

QC
807.5
.U6
W6
no.89
c.2

NOAA Technical Memorandum ERL WPL-89



A FIXED-DELAY, FREQUENCY-SHIFTED MICHELSON INTERFEROMETER
FOR REMOTE AIR TEMPERATURE MEASUREMENT

Lawrence Alan Johnson

Wave Propagation Laboratory
Boulder, Colorado
January 1982

noaa

NATIONAL OCEANIC AND
ATMOSPHERIC ADMINISTRATION

/ Environmental Research
Laboratories

QC
807.5
U6W6
no. 89

NOAA Technical Memorandum ERL WPL-89

A ~~1~~ FIXED-DELAY, FREQUENCY-SHIFTED MICHELSON INTERFEROMETER
FOR REMOTE AIR TEMPERATURE MEASUREMENT

Lawrence Alan Johnson

Wave Propagation Laboratory
Boulder, Colorado
January 1982



UNITED STATES
DEPARTMENT OF COMMERCE

Malcolm Baldrige,
Secretary

NATIONAL OCEANIC AND
ATMOSPHERIC ADMINISTRATION

John V. Byrne,
Administrator

Environmental Research
Laboratories

George H. Ludwig
Director

82 00602

This Technical Memorandum is a reprint of the dissertation with the same title accepted in partial fulfillment of the requirements for the degree of Doctor of Philosophy in the Graduate College, The University of Arizona, in 1981.

TABLE OF CONTENTS

	Page
LIST OF ILLUSTRATIONS	vi
LIST OF TABLES	ix
ABSTRACT	x
1. INTRODUCTION	1
Background	2
Statement of the Problem	6
Historical Note	6
Overview of the Work Reported Here	7
2. LIGHT SCATTERED IN THE ATMOSPHERE	12
Rayleigh-Brillouin Scattering	12
The Kinetic Limit, $y = 0$	17
Values of y Calculated	18
Rayleigh-Brillouin Spectrum ($y > 0$)	19
Aerosol Scattering	21
Raman Scattering	23
Composite Scattered Spectrum	24
Summary and Source Bandwidth Considerations	25
3. FIXED-DELAY MICHELSON SPECTROSCOPY	27
Interferometric Spectroscopy — A Review of its Theoretical Basis	28
The Real Interferometer	35
Extended Source	36
Transmitting Components of Finite Thickness	38
Misadjustment and Imperfect Optics	39
Absorption and Non-Ideal Reflectivities	41
Summary and Result	42
Interferogram of Light Scattered in Air in the Kinetic Limit ($y = 0$)	43
Fixed-Delay Michelson Interferometer as a Temperature Sensor	46
Uncertainty	50
Fringe Visibility Function of Rayleigh-Brillouin ($y > 0$) Scattered Light and Calculation of F_c	53
Performance: Fixed-Delay Michelson Interferometer as a Near Optimum Spectral Filter	56

TABLE OF CONTENTS--Continued

	Page
Fixed-Delay Michelson Interferometer as a Near Optimum Filter and MDTC	60
4. FREQUENCY SHIFTING THE INTERFEROMETER	67
Frequency Shifting Technique	69
Application to the Michelson Interferometer	74
Signal Processing	81
Independent Measurement of I_1	83
The Spectral Filter Picture Revisited	84
Minimum Detectable Temperature Change (MDTC)	88
Expected Signal Level	91
5. EXPERIMENTAL OBJECTIVES, APPARATUS, AND PROCEDURES	95
Scattering Chamber and Related Systems	97
The Laser	97
Beam Shaping	98
Parasitic Light Suppressors	99
Gas Circulation and Temperature Control	102
The Interferometer and Its Related Systems	104
Rotating Waveplate Frequency Shifter	104
The Interferometer	105
Detector	108
Signal Processing Electronics	108
Procedures	109
Warm Up	110
Alignment	110
Temperature Data	111
System Checks	112
Calibration of the Thermistor Sensor	113
6. EXPERIMENTAL RESULTS	115
Factors Contributing to Experimental Uncertainty . .	115
Signal Drift	116
Non-Interferometric AC Signal Contributions . .	117
Possible Presence of Aerosol Scattering	117
Gas Flow Characteristics and Temperature	
Probe Calibration	118
Data Processing	119
Calculating and Removing Offsets	119
Removing Drift from the Data	120
Calculating MDTC	120
Calculating Temperature and its Uncertainty . .	121

TABLE OF CONTENTS--Continued

	Page
Results and Discussion	122
Signal Levels and Averaging Times	129
7. CONCLUSIONS	131
APPENDIX: CALCULATING THE y PARAMETER	135
REFERENCES	137

LIST OF ILLUSTRATIONS

Figure	Page
2.1. The Relationship Between the Quantities \vec{k} , \vec{k}_o , \vec{k}_s , \vec{E} , and ψ , θ	14
2.2. Spectrum of Rayleigh/Brillouin Scattered Light for Two Values of y	16
2.3. The y Parameter Graphed as a Function of Altitude	20
2.4. Comparison of the Scattered Spectra for $y = 0.43$ and $y = 0$	22
2.5. Composite Scattered Spectrum Including Rayleigh-Brillouin and Aerosol Scattering	25
3.1. Schematic Representation of an Ideal Michelson Interferometer	29
3.2. Gaussian Spectral Profile and the Resulting Interferogram	34
3.3. Interferogram and Fringe Visibility Function Due to Light Scattered from Air in the Kinetic Limit ($y = 0$)	45
3.4. Michelson Interferometer Fringe Visibility Function for Rayleigh-Brillouin Scattered Light	55
3.5. Partial Derivatives of $V(\tau)$ with Respect to Temperature and Pressure	55
3.6. Correction Factor F_c as a Function of OPD	56
3.7. A Simple Spectral Filter and Detector	58
3.8. Filter Function of a Fixed-Delay Michelson Interferometer	59
3.9. MDTC for a Rectangular Filter Function	63
3.10. MDTC for a Fixed-Delay Michelson Interferometer	64
3.11. MDTC for a Fabry-Perot Interferometer	66
4.1. Rotating Waveplate Frequency Shifter	71

LIST OF ILLUSTRATIONS--Continued

Figure	Page
4.2. The Modified Michelson Interferometer Used in This Investigation	76
4.3. The Relationship of the Spectrum $I_v(v)$ to the Generalized Filter Function $F(v)$ of the Interferometer/Signal Processor Combination	88
4.4. MDTC vs. τ for the Frequency Shifted Michelson Interferometer and Classical Michelson Interferometer	90
4.5. MDTC vs. τ for the Frequency Shifted Michelson Interferometer Including the Effects of a Non-Ideal Interferometer	92
4.6. Schematic Representation of Source and Collecting Lens Geometry	93
5.1. Schematic Layout of the Experimental Apparatus	96
5.2. Side Drawing of the Scattering Chamber	99
5.3. Beam Dumper Assembly	100
5.4. Interaction Region	102
5.5. The Interferometer and Detector Layout	106
5.6. Detector and Signal Processing Electronics	109
6.1. Graphical Illustration of the Technique Used for Removing Signal Drift from the Temperature Data	121
6.2. Measured MDTC vs. OPD	123
6.3. Measured and Calculated Air Temperatures Based on Interferometer Output Signals with an Optical Delay of 4.6 cm	124
6.4. Measured and Calculated Air Temperatures Based on Interferometer Output Signals with an Optical Delay of 6.0 cm	125

LIST OF ILLUSTRATIONS--Continued

Figure	Page
6.5. Measured and Calculated Air Temperatures Based on Interferometer Output Signals with an Optical Delay of 8.0 cm	126

LIST OF TABLES

Table	Page
3.1. Uncertainties Contributing to the Measurement of Temperature	52
3.2. Sensitivity of F_c to changes in T' , T , and P	57

ABSTRACT

The spectral width of single-frequency radiation scattered in the atmosphere may be used to determine air temperature. In general, the measurement is complicated by pressure dependent changes in the spectral profile of the scattered radiation and by the inherently low received signal levels. A fixed-delay Michelson interferometer minimizes both of these problems by: (1) exhibiting a low sensitivity to pressure induced changes in the scattered spectrum and (2) optimally utilizing the available signal. By frequency shifting the signal in one arm of the interferometer relative to the other it is possible to efficiently modulate the output of the interferometer and make it insensitive to small changes in the center frequency of the scattered spectrum. Laboratory results obtained using a fixed-delay, frequency-shifted Michelson interferometer demonstrate the ability of this instrument to remotely measure air temperatures in the range 290 K to 310 K with an uncertainty of ± 2 K with averaging times on the order of seconds at a received signal level of 6×10^{-10} watts.

CHAPTER 1

INTRODUCTION

This dissertation reports the theoretical description and experimental verification of a form of Michelson interferometer capable of remotely measuring air temperature. The technique used is based on the fact that single frequency radiation scattered from air molecules is Doppler broadened into a spectrum the width of which depends on the temperature of the air. It is shown that a simple fixed-delay Michelson interferometer is capable of efficiently and accurately monitoring the spectral width to produce a signal from which temperature may be calculated. Further, it is shown that a simple rotating waveplate device may be used to frequency shift one arm of the interferometer relative to the other to modulate the output signal and make it insensitive to small changes in the center frequency of the scattered spectrum. In the experimental work reported here a fixed-delay, frequency-shifted Michelson interferometer was constructed and used to measure absolute temperatures in the range 290 K to 310 K within a laboratory scattering chamber. The remotely measured temperatures generally agreed with in situ measurements to within ± 2 K and the minimum detectable temperature change due to signal shot noise was 1.2 K both for signal averaging times on the order of seconds.

In this chapter background material for the problem of remote measurement of air temperature is given including a brief historical

review of several important concepts. Next the specific problem addressed by this work is described and in the last section a brief overview of the work reported here is given.

Background

The desire for accurate temperature profiles up through the atmosphere often arises in the atmospheric sciences. Temperature and other parameters need to be known at various times in order to study atmospheric dynamics. In particular these parameters are used as inputs to the computer models essential to weather forecasting.

Currently, temperature profiles are measured at selected locations twice a day by the use of radiosonde balloons. Although they provide accurate temperature measurements, radiosondes are inconvenient to use and cannot provide continuous profile data. A more convenient method of measuring temperature profiles is sought.

Ground based remote sensors are a natural choice for the job of continuous measurement of atmospheric temperature profiles. Many techniques have been proposed that utilize electromagnetic radiation ranging from microwaves to the visible region of the spectrum. To date the most successful technique is probably that of microwave radiometry. Temperature profiles up to 12 km have been demonstrated with uncertainties on the order of 2 K.^{1,2} To obtain these temperature profiles an inversion technique must be used to reduce the data. As a consequence, the temperature uncertainty grows rapidly at the higher altitudes unless an independent measure of temperature or knowledge of the height of the temperature inversion layer is available. Also

extension to heights above 10-12 km is difficult due to the nature of the problem. Consequently, there is a need to develop other remote sensors to complement the existing capabilities.

Various optical probing techniques have been proposed in this connection. In every case the basic idea has been to probe the atmosphere with a strong source of light and then analyze the light scattered back to obtain the temperature information. One of the most promising optical probing techniques was first suggested by Fiocco and DeWolf in 1968.³ The technique they proposed relied on the fact that Rayleigh scattered light from gas molecules is Doppler broadened, and the width of the scattered spectrum is directly related to the kinetic temperature of the gas molecules. To a good approximation, if the width of the scattered spectrum is known, temperature may be calculated directly.

Fiocco and DeWolf first proposed measuring air temperatures by using a Fabry-Perot interferometer to determine the spectral width of the scattered light.³ In 1971 Fiocco, et al. reported the results of their first attempts to measure atmospheric temperatures.⁴ In one nighttime experiment they were able to determine atmospheric temperatures at altitudes up to about 5 km by averaging their data for 1 h. They estimated the uncertainty of the measurement to be on the order of a few degrees Kelvin. These results are encouraging although greater ranges, greater accuracy, and shorter averaging times would be necessary to make this technique useful today.

In the nine years since Fiocco and his coworkers reported their experimental results no new experimental data has been published regarding this technique. Yet, in those intervening years advances in optical technology have made optical remote sensors more and more attractive. For example, lasers with high average power and narrow linewidths have been developed, dielectric coated, spherical mirror Fabry-Perot etalons with finesse >200 have become available, and other spectroscopic techniques have also gained prominence.

The problem is basically a classical spectroscopic one: How does one measure the spectral width of a weak source of radiation? And, more crucially, how does one measure very small changes in that spectral width. To give some idea of the parameters involved, consider the following. Under typical atmospheric conditions Rayleigh scattered light from a narrow bandwidth laser beam at 500 nm would be spread into a Gaussian spectrum roughly 3 GHz wide. A typical pulsed lidar system operating with a pulse energy of 1 joule would collect only about 3.8×10^4 photons from a 150 m range cell 5 km away, assuming that the entire spectrum is received. A 1 K change in temperature would cause only a 0.17% change in the full-width-at-half-maximum of the Rayleigh scattered spectrum.

In the simplest visualization, one would scan the scattered spectrum with a narrow bandpass spectrometer to measure its spectral width. This is what Fiocco and DeWolf did using a Fabry-Perot spectrometer.^{3,4} To get an idea of the resolving power required, let us say that the bandpass of the spectrometer must be 1/50 the spectral width

of the scattered spectrum to be recovered. This leads to a resolving power of about 10^6 for the conditions stated above.

If only a small etendue is required then in principle a resolving power of 10^6 is within reach of several types of spectrometers. However, in practice prism and diffraction grating instruments would have to be excessively large. Of the classical spectroscopic techniques this leaves only Fabry-Perot and Michelson interferometers. In a recent paper, Lading and Jensen⁵ reviewed this choice from an estimation theory point of view and concluded that if many parallel channels are available, spectral analysis (such as with Fabry-Perot interferometers) is preferable. If a single channel is available, Fourier spectroscopy (such as with a Michelson interferometer) is preferable.

Recently Schwiesow and Lading⁶ have proposed the use of two stabilized, fixed-delay Michelson interferometers for measuring atmospheric temperature profiles, although no experimental work was reported. This dissertation reports the theory and experimental verification of a similar instrument consisting of a single fixed-delay Michelson interferometer tested with a laboratory scattering chamber. One unique characteristic of the instrument described here is that it produces an output signal that is insensitive to small changes in the center frequency of the scattered spectrum. This characteristic is achieved by frequency shifting one arm of the interferometer relative to the other and then detecting only the amplitude of the modulated output.

The ability of any remote sensor to determine air temperature from measurements of the width of the Rayleigh scattered spectrum

depends critically on the variability of the scattered spectrum with atmospheric parameters other than temperature. Yet, it is known that in the lower atmosphere the spectrum of Rayleigh scattered light from air depends slightly on pressure.³ The effect of this pressure dependence on a Michelson interferometer remote temperature sensor has not yet been adequately studied. An important aspect of this work is that here it is shown that the Michelson interferometer temperature sensor is surprisingly insensitive to this effect.

Statement of the Problem

The problem specifically addressed by this work was to develop, build, and test a simple experimental Michelson interferometer capable of remotely measuring air temperature with an uncertainty on the order of 1 K. This work represents part of an initial effort to develop this type of instrument as a field system capable of measuring atmospheric temperature profiles. As such, several simplifications were acceptable in this work that would not exist in an atmospheric application. For example, since the experimental work was done with a laboratory scattering chamber, aerosols were filtered out and background radiation was reduced to a negligible level. However the theoretical concepts developed are quite general and should prove useful to workers in this field.

Historical Note

The concept of measuring atmospheric temperatures by monitoring the spectral width of Rayleigh scattered light is relatively new, due

mainly to the unavailability of monochromatic, high energy sources of visible light prior to the early sixties. In 1968 Fiocco and DeWolf first suggested the possibility of such a measurement³ and in 1971 reported some experimental results.⁴ Following these publications no new material appeared in the open literature until 1979 when the concept of using a fixed delay Michelson interferometer for measuring atmospheric temperatures was suggested. Recently, Lading and Jensen have compared Fabry-Perot and Michelson interferometers for measuring narrow spectral widths (and therefore temperature) on the basis of estimation theory⁵ and Schwiesow and Lading have proposed the use of two, fixed-delay Michelson interferometers for atmospheric remote temperature sensing.⁶

In a more general sense, the idea of using a Michelson interferometer to measure spectral linewidths dates back to the early work of Michelson. In the late 1800's Michelson used his interferometer to measure the spectral widths and doublet separations of the emission lines of many elements by measuring the fringe visibility function of each source.^{7,8} Curiously, in spite of the elegance and simplicity of this technique, fringe visibility measurements have rarely been used since that time. An exception is the work done by Terrien⁹ who used fringe visibility measurements to determine the spectral profile of emission lines in much the same way as Michelson.

Overview of the Work Reported Here

The work reported here represents three important contributions. Most significant are the experimental results which are the first remote

air temperature measurements made using a Michelson interferometer. It is noteable that temperature uncertainties on the order of ± 2 K were achieved for averaging times of a few seconds at received signal levels of 5×10^{-10} watts. Another important contribution of this work is the introduction of a frequency shifting technique to interferometric spectroscopy. While this technique has been used in optical testing for several years this work represents its first application to the Michelson interferometer for a spectroscopic measurement. Another important contribution of this work is the theoretical analysis of the effects of Brillouin scattering on temperature measurement by the Rayleigh linewidth technique. Although the effects of Brillouin scattering are acknowledged by all authors writing in this field, this work represents the first serious effort to quantify the extent of these effects and suggest appropriate corrections.

In Chapter 2 we begin with a brief review of the characteristics of light scattered from air. Primarily, we will be interested in the spectral characteristics of Rayleigh scattered light from air molecules, although aerosol and Raman scattering are also mentioned. It is shown that the spectrum of Rayleigh scattered light is approximately Gaussian and in this approximation its width varies with temperature but is independent of pressure. This fact forms the basis of the temperature sensing concept. The departure of the actual scattered spectrum from the Gaussian approximation and the effects of pressure are then estimated.

Chapter 3 is devoted to studying the application of a fixed-delay Michelson interferometer to measuring air temperature by way of its sensitivity to spectral linewidths. It is shown that for the case where no aerosols are present a single fixed-delay Michelson interferometer is capable of measuring air temperature relative to a single calibration. The noise performance of the interferometer is theoretically evaluated and compared to that of a Fabry-Perot spectrometer in terms of its minimum detectable temperature change. This analysis is benefitted by regarding the fixed-delay Michelson interferometer as a simple spectral filter. Finally, it is shown that under normal operating conditions such an interferometer is surprisingly insensitive to pressure induced changes in the scattered spectrum.

In Chapter 4 it is shown that the output of the interferometer can be made insensitive to changes in the center frequency of the scattered spectrum by frequency shifting one arm of the interferometer relative to the other. Experimentally this is important since it is difficult to obtain a radiation source of high frequency stability. A simple frequency shifting technique involving a rotating waveplate is reviewed and shown to be applicable to a Michelson interferometer with a simple modification. In effect, the frequency shifter creates a moving fringe pattern at the output of the interferometer which results in a modulated output signal. Finally, it is shown that an appropriate signal processing system produces an output which is proportional to the interferometer fringe visibility function and is therefore sensitive to changes in the temperature of the scattering gas.

Chapter 5 is devoted to a description of the experimental setup and procedures used in this investigation. The experimental setup consisted basically of two parts: (1) the laser source and scattering chamber that produced the source of scattered radiation under controlled conditions and (2) the interferometer and signal processing system that produced signals from which the temperature of the scattering gas was determined. The experimental procedure used consisted of measuring the signal levels at several known temperatures and interferometer optical delays. Other parameters measured experimentally were the level of background light and other residual signal levels due to sources other than Rayleigh scattered light.

In Chapter 6 the results of the experimental investigation are presented. Major problems turned out to be signal drift arising from various sources and residual signal levels not due to Rayleigh scattering. These problems made accurate measurements at long optical delays impossible, although they did not present a severe constraint at optical delays of primary interest. The minimum resolvable temperature change due to noise in the output signal varied roughly in accordance with the prediction of Chapter 4 verifying the presence of an optimum optical delay. At that optimum delay, temperatures in the range from 290 K to 310 K were measured with an uncertainty of ± 2 K and a minimum detectable temperature change of 1.2 K was indicated.

Finally, in Chapter 7 the work presented here is concluded. It is noted that the primary objective of this work is fulfilled by the experimental demonstration of remote temperature measurements using the

frequency-shifted, fixed-delay Michelson interferometer and the agreement of the theoretical predictions with those measurements. Although signal drift problems were a limiting factor in the experimental work reported here, these problems could be easily eliminated in an improved version of the interferometer. These considerations indicate that a frequency-shifted, fixed-delay Michelson interferometer can provide a simple and convenient instrument for remote measurement of air temperatures.

CHAPTER 2

LIGHT SCATTERED IN THE ATMOSPHERE

In this chapter I briefly review some aspects of light scattering in the atmosphere. Primary emphasis is placed on Rayleigh-Brillouin scattering since this is of central importance to this dissertation. Other scattering mechanisms discussed are aerosol and Raman scattering. Most of the material presented here is discussed in greater detail in the literature.^{3,10,11,12} Where possible I simply give a brief review and then quote results derived elsewhere.

Rayleigh-Brillouin Scattering

Rayleigh scattering is the scattering of electromagnetic radiation by particles much smaller than a wavelength. Here we will be concerned with the molecular scattering of visible light, which is indeed in the Rayleigh regime. The term "Rayleigh scattering" is used universally throughout the literature when discussing the intensity and angular distribution of scattered light. However, when discussing the spectral distribution of scattered light a number of different terms are used.¹³ In this dissertation I use the term "Rayleigh-Brillouin scattering" in that connection as this designation seems to be favored by current authors.

Introduction

The mechanism of Rayleigh scattering can be explained in a number of ways. In one common approach one calculates the dipole moment

induced in each scattering molecule and then sums the reradiated field of each molecule to arrive at the total scattered field.¹⁰ However, this simple approach in itself is incomplete. It can be shown that for a perfectly homogeneous scattering medium only forward scattering is possible.¹¹ In fact it is the local fluctuations in the number density of scatterers that produces angular scattering and the distributed spectrum of the scattered light.^{11,14,15} To put it another way, Rayleigh scattering is caused by local fluctuations in the dielectric constant of the medium. (This could equally well be stated in terms of fluctuations in the index of refraction of the medium.) Using the notation of Fiocco and DeWolf³ we may write the differential scattering cross section per unit volume as,

$$\frac{\partial^2 \Sigma}{\partial \Omega \partial \nu} = \frac{\partial \Sigma}{\partial \Omega} \cdot \phi_m(|\vec{K}|, \nu) \quad (2.1)$$

where ν is the (optical) frequency and Ω is the solid angle of interest. Here \vec{K} is the vector difference between the incident and scattered wave vectors (e.g., for backscatter $|\vec{K}| = 2 \cdot 2\pi/\lambda_0$). In eqn. 2.1, $\partial \Sigma / \partial \Omega$ represents the angular distribution of scattered light and $\phi_m(|\vec{K}|, \nu)$ represents the spectral distribution, where $\phi_m(|\vec{K}|, \nu)$ is normalized to unit area. Equation 2.1 may be used to calculate the power scattered into a solid angle Ω and frequency interval ν_1 to ν_2 from a small volume V as follows:

$$P = I_0 V \int_{\Omega} \int_{\nu_1}^{\nu_2} \frac{\partial^2 \Sigma}{\partial \Omega \partial \nu} d\Omega d\nu \quad (2.2)$$

where I_0 is the irradiance of the incident beam which is assumed to be uniform throughout V .

The angular distribution of scattered light is well known and may be expressed in terms of the refractive index of the gas,¹⁰

$$\frac{\partial \Sigma}{\partial \Omega} = \frac{9\pi^2}{\rho_0 \lambda^4} \left[\frac{n^2 - 1}{n^2 + 2} \right]^2 \sin^2 \psi \quad (2.3)$$

where ρ_0 is the molecular number density of the gas and n is the index of refraction. The scattering angle ψ is defined as the angle between the incident \vec{E} vector and the scattered wave propagation vector, as shown in fig. 2.1. Although $\partial \Sigma / \partial \Omega$ appears to be inversely proportional to number density ρ_0 in eqn. 2.3, the index of refraction is also a function of ρ_0 , and as a result $\partial \Sigma / \partial \Omega$ is actually nearly proportional to ρ_0 .¹⁶

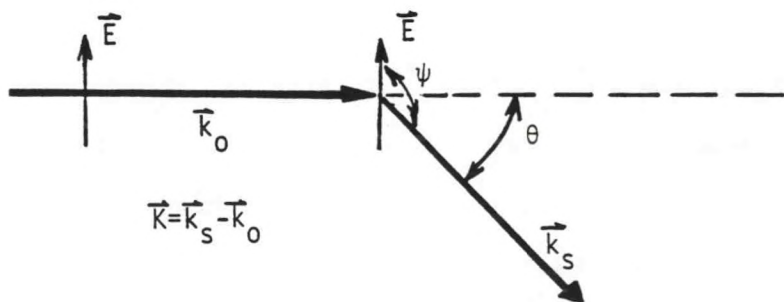


Fig. 2.1. The Relationship Between the Quantities \vec{k} , \vec{k}_0 , \vec{k}_s , \vec{E} , and ψ , θ .

In the case of isotropic scattering molecules (for example a noble gas) and polarized incident radiation, the scattered light is also polarized. The E vector of the scattered light lies in a plane that contains the incident light E vector and the scattered light wave propagation vector. In the case of nonisotropic scattering molecules such as nitrogen and oxygen in air, some depolarization occurs. For example, in nitrogen about 0.3% of the scattered light is polarized orthogonally to direction of polarization of the strongest component.¹⁷ Because of its relative weakness this "depolarized" component will be ignored throughout the rest of this dissertation.

Unfortunately, the spectral distribution of the scattered light is not as easily described as the angular distribution. Physically, the spectral distribution results from Doppler shifts in the scattered light associated with the molecular velocity distribution. In the limit of non interacting particles the spectral distribution is Gaussian. Physically, this limit is approached in rarefied gases when collisions between particles are infrequent. However, at pressures near atmospheric pressure, some interaction between gas molecules occurs. In this case the scattered spectrum is no longer purely Gaussian. A pair of Brillouin wings begin to emerge located symmetrically on either side of the center frequency^{3,11,12} as shown in fig. 2.2.

The extent of molecular interaction is usually characterized by a dimensionless parameter, y , which is defined as the ratio of the wavelength of density fluctuations in the medium to the molecular mean free path between collisions.^{15,18,19} Since y is an important parameter in

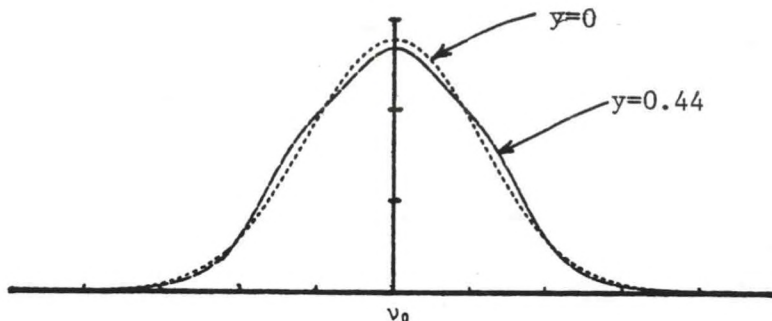


Fig. 2.2. Spectrum of Rayleigh-Brillouin Scattered Light for Two Values of y .
($T=300$ K, $\lambda=514.5$ nm, backscatter).

the models used to calculate the spectrum of Rayleigh-Brillouin scattered light it will appear frequently through this chapter. In the limit of non-interacting particles (often referred to as the kinetic limit) the y parameter tends to zero. As particle interactions become more important, y increases, indicating that the scattered spectrum is no longer purely Gaussian. The value of y may be calculated from measurable experimental parameters and for the purposes of the work reported here, the following convenient expression has been used:

$$y \approx 0.2308 \frac{T(K) + 110.4}{[T(K)]^2} \frac{P(atm) \lambda(\text{nm})}{\sin(\theta/2)} \quad (2.4)$$

where the required units are indicated. The scattering angle θ is the angle between the incident and scattered wave propagation vectors as shown in fig. 2.1. A discussion of the assumptions used to arrive at this expression is given in the Appendix.

The theoretical models used to calculate the spectrum of Rayleigh-Brillouin scattered light are still being perfected. None of them

have yet been applied to the case of air, although recent results indicate excellent agreement between theory and experiment for nitrogen.²⁰

When necessary, I have used the model proposed by Yip and Nelkin²¹ to calculate the Rayleigh-Brillouin scattered spectrum. Although their model is not as accurate as more recent ones, it is easy to use and is adequate for answering the questions asked here.

Generally throughout this dissertation the spectrum of scattered light is assumed to be Gaussian. Computationally this analytic form is appealing since it is easy to work with. One of the purposes of this chapter is to estimate how much the true scattered spectrum differs from the Gaussian form and to estimate how much pressure and temperature affect the true scattered spectrum. We begin by examining the kinetic limit in which there is no interaction between gas molecules.

The Kinetic Limit, $y = 0$

In the kinetic limit ($y = 0$) there is no interaction between molecules. In this case the spectrum of scattered light is simply Gaussian,³

$$\phi_m(|\vec{K}|, \Delta\nu, T) = \left(\frac{2\pi M}{|\vec{K}|^2 k_B T} \right)^{1/2} \exp \left(- \frac{2\pi^2 M \Delta\nu^2}{|\vec{K}|^2 k_B T} \right) \quad (2.5)$$

where $\Delta\nu = \nu_0 - \nu$, ν_0 being the frequency of incident radiation. Here and throughout the dissertation I will simply use the average molecular mass for M , where the average is taken over various molecular species present in air. Schwiesow and Lading⁶ estimate that less than a 1% error is introduced into the calculation of $\phi(|\vec{K}|, \Delta\nu, T)$ by using this approximation.

In terms of a width parameter, b , eqn. 2.5 may be written as,

$$\phi_m(\Delta\nu, T) = \frac{1}{b\sqrt{T}} \exp\left(-\pi \frac{\Delta\nu^2}{b^2 T}\right) \quad (2.6)$$

where,

$$b^2 = \frac{|\vec{K}|^2 k_B}{2\pi M} \quad . \quad (2.7)$$

In eqn. 2.6 the functional dependence on $|\vec{K}|$ is not shown explicitly since this is assumed to be essentially constant for the experiment described here. The important feature to note is that in this approximation ($y = 0$) the width of the spectrum varies only with the temperature, T , assuming that the scattering geometry, incident frequency, and average mass remain constant. The scattering geometry and the frequency of incident light are both parameters of the experimental setup. With care these parameters may be made constant. The average mass depends on the mixing ratio of the various gases in air. Generally the proportions of these gases is taken to be constant below 90 km.²² Thus, the spectral width is a function solely of temperature. This fact forms the basis of the concept of remote air temperature measurement by spectral analysis of Rayleigh-Brillouin scattered light. To determine how appropriate the simple expression of eqn. 2.6 is to the true Rayleigh-Brillouin spectrum we next calculate the value of y expected for the experimental conditions of this investigation. This value can then be used to estimate the true scattered spectrum.

Values of y Calculated

In the experimental work for this dissertation pressure and temperature were about 0.803 atm and 300 K respectively. The laser

wavelength was 514.5 nm and the scattering angle ranged from 175° for the marginal ray entering the optical system to 180° for the axial ray. The factor $\sin(\theta/2)$ (cf. eqn. 2.4) differs by about 0.1% between these two values of θ . Consequently, I will simply use $\theta \approx 180$. Using these values, eqn. 2.4 may be evaluated resulting in a value $y = 0.43$. As explained in the Appendix this value is about a factor of two larger than the typical values quoted by Fiocco³ and others.^{23,24} However this value is consistent with recent experimental results for nitrogen.²⁰

It is also interesting to evaluate y for typical atmospheric conditions at a range of altitudes. Figure 2.3 is a graph of y vs. altitude, z , using appropriate values of temperature and pressure from the U.S. Standard Atmosphere.²⁵ In the graph backscatter ($\theta = 180^\circ$) is assumed at a wavelength of $\lambda = 514.5$ nm.

Rayleigh-Brillouin Spectrum ($y > 0$)

In this section we explore the differences between the spectrum of scattered light in the kinetic limit ($y = 0$) and the estimated actual spectrum ($y \approx 0.43$). Since the shape of the actual scattered spectrum depends in part on the value of y it should be clear from eqn. 2.4 that pressure as well as temperature will determine its shape. This complicates the problem of determining temperature since it implies that a knowledge of pressure is required in addition to a measurement of spectral width.

For the experimental work reported here, air pressure in the scattering chamber was easily measured. However, in an atmospheric remote sensing application, accurate *a priori* knowledge of pressure as

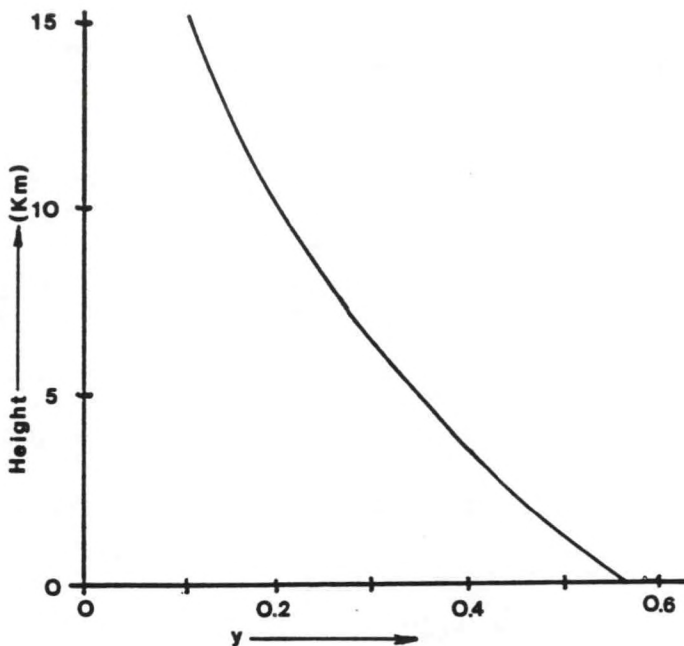


Fig. 2.3 The y Parameter Graphed as a Function of Altitude.

The U.S. Standard Atmosphere, 1962²⁵ is assumed with backscatter and $\lambda = 514.5$ nm.

a function of height is not usually available. However, using a statistical approach based on radiosonde data, pressure profiles may be estimated for a given location, date, and time of day. If surface pressure is known then pressures at heights to 10 km may be predicted with uncertainties on the order of 6 mbar or less. Fortunately, nearer the surface where the departure of the spectrum from a Gaussian is greatest, pressures may be predicted with greatest accuracy — approaching 2 mbar at 1 km.²⁶

Using the model proposed by Yip and Nelkin²¹ I have calculated the scattered spectra for $y = 0$ and for conditions appropriate for this

experiment, $y = 0.46$. From fig. 2.3 it can be seen that in terms of the y parameter these conditions are also appropriate for a U.S. Standard Atmosphere height of about 3 km. The spectrum for $y = 0.46$ differs from the spectrum for $y = 0$ by more than 20% in some places as can be seen in fig. 2.4. However, generally $\partial\phi_m/\partial T$ (per K) is at least several times larger than $\partial\phi_m/\partial P$ (per mbar). Therefore a pressure uncertainty of a few mbar is equivalent to a temperature uncertainty of several tenths of a degree K or less at a given point on the spectrum.

While interesting, these results are difficult to intuitively apply to the response of a Michelson interferometer. It will be shown in the next chapter that the Michelson interferometer effectively samples the Fourier transform of the spectral distribution of the scattered light. Consequently further discussion of the effects of Brillouin scattering is deferred to the end of Chapter 3.

Aerosol Scattering

In this experiment I have attempted to work only with Rayleigh-Brillouin scattered light. Consequently, I have tried experimentally to reduce the effects of aerosol scattering to a negligible level. However, in order to test for the presence of aerosol scattering, it is necessary to understand some of its characteristics. The following paragraphs provide a brief summary of these characteristics.

Minute particles of dust and organic matter are always present in natural air. These particles range in size from $<0.1 \mu\text{m}$ to macroscopic. Because of their masses, these particles move at velocities much less than air molecules and as a consequence, the spectrum of light

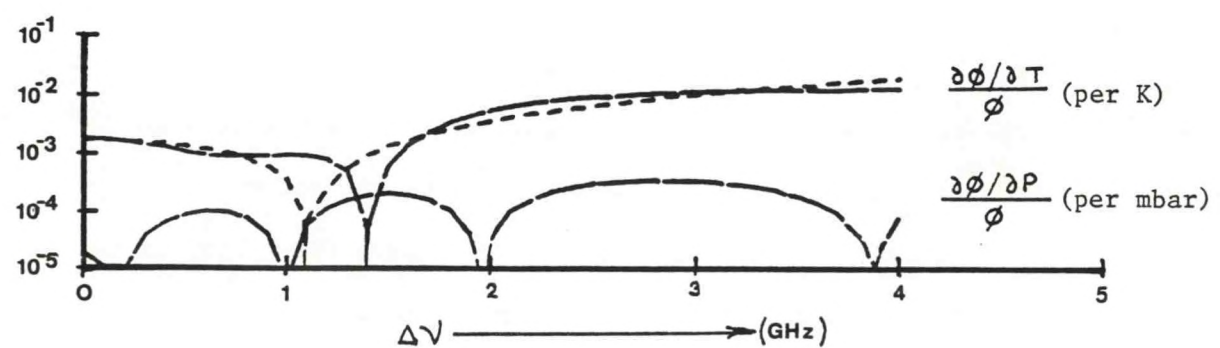
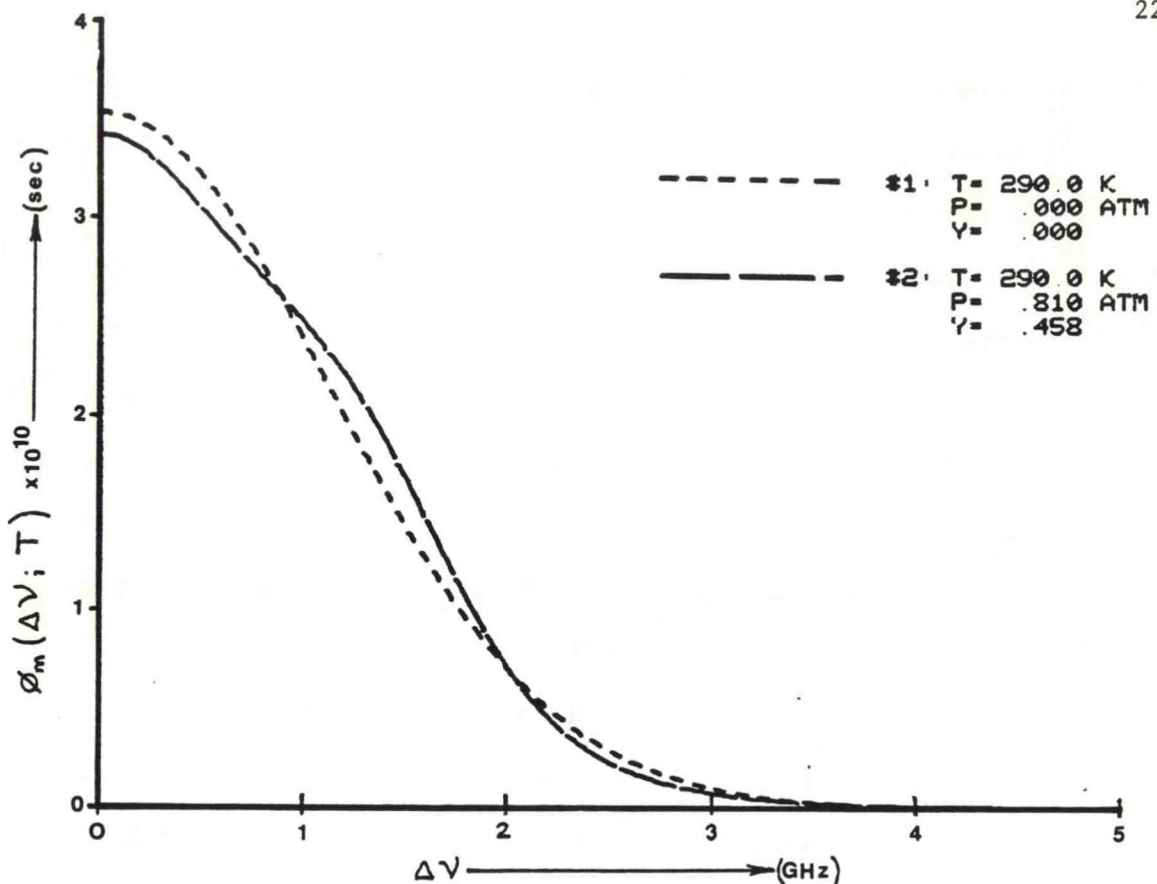


Fig. 2.4. Comparison of the Scattered Spectra for $y = 0.46$ and $y = 0$.
 Also shown are derivatives with respect to temperature and pressure.
 In all cases $T = 290$ K, $\lambda = 5.145$ nm (backscatter).

scattered from aerosols is much narrower than the Rayleigh-Brillouin spectrum. Fiocco and DeWolf³ show that the aerosol spectrum is Lorentzian and estimate a spectral width on the order of 10^5 Hz. This is approximately four orders of magnitude narrower than the Rayleigh-Brillouin spectrum. Consequently, the aerosol spectrum will be approximated by a delta function throughout this dissertation. With this approximation the aerosol spectrum may be written,

$$\phi_a(\Delta\nu) = \delta(\Delta\nu) \quad (2.8)$$

where $\delta(\Delta\nu)$ is the Dirac delta function. Note that the angular dependence is not specified. In general, the angular dependence of aerosol scattering is quite complicated and since it has no particular bearing in this work I have omitted it.

In the lower atmosphere the volume scattering cross section for aerosols is generally much greater than for Rayleigh-Brillouin scattering. Therefore an important aspect of the experimental setup was its ability to filter out these aerosols. It will be shown later that the filtering system was successful and aerosol scattering was reduced to a negligible level.

Raman Scattering

Even in pure air the spectrum of scattered light is more complicated than that predicted by Rayleigh-Brillouin theory alone. It is possible for the incident light to impart or receive energy from the

rotational or vibrational energy of the scattering molecule. The result is that some of the scattered light is upshifted or downshifted in frequency by an amount characteristic of the scattering molecule. This is Raman scattering.²⁷

In the case of air, Raman scattered light is shifted to a band of frequencies relatively far removed from the Rayleigh-Brillouin spectrum.²⁸ Additionally, the scattering cross sections for (non-resonant) Raman scattering by atmospheric constituents are about two orders of magnitude less than that for Rayleigh-Brillouin scattering.^{29,30} For these reasons Schwiesow and Lading⁶ have estimated that Raman scattered light has a negligible effect in the present application. Therefore, Raman scattering will be ignored throughout the remainder of this work.

Composite Scattered Spectrum

Neglecting Raman scattering and any background radiation we are left with Rayleigh-Brillouin scattering and aerosol scattering. A composite scattered spectrum is shown in fig. 2.5. The relative height of the aerosol peak shown in fig. 2.5 was chosen arbitrarily. In general the amount of aerosol scattering depends on the number and size distribution of aerosols present.

For a given scattering geometry the composite spectrum of scattered light may be expressed in terms of the spectral irradiance $I_\nu(\Delta\nu, T)$ at some plane in the optical system,

$$I_\nu(\Delta\nu, T) = I_m(T) \phi_m(\Delta\nu, T) + I_a \phi_a(\Delta\nu) . \quad (2.9)$$

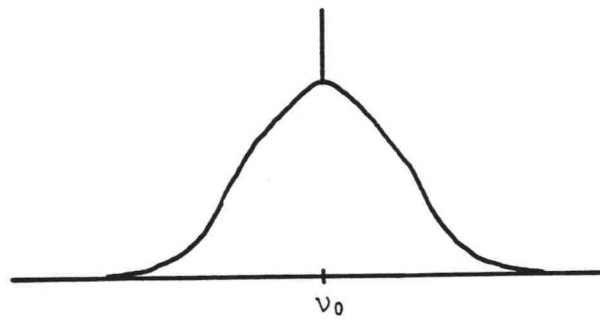


Fig. 2.5. Composite Scattered Spectrum Including Rayleigh-Brillouin and Aerosol Scattering.

Here $I_m(T)$ and I_a are the total irradiances due to molecular and aerosol scattering respectively; $\phi_m(\Delta\nu, \tau)$ and $\phi_a(\Delta\nu)$ are the respective normalized spectral distributions. The value of $I_m(T)$ may be calculated for a known scattering geometry by using eqns. 2.2 and 2.3. Note that since I_m is proportional to number density, it must be inversely proportional to temperature¹⁶ and this dependence is shown explicitly in eqn. 2.9 above. The value of I_a is not as easily calculated; for the purposes here it is sufficient to note that for a particular scattering geometry and wavelength, I_a is constant.

Summary and Source Bandwidth Considerations

In this chapter we have briefly reviewed the spectral characteristics of light scattered from air. It was shown that in the kinetic limit approximation ($y = 0$) the spectrum is Gaussian with a width that depends only on temperature (other parameters are constant). Under

typical atmospheric conditions ($y > 0$) the actual spectrum departs from a Gaussian and its shape depends on pressure as well as temperature. Aerosols, if present, scatter light into a spectrum that is very narrow relative to the Rayleigh-Brillouin spectrum. Raman and depolarized Rayleigh scattering have been neglected due to their relative weaknesses.

The results described in this chapter all assume that the spectrum of the incident radiation is infinitely narrow. In general this condition is never true and the actual scattered spectrum is a convolution of the source spectrum with the composite spectrum described by eqn. 2.9. However, the source used in this investigation was an argon ion gas laser having an effective bandwidth measured to be on the order of 1 MHz. This spectral width is more than three orders of magnitude narrower than that of the Rayleigh-Brillouin spectrum. In light of this fact, the composite spectrum of eqn. 2.9 may be used without modification.

This completes our review of light scattered from air. In the next chapter I show how the spectral characteristics of this light may be exploited to remotely measure air temperature by using a fixed-delay Michelson interferometer.

CHAPTER 3

FIXED-DELAY MICHELSON SPECTROSCOPY

The central purpose of this dissertation is to describe the theory and operation of a Michelson interferometer used as a remote sensor of air temperature. In the last chapter we reviewed the spectral characteristics of laser light scattered from air. In this chapter I describe the operation of a fixed-delay Michelson interferometer and show that its output provides an accurate and efficient estimate of the width of the scattered spectrum and therefore the temperature of the air.

In most spectroscopic problems involving a Michelson interferometer, the universal mode of operation is to measure the complete interferogram produced by the interferometer. The interferogram is then processed to recover the desired spectral information. An important aspect of this work is that the interferometer is operated at a single, fixed optical delay, thereby continuously monitoring a single point on the interferogram. In the problem at hand, three important results are obtained by operating the interferometer in this mode. First, it can be shown that in the signal shot noise limited case, the fixed-delay Michelson interferometer makes near optimum use of the available signal for determining spectral width. This is conveniently demonstrated by regarding the interferometer as a spectral filter. Secondly, it can be shown that the fixed-delay Michelson interferometer is nearly insensi-

tive to the effects of pressure in the true Rayleigh-Brillouin spectrum of scattered light ($y > 0$). Finally, a fixed-delay interferometer is very simple to build and can be made quite rugged for use in a field application.

In this chapter most of the theory is developed for a Michelson interferometer in the classical configuration even though the interferometer actually used in this investigation was a modified form. This approach provides a general theoretical framework. In Chapter 4 the frequency shifted interferometer used in this investigation is described and where necessary the concepts developed here are modified to suit that specific form. We begin the discussion of the fixed-delay Michelson interferometer with a brief review of its theoretical basis.

Interferometric Spectroscopy — A Review of its Theoretical Basis

The literature abounds with works on interferometric spectroscopy. It should suffice to mention here two recent books that are notable for their completeness. They are those by Chamberlain³¹ and Bell.³² In this section I present a brief review of the theoretical foundation of interferometric spectroscopy to establish the formalism for the rest of this chapter and the next.

We begin by referring to figure 3.1 which is a simplified schematic representation of a Michelson interferometer (note that this type of interferometer is more properly called a Twyman-Green interferometer since a point source is indicated). Initial assumptions are: (1) the wavefronts approaching the beamsplitter are plane waves propagating parallel to the optic axis of the interferometer, (2) the beamsplitter

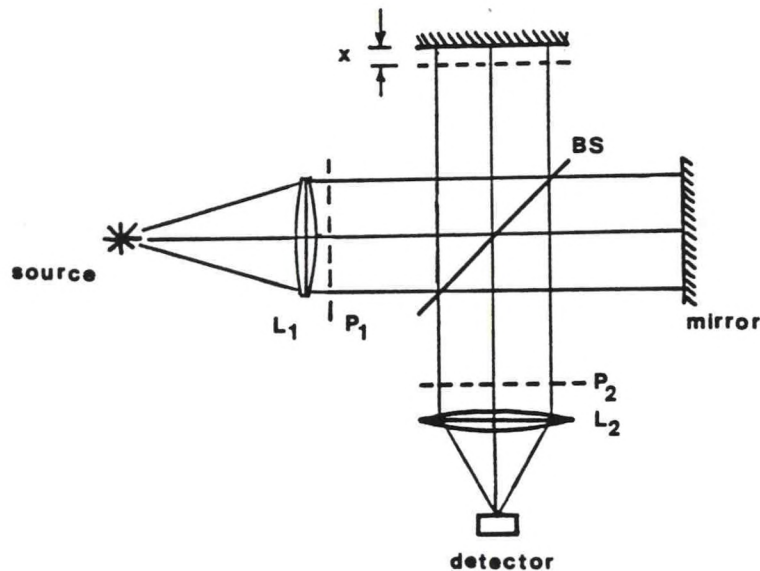


Fig. 3.1. Schematic Representation of an Ideal Michelson Interferometer.

is infinitely thin, perfectly flat, and lossless with an amplitude reflectance of $1/\sqrt{2}$, (3) the mirrors are also perfectly flat with an amplitude reflectance of 1, (4) a non-lossy, non-dispersive medium pervades and, (5) the spectrum of the input light is a bandlimited at optical frequencies. Of these assumptions, the last two are easily fulfilled in the problem at hand. The other assumptions require further consideration and will be discussed later in this chapter.

Expressing the real electric field at plane P_1 in terms of its associated analytic signal, we have³³

$$E_1(t) = \int_0^{\infty} a(v) e^{i[\phi(v) - 2\pi v t]} dv. \quad (3.1)$$

That is, we have expressed the electric field as the sum of an infinite ensemble of plane waves each with a different amplitude $a(\nu)$, phase $\phi(\nu)$, and frequency ν . At the output plane P_2 the electric field is composed of a component from each arm of the interferometer. Because of our assumptions we may express the field at P_2 in terms of the field at P_1 (neglecting diffraction) as

$$E_2(t) = \frac{1}{2} E_1(t - \tau_a) + \frac{1}{2} E_1(t - \tau_b) . \quad (3.2)$$

Each path through the interferometer introduces an optical delay that may be expressed in terms of time. It is the irradiance at plane P_2 that is of ultimate significance. This may be calculated directly from the electric field according to

$$I_2 = c\varepsilon \langle E_2^*(t) E_2(t) \rangle . \quad (3.3)$$

The brackets denote a time average (physically the response time of the detector), c is the speed of light, and ε is the electric permittivity of the pervading medium.

Rewriting equation 3.3 in terms of equation 3.2 we get

$$\begin{aligned} I_2(\tau_a, \tau_b) = & \frac{c\varepsilon}{4} \langle E_1^*(t + \tau_a) E_1(t + \tau_a) + E_1^*(t + \tau_b) E_1(t + \tau_b) \\ & + E_1^*(t + \tau_a) E_1(t + \tau_b) + E_1(t + \tau_a) E_1^*(t + \tau_b) \rangle . \quad (3.4) \end{aligned}$$

As usual, we can assume that the electric field is stationary, at least in the wide sense.³³ As a consequence, the first two terms of eqn. 3.4 are equal and their sum is simply the input irradiance at plane P_1 . We now have

$$I_2(\tau) = \frac{1}{2} I_1 + \frac{1}{2} c\varepsilon \operatorname{Re}\{E_1^*(t) E_1(t + \tau)\} \quad (3.5)$$

where again stationarity has been invoked to shift the time origin by replacing t with $t - \tau_a$ and letting $\tau \equiv \tau_b - \tau_a$. The term in brackets is the self coherence function of the field, $\Gamma(\tau)$. Writing eqn. 3.5 in terms of $\Gamma(\tau)$ we have

$$I_2(\tau) = \frac{1}{2} I_1 + \frac{1}{2} c\varepsilon \operatorname{Re}\{\Gamma(\tau)\} \quad (3.6)$$

The most crucial point in this derivation is identifying the self coherence function as the Fourier transform of the spectral density function $G(v)$ of the input field. This is the result of the well-known Wiener-Khintchine theorem (see for example Born and Wolf,³³ p. 504).

$$\operatorname{Re}\{\Gamma(\tau)\} = \int_{-\infty}^{\infty} G(v) e^{-i2\pi v \tau} dv. \quad (3.7)$$

Equations 3.7 and 3.6 together become

$$I_2(\tau) = \frac{1}{2} I_1 + \frac{1}{2} c\varepsilon \int_{-\infty}^{\infty} G(v) e^{-i2\pi v \tau} dv, \quad (3.8)$$

where

$$I_1 = c\varepsilon \int_{-\infty}^{\infty} G(v) dv.$$

Finally, the connection between $G(v)$ and the spectral irradiance, $I_v(v)$, at the input plane needs to be established. Here $I_v(v)$ is expressed as power per unit area per unit frequency interval and has units of $\text{W/m}^2 - \text{s}^{-1}$. Aside from the multiplicative constants there is an interesting requirement imposed by the mathematical representation chosen. Since the left hand side of equation 3.7 must be real, then $G(v)$ must be Hermitian. This is purely a consequence of the analytic representation of the electric field. Thus we are led to the following relationships:

$$I_v(v) = c\varepsilon G(v) \quad v > 0$$

$$G(v) = \begin{cases} \frac{1}{2} \frac{1}{c\varepsilon} I_v(v) & v \geq 0 \\ \frac{1}{2} \frac{1}{c\varepsilon} I_v(-v) & v < 0 \end{cases} \quad (3.9)$$

By convention, $I_v(v)$ is real and defined only for positive frequencies. Equations 3.8 and 3.9 can now be combined to express the output irradiance in terms of $I_v(v)$,

$$I_2(\tau) = \frac{1}{2} [I_1 + \int_0^{\infty} I_v(v) \cos 2\pi v \tau dv] , \quad (3.10)$$

where $I_1 = \int_0^{\infty} I_v(v) dv$.

Equation 3.10 is one way to state the basic relationship underlying Fourier transform spectroscopy. Experimentally, one measures $I_2(\tau)$ and then from it computes $I_v(v)$. It is sometimes more convenient to calculate the two-sided complex Fourier transform than the one-sided cosine transform of eqn. 3.10. However, it is easy to show that

$$\int_0^\infty I_v(v) \cos 2\pi v\tau \, dv = \operatorname{Re} \left\{ \int_{-\infty}^\infty I_v(v) e^{-i2\pi v\tau} \, dv \right\} \quad (3.11)$$

where the integration is carried out over negative frequencies which are set equal to zero.

In this dissertation we will deal exclusively with spectral distributions that are both narrow and symmetric with respect to their center frequency, v_o . In this case it is convenient to express eqn. 3.10 in the following form:

$$I_2(\tau) = \frac{1}{2} [I_1 + F\{I_v(v-v_o)\} \cos 2\pi v_o \tau] \quad (3.12)$$

where $F\{ \}$ denotes the complex Fourier transform. In the simple case of a Gaussian spectral profile the relationships between these various quantities are easily calculated. Figure 3.2 summarizes this example.

It is just this type of simple spectral profile with which Michelson did his original work. In the case of a symmetric spectral profile, the envelope of the interferogram fully characterizes the shape of the input spectrum. Michelson measured the envelope of the interferogram by defining a fringe visibility function $V(\tau)$,

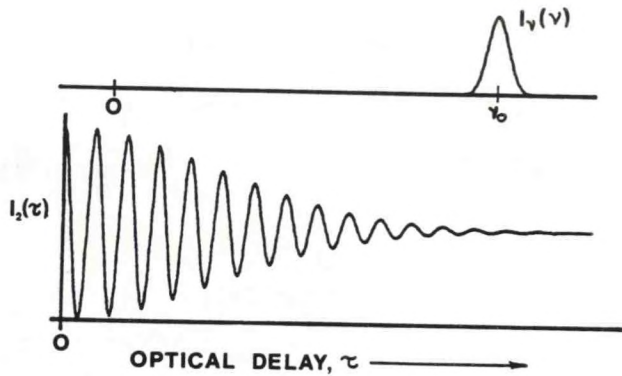


Fig. 3.2. Gaussian Spectral Profile and the Resulting Interferogram.

The Gaussian spectral profile is shown in (a) and the resulting interferogram in (b).

$$V(\tau) = \frac{I_2(\tau)_{\max} - I_2(\tau)_{\min}}{I_2(\tau)_{\max} + I_2(\tau)_{\min}} .$$

Substituting eqn. 3.12 into this expression one obtains the following result:

$$V(\tau) = F\{I_v(v-v_0)\}/I_1 . \quad (3.13)$$

That is, the fringe visibility function is equal to the normalized modulus of the Fourier transform of the spectral irradiance distribution. Expressing eqn. 3.12 in terms of this result we finally get

$$I_2(\tau) = \frac{1}{2} I_1 [1 + V(\tau) \cos 2\pi\nu_0\tau] . \quad (3.14)$$

This is the desired result that relates the output of the interferometer to the fringe visibility function $V(\tau)$.

This completes our review of the basis of transform spectroscopy. The most important result is that for a symmetric input spectrum, the output of the interferometer is simply related to the fringe visibility function $V(\tau)$, as shown in eqn. 3.14. Because the input spectral width depends on temperature, so also must the width of the fringe visibility function. It will be shown that by monitoring the value of the visibility function at a single appropriate point, the temperature of the scattering gas may be determined. First however, we must consider the effects of departures from the ideal interferometer originally assumed.

The Real Interferometer

We began the discussion of transform spectroscopy by assuming that a perfect interferometer was used in conjunction with a point source of light. Of course, these conditions are never achieved in reality. In the experiment described here, departures from the ideal included: (1) a source of both lateral and axial extent, (2) transmitting components of finite thickness (e.g., the beamsplitter), (3) misadjusted and imperfect optics, and (4) component absorption and reflectivities differing from those originally assumed. Each of these departures from the ideal bears on the operation of the interferometer.

The purpose of this section is to show that for the conditions and interferometer used in this investigation simple modifications of eqn. 3.14 yield an expression that accurately describes the operation of the real interferometer. Generally, the conditions mentioned above are adequately dealt with in the literature.^{31,32} In this section only brief summaries are given with results appropriate to the work described here. For a more detailed treatment the reader is referred to the literature.

Throughout this section use is made of the concept of optical path difference, OPD, which is simply the optical distance between two wavefronts of interest. In transform spectroscopy the two wavefronts of interest are generally those coming from different arms of the interferometer. In this connection we have already made use of the optical delay τ , which is related to OPD by the speed of light and the index of refraction of the pervading medium, $OPD = nct$.

Extended source

Referring to fig. 3.1, it can be seen that for a ray entering the interferometer parallel to the optical axis the OPD introduced would be $2x$, where x is the displacement of the mirror from the $OPD = 0$ condition. This holds true for all rays originating from an axial point source at the focus of the input lens. However, if the point source is moved off axis, the rays entering the interferometer then make an angle α with respect to the optical axis. From simple geometrical arguments³² it is easy to show that in this case the OPD introduced by the

interferometer is $2x \cos \alpha$. Thus, as the point source is moved off axis, the interferometer's OPD for that point source decreases.

If we now consider an extended source to be a collection of point sources the result is that the light from the source is distributed over a range of OPDs. In the case of a nearly monochromatic source, the effect of a spatially extended source on the interferogram is a reduction in fringe contrast.³² In terms of eqn. 3.14, this means that the observed fringe visibility function $V_o(\tau)$ would be less than the theoretical fringe visibility function $V(\tau)$ given by eqn. 3.13. It is convenient to account for this reduction in fringe visibility by a factor η_I , the interferometric efficiency defined by $V_o(\tau) = \eta_I V(\tau)$. In general, η_I will be a function of the optical delay τ . However for the purposes here it may be considered effectively constant over the range of τ of interest.

The usual procedure in transform spectroscopy is to simply limit the field of view of the instrument so that $\eta_I \approx 1$ for all wavelengths of interest. The criterion often used is that for the shortest wavelength of interest, the OPD for the edge of the field of view should differ by only $\lambda/2$ from the OPD for the center of the field of view. In the experimental work described in this dissertation, the source is a focused laser beam of high f/number, observed axially. Therefore, the lateral extent of the source is very small, easily fulfilling the criterion quoted above.

Due to the scattering geometry used in this investigation we must also consider the effect of a source extended in depth. Returning

to fig. 3.1, it can be seen that if the point source is displaced axially, then the beam entering the interferometer becomes either converging or diverging. In terms of rays entering the interferometer, again they are no longer parallel to the optical axis, but rather enter the interferometer at an angle α . In this case, α depends on both the axial displacement of the point source and the ray height at the input lens. Again, the same analysis described above may be applied in this case, to arrive at essentially the same result: an axially extended source results in a reduction in the interferometric efficiency η_I . However, the presence of a field stop in the optical system vignetted the light produced by scatterers displaced more than about $0.5''$ axially from the focus of the input lens. The result was that only rays fulfilling the OPD criterion quoted previously arrived at the interferometer. Therefore, virtually no reduction in interferometric efficiency η_I occurred due to the extended nature of the source.

Transmitting components of finite thickness

We now turn our attention to the transmitting components within the interferometer. For example, the interferometer used in this investigation had a beamsplitter made of a quartz plate with a surface dielectric coating. In effect this introduced an unequal glass path between the two arms of the interferometer. An unequal glass path affects both the spectral response and the field of view of the interferometer. Since the source spectrum in this investigation was nearly monochromatic the former effect may be neglected. However,

the field of view and its relationship to the source are important (as pointed out previously).

Compensation for a plate-type beamsplitter is usually introduced by placing a plate of identical material and dimensions in the arm of the interferometer that is lacking.³⁴ This was the case in the interferometer used in this investigation however there was also a multiple order quartz quarter waveplate in one arm of the interferometer thereby slightly uncompensating it again. Surprisingly, simple calculations reveal that the presence of the waveplate actually increased the field of view of the instrument. Therefore, the presence of the transmitting components in the interferometer should have no effect on its output.

Misadjustment and imperfect optics

Now we consider the effect of slightly misaligned mirrors and imperfect optics. By imperfect optics I refer to the case where the OPD varies slightly as a function of position in the aperture even for a collimated input beam. This might be caused either by surface errors on the mirrors or index of refraction variations in the transmitting components.

Chamberlain³¹ defines a spectral distortion factor $d(\lambda)$:

$$d(\lambda) = \frac{1}{A} \iint_A \cos[2\pi \delta(u,v)/\lambda] du dv \quad (3.15)$$

where the integration is carried out over the clear aperture of the interferometer. The function $\delta(u,v)$ is simply the difference in optical

path between the real interferometer and the ideal interferometer at a particular point in the aperture defined by the coordinates (u, v) . For the present case, λ is effectively constant ($\lambda_o = c/v_o$) and eqn. 3.15 reduces to a constant. For perfect optics $d(\lambda_o) = 1$ and for less than perfect optics $d(\lambda_o) < 1$. In terms of the interferogram, $d(\lambda_o)$ simply multiplies the fringe visibility function,³¹

$$I_2(\tau) = \frac{1}{2} I_1 \{1 + d(\lambda_o) V(\tau) \cos 2\pi v_o \tau\}.$$

In other words, defects in the optics have the effect of reducing the effective fringe visibility. Again this reduction in fringe visibility may be conveniently accounted for by a reduction in the interferometric efficiency η_I . In this case, $\eta_I \propto d(\lambda_o)$.

As a point of reference consider the case where one of the mirror surfaces is slightly spherical instead of flat. For this case Chamberlain gives $\delta(\lambda) = \sin(4\varepsilon/\lambda)/(\pi/\lambda)$, where ε is the surface error of the edge of the mirror relative to the center. If $\varepsilon = \lambda_o/20$ then $\delta(\lambda_o) = 0.94$ resulting in a 6% reduction in the fringe visibility observed at the output of the interferometer.

Mirror misalignment may be considered as a specific optical defect. If one of the mirrors is tilted at an angle α with respect to the other, the spectral distortion factor is³¹

$$d(\lambda_o, \alpha) = 2 \frac{J_1(4\pi R\alpha/\lambda_o)}{4\pi R\alpha/\lambda_o},$$

where $J_1(x)$ is the first order Bessel function. Here, R is the clear aperture radius of the mirror. It is interesting to note that $d(\lambda_0, \alpha)$ is very sensitive to tilt. A tenth of a wave of tilt across the aperture ($2Ra/\lambda_0 = 0.1$) causes about a 5% reduction in the value of $d(\lambda_0, \alpha = 0)$. This is also a good indication of how sensitive this type of interferometer is to mechanical vibrations, instabilities, and misalignment.

Absorption and non-ideal reflectivities

Inevitably, any real interferometer will have some absorption and an unequal transmission of light through its two arms. This may be caused by absorption in any of the optical components, unequal reflection and transmission by the beamsplitter, or Fresnel reflection losses by other dielectric surfaces. These factors affect both the overall transmission of the instrument and its interferometric efficiency.³²

Bell³² treats the case where one mirror has an amplitude reflectance $r(\lambda)$ and the other has an amplitude reflectance of unity. For a monochromatic input spectrum, $r(\lambda)$ is constant and the interferogram would be (aside from a phase factor),

$$I_2(\tau) = \frac{1}{2} [I_1 \frac{1+r^2}{2} + |r| \int_0^\infty I_\nu(\nu) \cos 2\pi\nu\tau d\nu] . \quad (3.16)$$

Rearranging this result slightly and putting it in terms of the fringe visibility function as in eqn. 3.14, one obtains

$$I_2(\tau) = \frac{1}{2} I_1 \left(\frac{1+r^2}{2} \right) \left[1 + \frac{2|r|}{1+r^2} V(\tau) \cos 2\pi v_o \tau \right]. \quad (3.17)$$

In other words, there is a reduction in the overall transmission of the instrument and a reduction in the fringe visibility. The latter may be expressed as a reduction in interferometric efficiency η_I , as in the previous cases. The former may be expressed as a reduction in the overall system efficiency η_o , which would multiply I_1 in eqn. 3.17.

Absorptions and other losses in the interferometer may be accounted for in approximately the same manner as outlined above. The result may always be expressed simply as a reduction in overall system efficiency η_o and interferometric efficiency η_I . Note however that this simple result is true only when the input spectrum is nearly monochromatic, as in the case at hand.

Summary and result

In this section we have considered departures from the ideal interferometer. It was shown that a finite field of view resulted in a reduction in interferometric efficiency η_I . Similarly, imperfect or misaligned optics had the same result. In the case of unequal transmission by the two arms of the interferometer a reduction occurred in both the interferometric efficiency and overall efficiency η_o . In terms of eqn. 3.14 these factors are represented in the following simple modification,

$$I_2(\tau) = \frac{1}{2} I_1 \eta_o [1 + \eta_I V(\tau) \cos 2\pi v_o \tau]. \quad (3.18)$$

It will be shown later that these reductions in efficiency do not directly effect the measurement of temperature. Rather, they effect the signal-to-noise ratio and therefore the uncertainty in the temperature measurement.

In the next section we will use the above result (eqn. 3.18) along with eqn. 3.13 to calculate the interferogram due to the spectrum of Rayleigh-Brillouin scattered light from air. Following that, it will be shown how the output of the interferometer may be used to determine the temperature of the scattering gas.

Interferogram of Light Scattered in Air in the Kinetic Limit ($y = 0$)

Calculation of the interferogram of light scattered from air is simply an application of eqns. 3.18 and 3.13 to the spectral distribution of the scattered light. Unfortunately, as pointed out in Chapter 2, the spectral distribution is known exactly only in the kinetic limit approximation ($y = 0$). The approach taken in this section will be to calculate the interferogram analytically in that limit. The result of this calculation is convenient to use and, as it turns out, will require only a simple modification to account for the presence of Brillouin scattering in the true scattered spectrum ($y > 0$).

In the kinetic limit ($y = 0$), the spectrum of Rayleigh-Brillouin scattered light is Gaussian (eqn. 2.6). The spectrum due to aerosols, if present, is effectively a delta function (eqn. 2.8). The interferogram produced by the sum of these two components is found simply by applying eqns. 3.18 and 3.13 to the composite spectrum (eqn. 2.9) to obtain

$$I_2(\tau) = \frac{I_m + I_a}{2} n_0 [1 + n_I V(\tau) \cos 2\pi\nu_0\tau] \quad (3.19)$$

where

$$V(\tau) = \frac{I_m}{I_m + I_a} \exp(-\pi b^2 \tau^2 T) + \frac{I_a}{I_m + I_a} \quad . \quad (3.20)$$

As before b is assumed to be a constant and is defined as follows:

$$b^2 = \frac{|\vec{k}|^2 k_B}{2\pi M}$$

where \vec{k} is the vector difference between the wave vectors of the incident and scattered light, k_B is Boltzman's constant, and M is taken to be the average molecular mass of the scattering gas. Using appropriate values for the constants eqn. 3.19 is shown graphically in fig. 3.3. Although aerosol scattering is expected to be negligible compared to molecular scattering ($I_a \ll I_m$) they are shown to be of comparable magnitude in the figure for clarity. From eqn. 3.20 it can be seen that in the kinetic limit approximation the fringe visibility function is simply the sum of a Gaussian and a constant and that the width of the Gaussian depends explicitly on the gas temperature.

This completes the calculation of the interferogram of light scattered from air in the kinetic limit. The important results of this section are the functional form of the interferogram (eqn. 3.19) and the consequence that the fringe visibility function $V(\tau)$ depends explicitly on the temperature of the scattering gas. In Chapter 4 it will be shown that by frequency shifting one arm of the interferometer with respect to the other and synchronously detecting the output, it is possible to

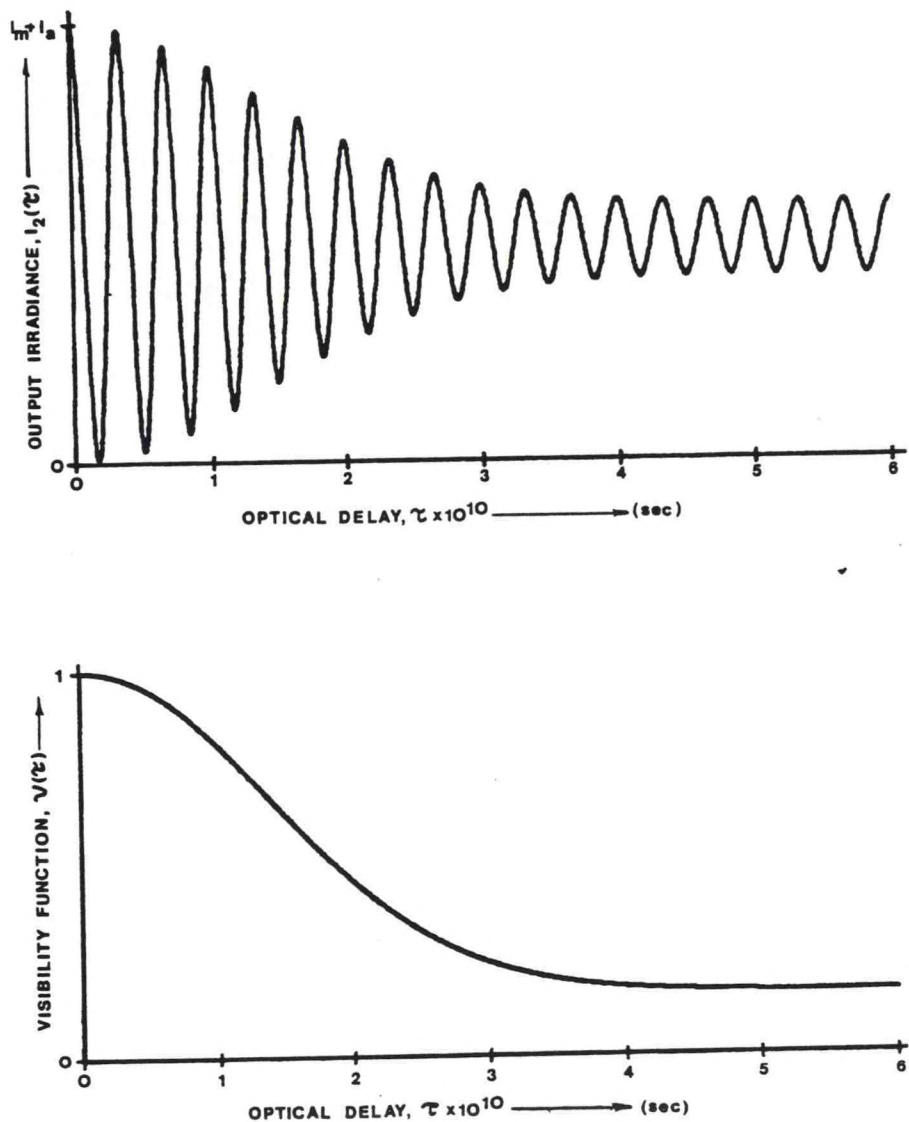


Fig. 3.3 Interferogram and Fringe Visibility Function Due to Light Scattered from Air in the Kinetic Limit ($y = 0$).

The interferogram is shown in (a) and the fringe visibility function in (b). ($\lambda = 514.5$ nm, backscatter, $T = 300$ K. Fringe spacing is shown greatly enlarged for clarity.)

measure a signal proportional to the fringe visibility. By monitoring this signal, changes in the temperature of the scattering gas may be determined.

Fixed Delay Michelson Interferometer as a Temperature Sensor

The usual approach in transform spectroscopy is to completely determine the interferogram and then transform it to determine the input spectrum. However, in the problem at hand a great deal of *a priori* knowledge exists concerning the input spectrum. Consequently, a detailed knowledge of the interferogram is unnecessary.

It has been shown previously that since the spectrum of light scattered from air is symmetric (eqn. 2.9), all spectral profile information is contained in the fringe visibility function $V(\tau)$. In the last section it was shown that for this spectrum the width of the visibility function depends on the temperature of the air. In this section we will exploit this fact. Specifically, I show that in the kinetic limit ($y = 0$) with no aerosols present it is only necessary to monitor the fringe visibility function at a single optical delay in order to measure temperature. Later I show that this also holds true under normal atmospheric conditions ($y > 0$).

The motivation for operating at a single fixed delay is simplicity in the instrument. Most of the complexity associated with the usual transform spectrometers arises from the need to vary the optical delay in order to sample the entire interferogram. By operating at a single fixed delay, all of that complexity is eliminated leaving an instrument

that is very simple and inexpensive, and one that could be made quite rugged.

It will also be shown that in spite of its simplicity, the fixed delay Michelson interferometer makes very efficient use of the available signal light. It was because of the inherent simplicity and efficiency that this instrument was chosen as the leading candidate for remote air temperature measurement in the laboratory that supported the work reported here.

The Basic Relationship

We begin this discussion by explicitly relating the temperature of the scattering gas to signals derived from the output of the interferometer (eqn. 3.18). The exact origin of these signals will be detailed in Chapter 4, but for now let us assume that experimentally it is possible to measure a signal S that is proportional to the fringe visibility function $V(\tau)$ and total input irradiance $(I_m + I_a)$,

$$S(\tau, T) = C [I_m(T) + I_a] V(\tau, T) , \quad (3.21)$$

and a signal S_o that is proportional only to the total scattered irradiance,

$$S_o(T) = D[I_m(T) + I_a] . \quad (3.22)$$

Here, the temperature dependence of $I_m(T)$ (see eqn. 2.9) is shown explicitly. The constants of proportionality include many factors such as

interferometric and overall system efficiencies, detector responsivity, amplifier gains, etc. Writing S in terms of eqn. 3.20 one obtains

$$S(\tau, T) = C\{I_m(T) \exp(-\pi b^2 \tau^2 T) + I_a\} . \quad (3.23)$$

The first term in this expression is the signal due to molecular scattering and the second term is the signal due to aerosol scattering. This expression may be easily solved for temperature in the exponential to obtain the following relationship:

$$T = -\frac{1}{\pi b^2 \tau^2} \ln \left[\frac{S(\tau, T) - C I_a}{C I_m(T)} \right] . \quad (3.24)$$

The second term in the numerator of this expression is the signal contribution due to aerosol scattering alone. Let us denote this term as S_a , $S_a \equiv C I_a$.

If a calibration temperature T' is available, the measurement of the absolute temperature T is greatly simplified. In this case T is given by

$$T = -\frac{1}{\pi b^2 \tau^2} \ln \left[\frac{S(\tau, T) - S_a}{S(\tau, T') - S_a} \cdot \frac{I_m(T')}{I_m(T)} \right] + T' . \quad (3.25)$$

Finally, to get rid of the second term in the argument of the logarithm, we make use of the other available signal $S_o(T)$ (eqn. 3.22). Solving eqn. 3.22 for $I_m(T)$ and inserting it into eqn. 3.25 one obtains

$$T = \frac{-1}{\pi b^2 \tau^2} \ln \left[\frac{S(\tau, T) - S_a}{S(\tau, T') - S_a} \cdot \frac{S_o(T') - S_{oa}}{S_o(T) - S_{oa}} \right] + T' \quad (3.26)$$

where the contribution to $S_o(T)$ due to aerosols has been denoted S_{oa} .

This expression gives the absolute temperature of the scattering gas in terms of a calibration temperature and signals measurable with a Michelson interferometer. However, to obtain all of these signals, measurements at two different optical delays would be required.

Further simplification occurs if the signals due to aerosol scattering are negligible compared to $S(\tau, T)$ and $S_o(T)$. In this case the above expression reduces to the following form:

$$T = - \frac{1}{\pi b^2 \tau^2} \ln \left[\frac{S(\tau, T)/S_o(T)}{S(\tau, T')/S_o(T')} \right] + T' . \quad (3.27)$$

Since operation of the interferometer at a single fixed delay provides both $S(\tau, T)$ and $S_o(T)$, eqn. 3.27 may be solved. Thus, if no aerosols are present, the absolute temperature of the scattering gas may be determined from a calibration temperature and signals available from a single, fixed-delay Michelson interferometer.

Equation 3.27 is based on the assumption that the scattered spectrum is purely Gaussian. It was shown in Chapter 2 that the true scattered spectrum departs significantly from the Gaussian form at air pressures near 1 atmosphere. However, it will be shown later that for optical delays of interest, the interferogram of Rayleigh-Brillouin ($y > 0$) scattered light departs only slightly from that calculated for

the kinetic limit ($y = 0$) approximation. Anticipating these results we will assume here that the correction necessary to eqn. 3.27 may be applied as a simple multiplicative factor, F_c . In general, F_c will depend on many things: the calibration temperature T' , the measured temperature T , the optical delay τ , and pressure P . However, it will be shown in the next section that the correction factor F_c depends strongly only on the optical delay τ and that approximate values for the other parameters suffice. Applying this correction factor, eqn. 3.27 becomes

$$T = \frac{-F_c}{\pi b^2 \tau^2} \ln \left[\frac{S(\tau, T)/S_o(T)}{S(\tau, T')/S_o(T')} \right] + T' \quad (3.28)$$

Equation 3.28 provides the theoretical basis of this investigation. In the next chapter I show how the signals $S(\tau, T)$ and $S_o(T)$ are obtained by frequency shifting one arm of the interferometer with respect to the other. Then the remainder of the dissertation is devoted to the experimental verification of the relationship. Before proceeding however we must address the question of uncertainty in the determination of T . This uncertainty results primarily from noise present in the output signals although other factors also contribute.

Uncertainty

We now estimate the uncertainty inherent in determining temperature T using eqn. 3.26 with the multiplicative factor F_c added and assuming the aerosol contributions are negligible. The approach taken is to note that T is a function of all of the variables on the right

hand side of eqn. 3.26 $T = f[\tau, S(\tau, T), S_a \dots]$ so that the uncertainty in T may then be estimated by using the following relationship:³⁵

$$\Delta T \approx \left[\left(\frac{\partial f}{\partial \tau} \right)^2 (\Delta \tau)^2 + \left(\frac{\partial f}{\partial S} \right)^2 (\Delta S)^2 + \dots \right]^{1/2} \quad (3.29)$$

where the assumption is made that the various partial derivatives are uncorrelated. The notation is simplified if we drop the functional dependences of S and S_o , for example $S(\tau, T')$ becomes S' . We also assume that S_a and S_{oa} are negligible compared to S and S_o respectively in the final result and that $S \approx S'$ and $S_o \approx S_o'$. Finally, we will assume that the fractional uncertainties in the signals measured at different temperatures are approximately equal.

With these simplifications the following result is obtained:

$$\begin{aligned} \Delta T \approx & \left\{ \left[2(T - T') \frac{\Delta \tau}{\tau} \right]^2 + 2A^2 \left[\frac{\Delta S}{S} \right]^2 + 2A^2 \left[\frac{\Delta S_o}{S_o} \right]^2 \right. \\ & + A^2 \left[\frac{S' - S}{S} \right]^2 \left[\frac{\Delta S_a}{S} \right]^2 \\ & \left. + A^2 \left[\frac{S_o' - S_o}{S_o} \right]^2 \left[\frac{\Delta S_{oa}}{S_o} \right]^2 + \left[\Delta T' \right]^2 + \left[(T - T') \frac{\Delta F_c}{F_c} \right]^2 \right\}^{1/2} \quad (3.30) \end{aligned}$$

where, $A \equiv \frac{-1}{\pi b^2 \tau^2}$. To give this result some perspective, Table 3.1 summarizes the temperature uncertainty obtained by assuming reasonable values for the uncertainties in eqn. 3.30. In this example $T = 300$ K, $T' = 290$ K, $\tau = 1.67 \times 10^{-10}$ s (OPD = 5 cm), and aerosol scattering is

Table 3.1.--Uncertainties Contributing to the Measurement of Temperature.

An example of the contributions of various sources of uncertainty to the total uncertainty in temperature. In this example $T = 300$ K, $T' = 290$ K, $\tau = 1.67 \times 10^{-10}$ s (OPD = 5 cm). Aerosol scattering is assumed to be negligible.

Source and Magnitude of Uncertainty	Squared Contribution to Total
Fractional uncertainty in optical delay	$\frac{\Delta\tau}{\tau} = 0.05$ 0.25 K^2
Fractional uncertainty in signals S, S'	$\frac{\Delta S}{S} = 0.001$ 0.35 K^2
Fractional uncertainty in signals S_o, S'_o	$\frac{\Delta S_o}{S_o} = 0.001$ 0.35 K^2
Fractional uncertainty in aerosol contribution to S	$\frac{\Delta S_a}{S} = 0.01$ 0.06 K^2
Fractional uncertainty in aerosol contribution to S_o	$\frac{\Delta S_{oa}}{S_o} = 0.01$ 0.02 K^2
Total uncertainty in calibration temperature	$\Delta T' = 0.3 \text{ K}$ 0.09 K^2
Fractional uncertainty in correction factor	$\frac{\Delta F_c}{F_c} = 0.01$ 0.01 K^2 _____ 1.13 K^2
Estimated total uncertainty in measurement, $\Delta T = 1.1 \text{ K}$	

assumed to be negligible. The important results of this summary are that: (1) the major source of uncertainty in T arises from uncertainty in the signal levels S , S' , S_o , and S'_o , (2) so long as aerosol scattering is less than a few percent of the main signal then it has a negligible contribution to the uncertainty in T , and that (3) similarly, uncertainty in the correction factor may be as high as a few percent without appreciably affecting the calculated value of T .

Fringe Visibility Function of Rayleigh-Brillouin ($y > 0$)
Scattered Light and Calculation of F_c .

Generally throughout this chapter we have assumed that the spectrum of scattered light is Gaussian. Based on this assumption, the resulting interferogram and fringe visibility functions were calculated and in the last section these results were used to obtain an expression for calculating the temperature T . Although the Gaussian approximation is convenient, it is not accurate for conditions found in the lower atmosphere, as was shown in Chapter 2. In this section the results of calculating the true fringe visibility function due to Rayleigh-Brillouin scattering are presented and this information is then used to calculate the correction factor F_c necessary to eqn. 3.28.

Using Yip and Nelkin's model²¹ the true Rayleigh-Brillouin scattered spectrum may be easily calculated for a range of temperatures and pressures (see for example fig. 2.4). From these results the Michelson fringe visibility function may be calculated by using eqn. 3.20. The results for three pressures are shown in fig. 3.4, including the case for $y = 0$. It is interesting to note at OPDs of interest

(about 5 to 6 cm) the visibility functions are very nearly equal, indicating a low sensitivity to pressure changes (or uncertainty in pressure). To pursue this result further, the derivatives with respect to temperature and pressure have also been calculated and are shown in fig. 3.5. The important result of this calculation is that for OPDs of interest, the fringe visibility function, and therefore the output of the interferometer, is much less sensitive to pressure changes than to temperature changes. For example, if we assume that pressure may be estimated to within 6 mbar (see Chapter 2), then it can be seen from fig. 3.5 that this uncertainty in pressure is negligible for a temperature measurement of 1 K resolution. Similar calculations for standard atmospheric conditions for heights from 0 to 10 km yield effectively these same results.

Next we turn our attention to calculating the correction factor F_c used in eqn. 3.28. The correction factor may be found by solving this equation for F_c and substituting the fringe visibility function $V(\tau, T)$ for $S(\tau, T)/S_o(T)$ and likewise $V(\tau, T')$ for $S(\tau, T')/(S_o(T'))$. For given values of T , T' , and P the fringe visibility function may be calculated and from these results F_c may be calculated directly. Values appropriate for the experimental work described in this dissertation are shown in fig. 3.6.

Since T is actually the measured quantity in the experiment, its value varies. Likewise, both T' and P may also vary depending on the experimental conditions. Fortunately, for OPDs of interest, the value of F_c is nearly independent of these parameters over reasonable

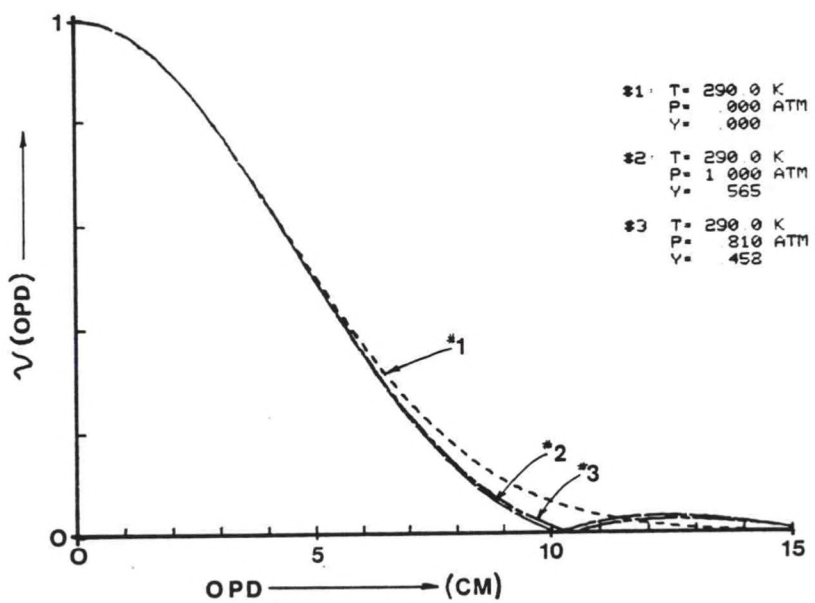


Fig. 3.4 Michelson Interferometer Fringe Visibility Function for Rayleigh-Brillouin Scattered Light.

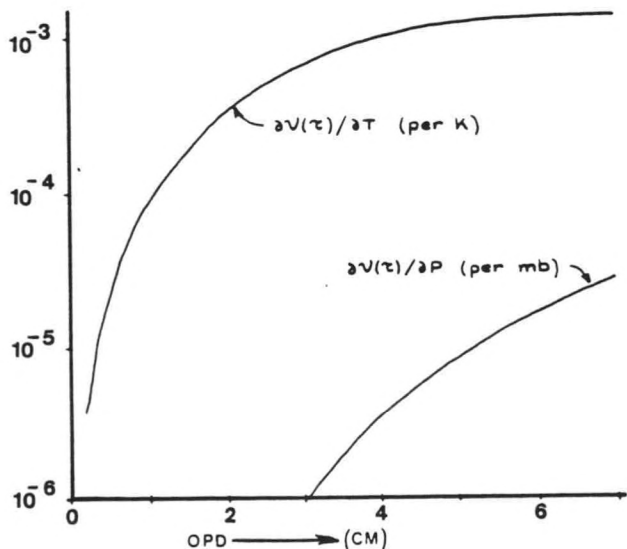


Fig. 3.5 Partial Derivatives of $V(\tau)$ with Respect to Temperature and Pressure.

($T = 290 \text{ K}$, $p = 1 \text{ atm}$). Calculations for atmospheric conditions from 0-10 km yield essentially these same results.

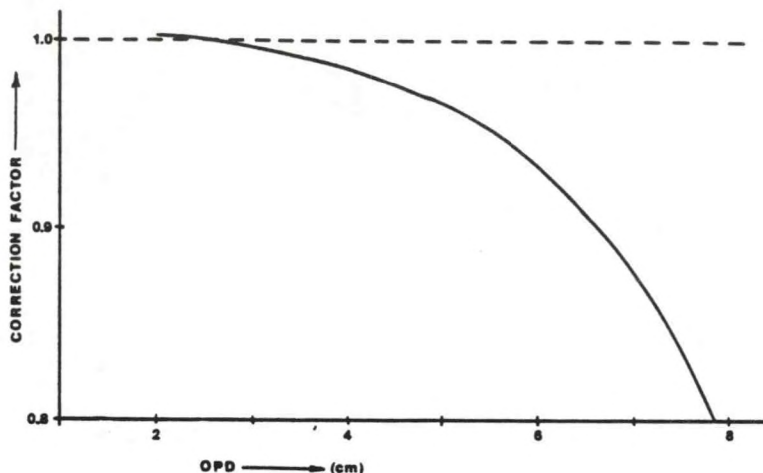


Fig. 3.6 Correction Factor F_c as a Function of OPD.

Nominal parameters are $T' = 295$ K, $T = 300$ K, $P = 0.803$ atm, and $\lambda = 514.5$ nm (backscatter).

temperature ranges. Table 3.2 summarizes the calculated percent changes in F_c resulting from the indicated changes in T , T' and P . It can be seen that for a given optical delay, the value of F_c is nearly constant over a range of experimental conditions. These results suggest that simple correction factors could be determined for atmospheric measurements where only estimates of T and P are available.

Performance: Fixed Delay Michelson Interferometer as a Near Optimum Spectral Filter

In this section the concept of regarding a fixed-delay Michelson interferometer as a spectral filter is developed. This concept is then used to compare the performance of a fixed-delay Michelson interferometer to that of other spectral filters in the role of a remote air temperature sensor. Here this analysis is applied to a classical Michelson interferometer even though the interferometer used in this investigation was actually a modified form, as described in the next chapter. This is done to provide a broad theoretical basis. Later the analysis is applied specifically to the interferometer used in this investigation.

Table 3.2.--Sensitivity of F_c to Changes in T' , T , and P .

Nominal values are $T' = 295$ K, $T = 305$ K, $P = 0.803$ atm,
 $\lambda = 514.5$ nm (backscatter).

Parameter and induced change	Resulting change in F_c at indicated OPD		
	4 cm	6 cm	8 cm
Nominal value of F_c	0.985	0.933	0.885
Calibration temperature, T' $\Delta T' = \pm 5$ K	0.1%	<0.1%	0.3%
Measured temperature, T $\Delta T = \pm 15$ K	<0.1%	0.2%	1.0%
Pressure, P $\Delta P = \pm 10$ mbar	<0.1%	<0.1%	0.1%

Fixed delay Michelson interferometer as a spectral filter

In this analysis it is convenient to regard a fixed-delay Michelson interferometer as a simple spectral filter. This concept is particularly useful for comparing this type of interferometer with the Fabry-Perot interferometer. To understand this viewpoint consider the example shown in fig. 3.7. In this example a simple spectral filter transmits a portion of the spectrum of the source radiation to the detector. Assuming the detector has a flat spectral response, the irradiance at plane P is $I_v(v)$, and the transmittance function of the filter is $F(v)$, then the output of the detector ξ is simply

$$\xi = R \int_0^{\infty} I_v(v) F(v) dv \quad (3.31)$$

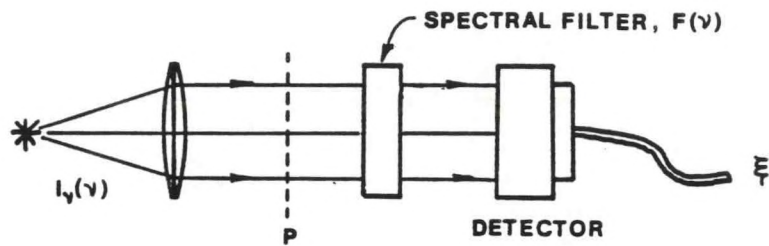


Fig. 3.7 A Simple Spectral Filter and Detector.

where R is a constant that depends on the detector and geometry of the setup. To see the similarity between this example and the output of a Michelson interferometer, we have only to write eqn. 3.10 in a slightly different way. The output of the interferometer is then

$$I_2(\tau) = \int_0^{\infty} I_v(v) \frac{1}{2}[1 + \cos 2\pi v\tau] dv. \quad (3.32)$$

If the output of the interferometer is collected by a detector of uniform spectral response its output would be

$$\xi' = R' \int_0^{\infty} I_v(v) \frac{1}{2}[1 + \cos 2\pi v\tau] dv. \quad (3.33)$$

Clearly, the interferometer acts as a spectral filter with a transmittance function

$$F'(v, \tau) = \frac{1}{2}[1 + \cos 2\pi v\tau]. \quad (3.34)$$

This is shown graphically in fig. 3.8.

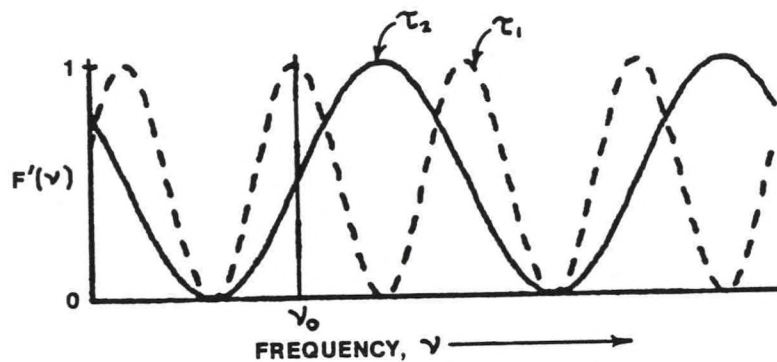


Fig. 3.8. Filter Function of a Fixed-Delay Michelson Interferometer.
The filter functions are shown for two different optical delays.

To get a better feeling for this point of view, consider the case where the input spectrum is effectively a delta function (e.g., from a gas laser) at frequency v_0 . Referring to fig. 3.8, one can see that by adjusting the interferometer to a delay τ_1 all of the input light is passed through the interferometer. This corresponds to a "bright fringe". Adjustment of the delay to τ_2 corresponds to a near "dark fringe".

Regarding the fixed-delay Michelson interferometer as a spectral filter allows one to understand its operation as a frequency space filter. By extending the concept, one can get an intuitive grasp of some of the concepts often associated with Fourier transform spectroscopy, such as the "multiplex advantage". However, this topic will not be pursued here.

Fixed-delay Michelson interferometer as a near optimum spectral filter and MDTC

We now turn our attention to applying the spectral filter concept to the problem at hand in order to evaluate the performance of various spectral filters, including the fixed-delay Michelson interferometer. The evaluation is based on the spectral filter's ability to efficiently use the available signal to produce an output that is sensitive to changes in spectral width and therefore temperature. It will be shown that if a single measurement is to be made then the fixed-delay Michelson interferometer has an advantage over a Fabry-Perot interferometer. This topic has been pursued rigorously using estimation theory in a recent paper by Lading and Jensen.⁵ The development here arrives essentially at their result but in a more intuitively appealing way by regarding the Michelson interferometer as a spectral filter. Throughout this development it is assumed that the limiting source of noise in the measurement is signal shot noise. In Chapter 6 it is shown that experimentally this condition is achieved.

Conceptually, the usual spectroscopic approach to measuring spectral width would be to scan the spectrum with a high resolving power (narrow bandwidth) instrument to determine the entire spectral profile. The width could then be measured directly from the recorded profile. However, in the case at hand this process would be very inefficient and unnecessarily complicated. The inefficiency results because all signal power outside the passband of such an instrument is wasted in the sense that it does not contribute to the output.

In the approach taken here, the input spectrum is passed through a single, fixed spectral filter to produce an output that is a continuous measure of the width of the input spectrum. This idea is shown conceptually in fig. 3.7. In order to compare the efficiency of different spectral filters, a figure of merit is required. For this measure I have chosen the minimum detectable temperature change (MDTC) which I have defined as the temperature change that produces a change in the output $\xi(T)$ equal to the RMS noise fluctuations. Thus,

$$MDTC \equiv \left| \frac{\xi_N}{\partial \xi(T) / \partial T} \right| \quad (3.35)$$

where ξ_N is the RMS change in $\xi(T)$ due to noise. The square root of this figure of merit is equal to the maximum likelihood estimator used by Lading and Jensen.⁵

As an example of the use of this figure of merit, consider the simple example shown in fig. 3.9. The spectral filter is rectangular with a unity transmission inside the passband and zero outside. The width and center frequency of the filter are adjustable parameters. In this example, and throughout this section, it is assumed that total power P_o in the integrated spectrum remains constant.

In general, the power transmitted to the detector is

$$P(T) = A \int_0^{\infty} I_v(v) F(v) dv \quad (3.36)$$

where A is the collected area of the output beam.

If the detector has a responsivity of R (amps/watt), then the output and RMS shot noise are

$$\xi(T) = R P(T) \quad (3.37)$$

$$\xi_N = [2e R P(T) \Delta f]^{1/2} \quad (3.38)$$

where e is the charge of the electron and Δf is the signal bandwidth of the electronics. The MDTC is now easily expressed in terms of eqns. 3.37 and 3.38 as

$$MDTC = \left[\frac{2e \Delta f}{R} \right]^{1/2} \frac{P(T)^{1/2}}{\partial P(T)/\partial T} \quad (3.39)$$

We are now ready to apply this analysis to the problem at hand.

Figure 3.9 summarizes the results of numerically calculating MDTC using eqns. 3.39, and 2.9 with aerosol scattering (I_a) set to equal to zero. The partial derivative was approximated as simply

$$\partial P(T)/\partial T = [P(T_2) - P(T_1)]/[T_2 - T_1].$$

Note that an optimum value exists for both the width and center frequency of the filter.

This same analysis can be applied to a fixed-delay Michelson interferometer by using eqn. 3.34 as the filter function

$$F'(\nu, \tau) = \frac{1}{2} (1 + \cos 2\pi\nu\tau) \quad (3.34)$$

where τ is the only adjustable parameter. One finds that in this case MDTC is minimized when $\tau = n/\nu_o$ or $\tau = (n + 1/2)/\nu_o$ where n is an

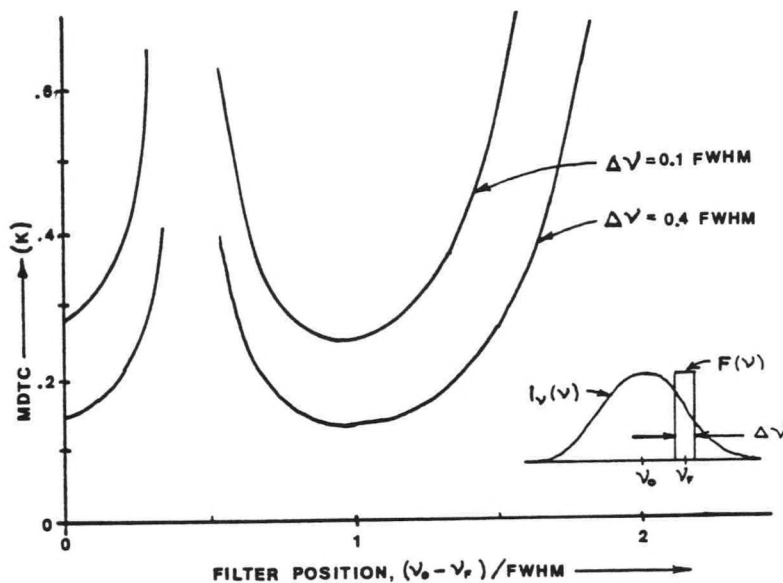


Fig. 3.9 MDTC for a Rectangular Filter Function.

Parameters used are: $P = 5.7 \times 10^{-10}$ watts, $R = 0.027$ amps/watt, $\Delta f = 1$ Hz. Little improvement was observed for filters wider than 0.4 FWHM.

integer and v_o is the center frequency of the Gaussian input spectrum. These conditions correspond to a "bright fringe" and a "dark fringe" respectively at the output of the interferometer. Assuming that one of the above conditions is satisfied, then the remaining degree of freedom in the filter is its period. The period of the filter is $1/\tau$, which for the two conditions mentioned above becomes v_o/n or $v_o/(n+1)$. Since n is a very large number ($\sim 10^6$) in this application, the range of periods is essentially continuous.

Figure 3.10 summarizes the results of applying the MDTC analysis to the Michelson interferometer. Note that in this case the results

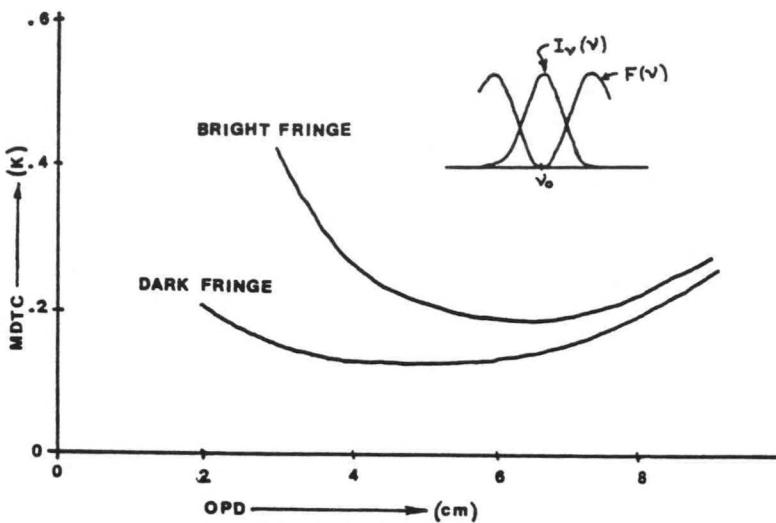


Fig. 3.10 MDTC for a Fixed-Delay Michelson Interferometer.
Parameters are given in fig. 3.9.

are comparable to those obtained with the rectangular filter of fig. 3.9. Also, it is interesting that the dark fringe condition provides a slightly lower MDTC than the bright fringe condition. This occurs since in both cases $\xi P(T)/\partial T$ is roughly the same but in the dark fringe condition less total light strikes the detector and therefore the noise level is less. Operating in this mode has been suggested by Schwiesow and Lading⁶ who have proposed making atmospheric temperature measurements with a Michelson interferometer actively locked to the dark fringe condition.

We can also apply the MDTC analysis to a Fabry-Perot interferometer for comparison with the above results. In this case the filter function is given by⁴¹

$$F(v) = [1 + (4 F^2/\pi^2) \sin^2(2\pi v d/c)]^{-1} \quad (3.40)$$

where F is the finesse, d is the plate separation (an air spaced etalon is assumed), and c is the velocity of light. Applying eqn. 3.40 to eqns. 3.36 and 3.39 as before, we get the results summarized in fig. 3.11. Note that in no case is the MDTC for the Fabry-Perot interferometer lower than that for the Michelson interferometer. Simply put, in the type of processor considered here, the fixed-delay Michelson interferometer makes better use of the available signal.

Finally, it should be noted that in the case of the Michelson interferometer MDTC may also be evaluated analytically using eqn. 3.14 and the definition of MDTC. In terms of eqn. 3.14 the power at the output of the detector is

$$P = A I_m [1 + V(\tau) \cos 2\pi\nu_o \tau] \quad (3.41)$$

where A is the collected area of the output beam and I_m is the total irradiance. Using eqns. 3.37, 3.41 and 3.20 and the expression for shot noise as before (eqn. 3.38) the following expression for MDTC is obtained:

$$\text{MDTC} = \frac{1}{\pi b^2} \left[\frac{4e \Delta F}{R I} \right]^{1/2} \frac{[1 + \exp(-\pi b^2 \tau^2 T) \cos \theta]^{1/2}}{\tau^2 \exp(-\pi b^2 \tau^2 T) \cos \theta} \quad (3.42)$$

where $\theta \equiv 2\pi\nu_o \tau$

$$b \equiv \frac{|\vec{K}|^2 K_B}{2\pi m} .$$

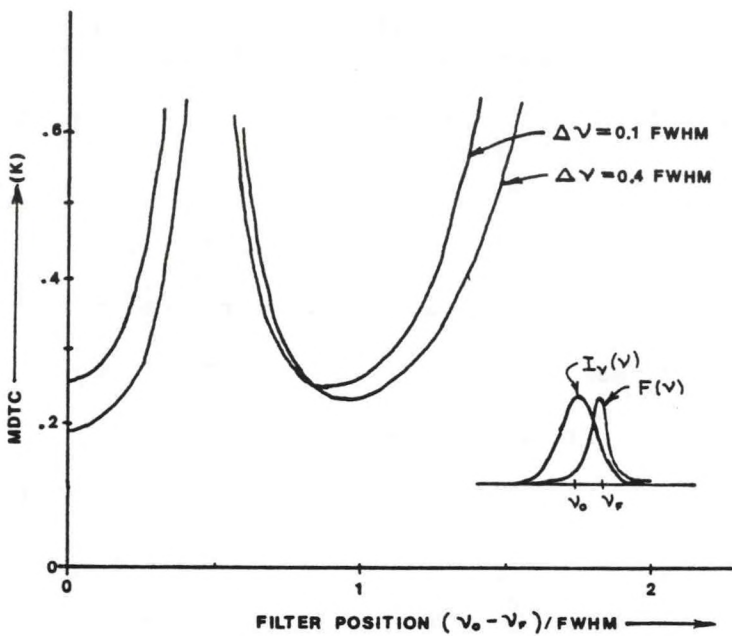


Fig. 3.11 MDTC for a Fabry-Perot Interferometer.

Parameters are given in fig. 3.9 with $F = 5$. Minimum MDTC occurred when $\Delta v \approx 0.4$ FWHM.

For comparison with the results of the numerical calculation summarized in fig. 3.10, note that the "bright fringe" condition corresponds to $\theta = 2\pi n$ and the "dark fringe" case corresponds to $\theta = 2\pi n + \pi$ where $n = 0, 1, 2, \dots$. A quick check would reveal agreement between eqn. 3.42 and fig. 3.10.

This concludes the comparison between the Michelson and Fabry-Perot interferometers. It was shown that both may be regarded as spectral filters and that as such, the Michelson interferometer makes better use of the available signal for measuring small changes in spectral linewidth. In the next chapter the concept of frequency shifting the interferometer is introduced and the modified Michelson interferometer actually used in this investigation is described.

CHAPTER 4

FREQUENCY SHIFTING THE INTERFEROMETER

In the last chapter we studied the fixed-delay Michelson interferometer. It was pointed out that such an interferometer has two characteristics that are important in the measurement of spectral linewidths (and therefore temperature): it makes very efficient use of the available signal and it is nearly insensitive to pressure effects in the spectrum of Rayleigh-Brillouin scattered light. In practice however, an important complication arises when operating at a fixed optical delay.

First, recall that spectral profile information, and therefore temperature information, are contained in the fringe visibility function $V(\tau)$. Referring to eqn. 3.19 however one can see that the output of the interferometer is also strongly dependent on the cosine term which represents the fringes.

$$I_2(\tau) = I_m + I_a \eta_o \{1 + \eta_I V(\tau) \cos 2\pi v_o \tau\} . \quad (3.19)$$

The difficulty arises when v_o and τ are not constant (v_o is the center frequency of the scattered spectrum and τ is the optical delay introduced by the interferometer). For example, if the interferometer was originally adjusted to a fringe maximum at an optical delay of 2×10^{-10} s (OPD \approx 3 cm) and with $\lambda_o = c/v_o = 514.5$ nm then a 1% change in output would result from a frequency shift of only $\Delta v_o = 160$ MHz. Similarly

this change could be caused by a mirror displacement of 0.016 waves (8.2×10^{-6} mm). The result is that the output of the interferometer would change with drifts in absolute frequency or mechanical mirror position as well as with changes in the temperature of the scattering gas. The sensitivity to absolute frequency is particularly troublesome because it is difficult to obtain such a degree of stability from a laser without active stabilization.

Active stabilization would be one way of overcoming the problem. Schwiesow and Lading⁶ have suggested actively locking a Michelson interferometer to a fringe extremum. For the purposes of this investigation a more convenient method was to frequency shift one arm of the interferometer relative to the other. This produced a moving fringe pattern which provided an AC signal output from the interferometer the amplitude of which was proportional to the fringe visibility. Only the phase of the output signal was affected by changes in v_o or small changes in τ . By choosing a signal processor that measured only the amplitude of the signal, an output was obtained that was independent of laser frequency (v_o) drift and small changes in optical delay (τ).

This chapter begins with an explanation of the frequency shifting technique used, after which I return to the interferometer and describe its operation as a polarization interferometer. In the last section signal processing is covered.

Frequency Shifting Technique

The idea of frequency shifting one arm of an interferometer relative to the other is not new to transform spectroscopy. Various ideas have been suggested from time to time although none have found widespread use. Most of the ideas that have been implemented have relied on some type of mechanical mirror movement. Indeed, the translation of one of the mirrors causes a frequency shift in that arm due to the Doppler effect. However, in that case the OPD varies continuously. The discussion here is restricted to techniques in which the OPD is effectively constant.

Chamberlain³⁶ has used a scheme of dithering one of the interferometer mirrors in and out to produce a phase modulation in one arm of an interferometer. This technique does produce a modulated output for the interferometer but the sensitivity to drift in v_0 and τ still remains. Lading and Jensen⁵ have recently suggested the use of an acousto-optic Bragg cell in each arm of the interferometer to frequency shift both arms. However, since the Bragg cells are within the interferometer, optical phase distortion is a problem. The technique described below relies on components that are outside of the interferometer and produce a sinusoidal output at the detector, the amplitude of which is proportional to $V(\tau)$ but independent of drifts in v_0 and τ .

In the early sixties a group of researchers at General Telephone and Electronics Laboratories used electro-optic devices to produce what they termed a single-sideband suppressed-carrier optical modulator.^{37,38,39} The basic idea was that a rotating birefringent plate could frequency

shift a component of the light passing through it. In effect they were able to produce a frequency shift in a narrowband optical beam, albeit with low efficiency. However, the basis of their technique has since been used successfully in optical testing to produce fringe scanning interferometers.

In optical testing fringe scanning interferometers are used when high accuracy is required in determining the shape of a wavefront returned from the test arm of the interferometer. The scanning fringes are produced by frequency shifting one arm of the interferometer relative to the other arm. This was first implemented by Crane⁴⁰ who placed a stationary $\lambda/4$ plate and a rotating $\lambda/2$ plate in the reference arm of the interferometer. A great improvement was introduced by Sommargren⁴¹ who showed that a rotating $\lambda/2$ plate followed by a stationary $\lambda/4$ plate external to the interferometer could be used instead. The advantage of this scheme is that since the components are external to the interferometer only modest optical quality is required. Recently, an extension of this technique has also been described for obtaining larger frequency shifts.⁴² It is the technique proposed by Sommargren that I have used in this investigation. In the following paragraphs I will briefly review the basic theory of his frequency shifter.

The frequency shifter consists simply of a rotating $\lambda/2$ plate followed by a stationary $\lambda/4$ plate as shown in Fig. 4.1. Following Sommargren, I will use the Jones calculus⁴³ to describe the waveplates and the polarization states throughout. Assuming a unit amplitude, horizontally polarized plane wave is incident on the $\lambda/2$ plate, the

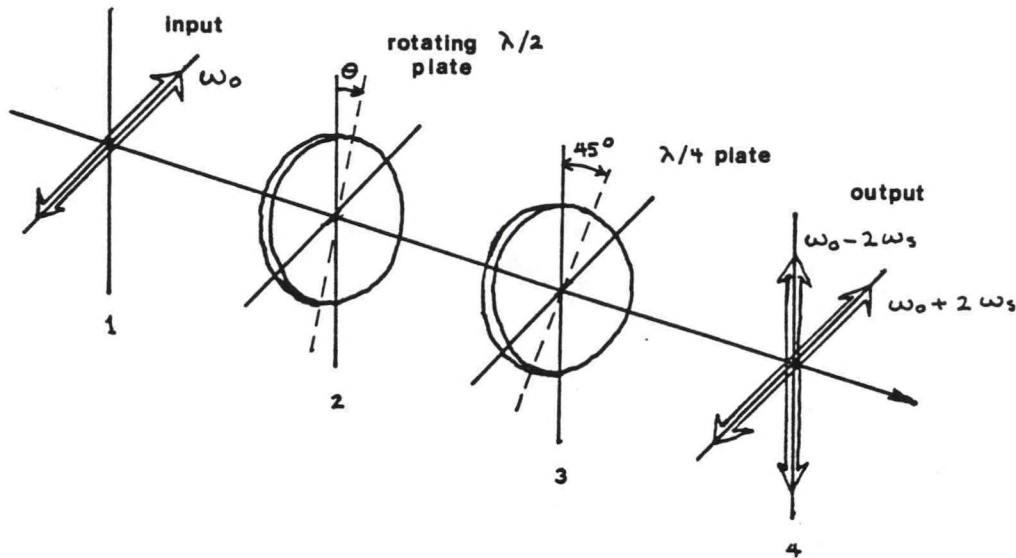


Fig. 4.1 Rotating Waveplate Frequency Shifter.

electric field may be described by

$$E_1(z, t) = e^{i(kz - \omega_0 t)} \hat{x} = \begin{bmatrix} 1 \\ 0 \end{bmatrix} e^{-i\omega_0 t}. \quad (4.1)$$

As usual, the space dependence is implicit in the matrix representation.

The beam first encounters a $\lambda/2$ plate rotating about the z axis at rate ω_s . If the instantaneous angle of the fast axis with respect to the vertical is θ , such that $\theta = \omega_s t$, then the waveplate is described by the matrix,

$$i \begin{bmatrix} \cos 2\theta & \sin 2\theta \\ -\sin 2\theta & \cos 2\theta \end{bmatrix}. \quad (4.2)$$

The output from the first waveplate is

$$E_2(t) = i \begin{bmatrix} \cos 2\theta & \sin 2\theta \\ -\sin 2\theta & \cos 2\theta \end{bmatrix} \begin{bmatrix} 1 \\ 0 \end{bmatrix} e^{-i\omega_0 t} = i \begin{bmatrix} \cos 2\theta \\ \sin 2\theta \end{bmatrix} e^{-i\omega_0 t}. \quad (4.3)$$

At this point the beam is simply linearly polarized but with its angle with respect to the vertical changing at a rate 2θ . As Sommargren points out, it is helpful at this point to express the beam as the sum of right- and left-circular components:

$$E_2(t) = i \begin{bmatrix} \frac{1}{2}(e^{i2\theta} + e^{-i2\theta}) \\ -\frac{1}{2}(e^{i2\theta} - e^{-i2\theta}) \end{bmatrix} e^{-i\omega_0 t} = \frac{i}{2} \left\{ \begin{bmatrix} 1 \\ -i \end{bmatrix} e^{-i(\omega_0 t - 2\theta)} + \begin{bmatrix} 1 \\ i \end{bmatrix} e^{-i(\omega_0 t + 2\theta)} \right\}$$

$$E_2(t) = i/2 \left\{ \begin{bmatrix} 1 \\ -i \end{bmatrix} e^{-i(\omega_0 - 2\omega_s)t} + \begin{bmatrix} 1 \\ i \end{bmatrix} e^{-i(\omega_0 + 2\omega_s)t} \right\}. \quad (4.4)$$

The terms in eqn. 4.4 represent a down shifted right-circular component and an upshifted left-circular component.

With its fast axis at 45° , the quarter wave plate acts on the left- and right-circularly polarized light to produce vertically and horizontally polarized light, respectively. Consequently, we would

expect the output of the quarter wave plate to be composed of an up-shifted vertically polarized component and a downshifted horizontally polarized component. The matrix representation of the $\lambda/4$ plate is,

$$\frac{\sqrt{2}}{2} e^{i\pi/2} \begin{bmatrix} -i & 1 \\ 1 & -i \end{bmatrix}$$

and the output from it is then

$$E_4(t) = -\frac{1}{\sqrt{2}} \left\{ \begin{bmatrix} -i \\ 0 \end{bmatrix} e^{-i(\omega_0 - 2\omega_s)t} + \begin{bmatrix} 0 \\ 1 \end{bmatrix} e^{-i(\omega_0 + 2\omega_s)t} \right\} . \quad (4.5)$$

We find the two orthogonal, frequency shifted linear polarization states as supposed above. Equation 4.5 may also be written in the following more compact form:

$$E_4(t) = -\frac{1}{\sqrt{2}} e^{-i\omega_0 t} \begin{bmatrix} e^{i2\omega_s t} \\ -i \\ e^{-i2\omega_s t} \end{bmatrix} . \quad (4.6)$$

The result of eqn. 4.6 is obtained for an incident plane wave of unit amplitude. The real optical signal dealt with in this experiment is neither of unit amplitude nor is it deterministic. However, in the case of quasi-monochromatic light, a simple modification of eqn. 4.6 suffices. If $E_0(t)$ is the analytic signal associated with the real optical signal,³³ then eqn. 4.6 becomes,

$$E_4(t) = -\frac{1}{\sqrt{2}} \begin{bmatrix} e^{i2\omega_s t} \\ -e^{-i2\omega_s t} \\ e^{-i\omega_o t} \end{bmatrix} E_o(t) \quad (4.7)$$

where the factor $e^{-i\omega_o t}$ has been included in $E_o(t)$.

In the next section the polarization properties of the interferometer used in this experiment are described. It is shown that with a simple modification, a Michelson interferometer can be used to delay one of the polarization states with respect to the other and then cause them to interfere at the output to produce a moving fringe pattern.

Application to the Michelson Interferometer

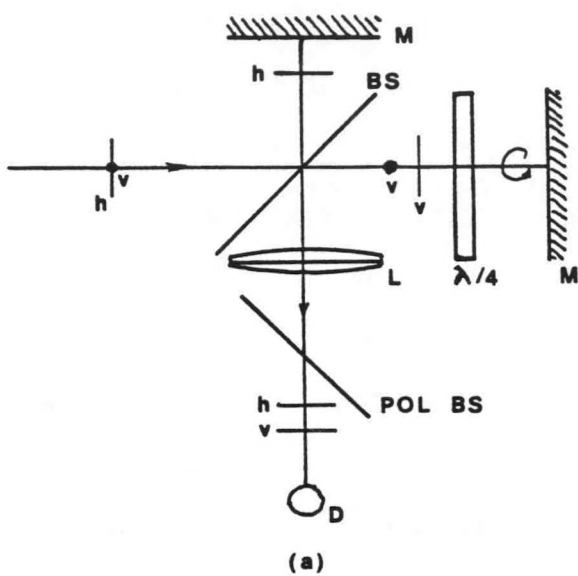
At the output of the frequency shifter the signal has been split into two orthogonal, linearly polarized components. One has been upshifted in frequency by an amount $2\omega_s$ and the other downshifted in frequency by the same amount. In order to get the interference we want, we need only to delay one component with respect to the other and then interfere them. Conceptually this could be done with a birefringent plate followed by a linear polarizer. Unfortunately, a very large thickness of birefringent material would be required to produce the optical delays of interest. For example approximately 30 cm of calcite would be required to produce an OPD of about 5 cm.

A commonly used alternative is the polarization interferometer.⁴⁴ In this device the two orthogonal polarization components are separated using a polarization beamsplitter or prism. An unequal delay is introduced to the beams which are then recombined and interfered. For a

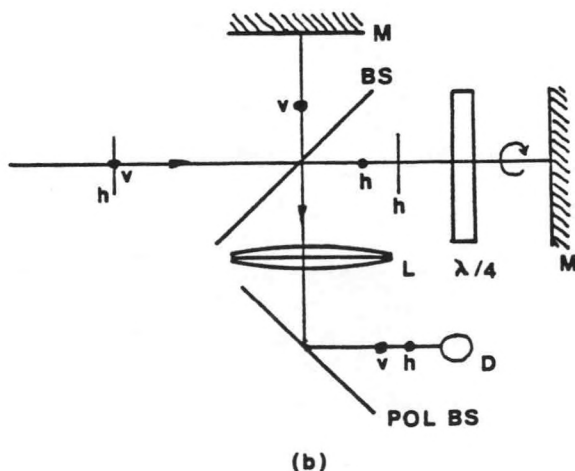
large aperture instrument however, the components involved can become quite expensive. The interferometer used in this investigation is a variation on this theme that is essentially a standard Michelson interferometer but with a single high quality quarter wave plate in one arm. Properly adjusted this interferometer can provide almost the same result as the more usual polarization interferometer described above.

A good way to understand the operation of the interferometer used here is to think of it as the sum of the two interferometers shown in fig. 4.2. For clarity, let us label the two components of the input beam as v and h for the vertically and horizontally polarized input beam components respectively. Since the beamsplitter is an ordinary dielectric beamsplitter, half of each of these components is transmitted and half is reflected. However, in fig. 4.2(a) for each component a single choice is shown: either the reflected part or the transmitted part, but not both. In fig. 4.2(b) the other choices are shown. Thus, the output of the actual interferometer consists of the sum of the outputs shown in figs. 4.2(a) and 4.2(b).

Following the operation of the interferometer, in fig. 4.2(a) it can be seen that part of the h component is reflected from the beam splitter, then reflects from the mirror, and then is partially transmitted through the beamsplitter to arrive at the output. Part of the v component is transmitted by the beamsplitter to the quarter wave plate. The quarter-wave plate is aligned with its fast axis at 45° to the vertical and consequently it converts the v component into circularly polarized light which changes its handedness on reflection from the



(a)



(b)

Fig. 4.2 The Modified Michelson Interferometer Used in This Investigation.

The interferometer can be thought of as the sum of the interferometers shown in (a) and (b). (M = mirror, L = lens, $\lambda/4$ = $\lambda/4$ plate, D = detector, BS = beamsplitter, POL BS = polarization beamsplitter).

mirror. Passing back through the quarter wave plate the v component becomes horizontally polarized. Part of it is reflected by the beam-splitter and arrives at the output ready to interfere with the h component.

At this point we have arrived at essentially the desired result. By adjusting the mirror separation, any reasonable OPD can be introduced between the v and h components. Furthermore, at the output the v and h components are polarized parallel to one another and therefore interfere effectively. Since there is a relative frequency shift of $4\omega_s$ between these interfering components, the output irradiance varies sinusoidally in time.

The interferometer shown in fig. 4.2(b) accounts for the transmitted and reflected components omitted in fig. 4.2(a). Its operation is effectively identical to that described above except that the two components arriving at its output are vertically polarized. As mentioned above the actual output of the interferometer consists of the sum of the components shown in figs. 4.2(a) and 4.2(b).

By now we have accounted for all beams in the interferometer except those that go back out the input. In this regard this interferometer is more like the classical Michelson interferometer than the usual polarization interferometer. In the usual polarization interferometer all of the input light arrives at the output. This same result could also be achieved with the type of interferometer described here if it were set up in the Mach-Zender configuration instead of the Michelson configuration. The Mach-Zender configuration however would require two

beamsplitters and would be difficult to arrange with a variable OPD.

The output of the interferometer may be written in terms of eqn. 4.6 as follows (cf. eqn. 3.2):

$$E(t, \tau) = \frac{1}{2} E_4(t+\tau) + \frac{1}{2} e^{i\pi/2} \begin{bmatrix} 0 & 1 \\ 1 & 0 \end{bmatrix} E_4(t) . \quad (4.8)$$

Here the optical delay τ is shown relative to an arbitrary time t , as in eqn. 3.5. Since the beam makes two passes through the quarter wave plate, it is represented as a half wave plate (at 45° to the vertical) in eqn. 4.8 with the appropriate Jones matrix.

Before evaluating the irradiance, the output beam must be passed through a polarization beamsplitter to separate the two polarization components as shown in fig. 4.2.

$$E_h(t, \tau) = \begin{bmatrix} 1 & 0 \\ 0 & 0 \end{bmatrix} E(t, \tau) \quad (4.9)$$

$$E_v(t, \tau) = \begin{bmatrix} 0 & 0 \\ 0 & 1 \end{bmatrix} E(t, \tau) .$$

The irradiance due to these components may be evaluated using the development of Chapter 3. For the horizontal component eqns. 4.9, 4.8, and 4.7 give

$$\begin{aligned} \langle E_h^* (t, \tau) E_h(t, \tau) \rangle &= \frac{1}{8} \{ \langle E_o^* (t) E_o(t) \rangle \\ &+ \langle E_o^* (t + \tau) E_o(t + \tau) \rangle \\ &+ 2 \operatorname{Re} \langle E_o^* (t + \tau) E_o(t) e^{i(4\omega_s t - \pi)} \rangle \} \end{aligned} \quad (4.10)$$

where use has been made of the approximation $\exp[i4\omega_s(t+\tau)] \approx \exp[i4\omega_s t]$ since $\tau \ll t$ (e.g., $\tau = 1.7 \times 10^{-10}$ s for an OPD of 5 cm). Since $\exp[i4\omega_s t - \pi]$ is deterministic, it may be moved out of the ensemble average indicated by the angle brackets $\langle \rangle$. Finally, identifying the self coherence function as in eqn. 3.6, we may rewrite eqn. 4.10 as

$$\langle E_h^* E_h \rangle = \frac{1}{4} [\Gamma(0) + \text{Re}[\Gamma(\tau) e^{i(4\omega_s t - \tau)}]] \quad . \quad (4.11)$$

If the self coherence function is broken up into its modulus $|\Gamma(\tau)|$ and phase $\Phi(\tau)$, this result may be written as

$$\langle E_h^* E_h \rangle = \frac{1}{4} \Gamma(0) \left\{ 1 + \frac{|\Gamma(\tau)|}{\Gamma(0)} \cos(\Phi(\tau) + 4\omega_s t - \pi) \right\} \quad . \quad (4.12)$$

Noting that the irradiance $I_h(\tau)$ at the output of the interferometer is simply $I_h(t, \tau) = c\varepsilon \langle E_h^* E_h \rangle$ (eqn. 3.3) and comparing eqn. 4.12 with eqn. 3.19 we finally get

$$I_h(t, \tau) = \frac{1}{4} I_1 \left\{ 1 + V(\tau) \cos(\omega_o \tau + 4\omega_s t - \pi) \right\} \quad . \quad (4.13)$$

This result is effectively the same as for the standard Michelson interferometer (cf. eqn. 3.14) except for a factor of 1/4 instead of 1/2 and the argument of the cosine which is now a function of time. The factor of 1/4 occurs since the output is divided evenly between the h and v channels. The argument of the cosine term causes the output of the interferometer to vary sinusoidally with time. Recall that the

cosine term of the interferogram represents the fringes. Therefore, in the case of eqn. 4.13 the fringes move continuously, just as they would if one of the mirrors were being translated. The troublesome term $\omega_0 \tau = 2\pi v_0 t$ now determines only the phase of the output. Thus, if the signal processor is AC coupled and sensitive only to the amplitude of the detector output, then small drifts in v_0 or τ will have no effect and the output of the signal processor would be proportional to $V(\tau)$.

To summarize, the rotating waveplate frequency shifter is capable of accepting a linearly polarized input beam and dividing it into two orthogonally polarized output beams that are shifted in frequency relative to one another. One beam is upshifted by an amount $2 \omega_s$ and the other downshifted by the same amount where ω_s is the angular rotation rate of the half-wave plate. If these two polarization components are then directed into the modified Michelson interferometer it produces two orthogonally polarized outputs. Each output is effectively the same as for the classical Michelson interferometer except that the argument of the cosine term changes linearly with time, in effect causing the fringes to move.

In the next section we consider the signal processing system which uses the output of the interferometer to produce a signal proportional to $V(\tau)$. Although the interferometer actually produces two outputs, only one is utilized in this experiment. This procedure was chosen purely for simplicity. Under other circumstances all of the available light could have been used.

Signal Processing

In this section we turn our attention to signal processing. Ultimately we wish to produce an output that is proportional to the fringe visibility function $V(\tau)$. Specifically, the output should not be affected by phase shifts in the signal. Since the frequency of the signal is known, and a reference signal is easily obtained from the rotating half-wave plate, a synchronous detection scheme is a natural choice for the processor. However, in order to produce an output insensitive to the phase of the signal a special technique must be used.

In the discussion that follows it is assumed that the signal light leaving the interferometer has been collected and converted into a voltage $v(t)$ through a suitable detector and preamplifier. Description of these elements is postponed until the next chapter since they have no direct bearing on the material presented here. In terms of eqn. 4.13 the output signal is

$$v(t) = \frac{1}{4} C I_1 \{1 + V(\tau) \cos[\omega_0 \tau + 4\omega_s t - \pi]\} \quad (4.14)$$

where C is a constant that depends on the detector and preamplifier characteristics.

Synchronous detection

The synchronous detector used in this experiment was an Ithaco Dynatrac 3 lock-in amplifier (model 393). This amplifier provided a unique insensitivity to signal phase. The basic idea is simply to detect the output signal with two separate lock-in amplifiers whose

reference signals are 90° out of phase. The outputs of these amplifiers are then vector summed to provide the desired output. The Dynatrac 3 performs these functions in a single package.

The input to the Dynatrac 3 is AC coupled so that the signal supplied to the first stages is proportional to the AC part of eqn. 4.14

$$v_1(t) = \frac{1}{4} C I_1 V(\tau) \cos[\omega_o \tau + 4\omega_s t - \pi] . \quad (4.15)$$

This signal is then divided into two channels and each channel is multiplied by a reference signal,

$$v_{ref,s}(t) = \sin(4\omega_s t + \phi) \quad (4.16)$$

$$v_{ref,c}(t) = \cos(4\omega_s t + \phi) .$$

The outputs of the multipliers are then passed through low pass filters whose outputs are

$$v_c(\tau) = \frac{1}{8} C I_1 V(\tau) \cos(\omega_o \tau - \phi') \quad (4.17)$$

$$v_s(\tau) = \frac{1}{8} C I_1 V(\tau) \sin(\omega_o \tau - \phi') \quad (4.18)$$

where the following definition has been used: $\phi' = \phi + \pi$. Note that these outputs are no longer explicitly functions of time; they remain constant as long as none of the parameters change.

The final output is formed by vector summing the outputs of the low pass filters (eqns. 4.17 and 4.18) to give,

$$v_{vs}(\tau) = [v_c^2 + v_s^2]^{1/2} = \frac{1}{8} C I_1 V(\tau) . \quad (4.19)$$

Note that $v_{vs}(\tau)$ does not depend on ω_0 or τ except through the fringe visibility function $V(\tau)$, providing the desired result.

Finally, notice that $v_{vs}(\tau)$ is directly proportional to I_1 as well as $V(\tau)$. Consequently, changes in the total amount of scattered light I_1 would be indistinguishable from changes in $V(\tau)$. To remove this problem an independent measurement of I_1 is required. This measurement is easily made from the same raw signal $v(t)$ (eqn. 4.16) as described below.

Independent measurement of I_1

To obtain an independent measurement of I_1 the output of the preamplifier $v(t)$ is simply passed directly through a low pass filter. The output of the filter is then proportional to,

$$v_o = \frac{1}{4} C I_1 . \quad (4.20)$$

We now have the signals assumed in the development of Chapter 3. $S(\tau)$ and S_o are simply proportional to $v_{vs}(\tau)$ and v_o ,

$$\begin{aligned} S(\tau) &= C' I_1 V(\tau) \\ S_o &= C'' I_1 \end{aligned} \quad (4.21)$$

where C' and C'' include the constants of eqns. 3.21 and 3.22 and any other applicable amplifier gains. These two signals provide the data for determining temperature measurements through the use of eqn. 3.28.

In Chapter 3 it was shown that a fixed delay Michelson interferometer has the unique ability to efficiently use the available signal light for determining changes in spectral width of the scattered spectrum. In the next section it is shown that this efficiency is retained by the frequency shifted interferometer described in this chapter.

The Spectral Filter Picture Revisited

In Chapter 3 it was shown that a fixed delay Michelson interferometer could be regarded as a spectral filter with a sinusoidal bandpass (eqn. 3.34). This concept was found useful in understanding the performance of the interferometer in the signal noise limited case. This concept may also be extended to the frequency shifted interferometer described in this chapter. In this case the filter function is similar to that of eqn. 3.34 except that it "sweeps" continuously in frequency.

To obtain this result we must return to eqn. 4.11 and proceed in a slightly different way. Rewriting eqn. 4.11 we have

$$\langle E_h^* E_h \rangle = \frac{1}{4} \Gamma(0) + \text{Re } \Gamma(\tau) e^{i(4\omega_s t - \pi)} \quad (4.11)$$

where $\Gamma(\tau) = \langle E_o^*(t+\tau) E_o(t) \rangle$. Breaking the self coherence function into its real $\Gamma_r(\tau)$ and imaginary $\Gamma_i(\tau)$ parts eqn. 4.11 becomes

$$\begin{aligned} \langle E_h^* E_h \rangle &= \frac{1}{4} [\Gamma(0) + \Gamma_r(\tau) \cos(4\omega_s t - \pi) \\ &\quad - \Gamma_i(\tau) \sin(4\omega_s t - \pi)] . \end{aligned} \quad (4.22)$$

From eqn. 3.7 we know that $\Gamma_r(\tau)$ is equal to the Fourier transform of the spectral density function $G(v)$,

$$\Gamma_r(\tau) = \int_{-\infty}^{\infty} G(v) e^{i2\pi v \tau} dv . \quad (3.7)$$

Since $G(v)$ is an even function (see eqn. 3.9), we may express $\Gamma_r(\tau)$ in terms of the cosine transform,

$$\Gamma_r(\tau) = 2 \int_0^{\infty} G(v) \cos 2\pi v \tau dv . \quad (4.23)$$

Similarly, it is not difficult to show that the imaginary part of the self coherence function is simply

$$\Gamma_i(\tau) = -2 \int_0^{\infty} G(v) \sin 2\pi v \tau dv . \quad (4.24)$$

Using these results eqn. 4.22 becomes

$$\langle E_h^* E_h \rangle = \frac{1}{4} [\Gamma(0) + 2 \int_0^{\infty} G(v) \cos(2\pi v \tau - 4\omega_s t + \pi) dv] . \quad (4.25)$$

In terms of spectral irradiance we find

$$I(\tau, t) = \int_0^{\infty} I_v(v) \frac{1}{4} [1 + \cos(2\pi v \tau - 4\omega_s t + \pi)] dv \quad (4.26)$$

in analogy to eqn. 3.32.

So, for the case of the frequency shifted interferometer used in this experiment, the spectral filter function is

$$F(v, t) = \frac{1}{4}[1 + \cos(2\pi v\tau - 4\omega_s t + \pi)] \quad (4.27)$$

which is clearly similar to that of the simple fixed delay Michelson interferometer except that it sweeps continuously in frequency.

In order to understand the operation of the overall system described in this chapter it is necessary to pursue this analogy further and include some aspects of the signal processing system. For example, including the detector and preamplifier we may express $v(t)$ as follows:

$$v(t) = A \int_0^{\infty} I_v(v) \frac{1}{4}[1 + \cos(2\pi v\tau - 4\omega_s t + \pi)] dv. \quad (4.28)$$

After AC coupling the signal has the form

$$v_1(t) = A \int_0^{\infty} I_v(v) \frac{1}{4} \cos(2\pi v\tau - 4\omega_s t + \pi) dv, \quad (4.29)$$

and at the output of the low pass filters the outputs are,

$$v_c(\tau) = \frac{1}{8} A \int_0^{\infty} I_v(v) \cos(2\pi v\tau + \phi') dv \quad (4.30)$$

$$v_s(\tau) = \frac{1}{8} A \int_0^{\infty} I_v(v) \sin(2\pi v\tau + \phi') dv,$$

where again, $\phi' \equiv \phi + \pi$ and ϕ is the relative phase of the reference signal.

In analogy to eqn. 3.34 the filter functions in this case would be

$$F_c(v) = \frac{1}{2} \cos(2\pi v\tau + \phi') \quad (4.31)$$

$$F_s(v) = \frac{1}{2} \sin(2\pi v\tau + \phi'). \quad (4.32)$$

This definition loses some of the appeal of eqn. 3.34 since these spectral filters have a negative "transmittance" for some frequencies. However, the spectral filter analogy is still useful for understanding the relationship of the frequency shifted interferometer and synchronous detector to the simple fixed-delay interferometer of Chapter 3. The factor of 1/2 occurs in eqns. 4.31 and 4.32 because only the horizontally polarized output beam is used. Notice also that the filter may be scanned in frequency by varying the phase ϕ of the reference signal.

The final step is to relate the vector sum of the two components of eqn. 4.30 to the spectral filter picture. It can be shown that this vector sum output is effectively equivalent, in both signal and noise, to the output due to a single component (e.g., eqn. 4.31) where the reference signal phase ϕ has been adjusted to give maximum output.⁴⁵

In this case the vector sum output is

$$V_{vs}(\tau) = \frac{1}{8} A \int_0^{\infty} I_v(v) \cos(2\pi v\tau + \phi') dv \quad (4.33)$$

where, $\phi' = n2\pi - 2\pi v_o \tau$ and v_o is the center frequency of the spectrum $I_v(v)$. The condition on ϕ' forces the cosine function to a maximum at $v = v_o$. The result is as if the filter function of eqn. 4.31 continuously tracked the spectrum of scattered light. This condition is shown graphically in fig. 4.2.

This completes the investigation of the spectral filter properties of the frequency shifted interferometer and signal processor combination. It has been shown that this setup is very similar to the classical fixed delay Michelson interferometer except that the filter

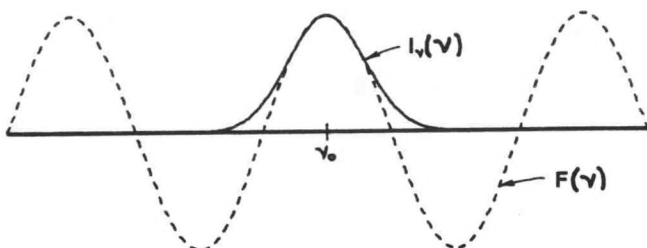


Fig. 4.3 The Relationship of the Spectrum $I_v(v)$ to the Generalized Filter Function $F_v(v)$ of the Interferometer/Signal Processor Combination.

effectively tracks the scattered spectrum and is insensitive to small changes in the interferometer's optical delay τ . To complete this chapter we next calculate the MDTC for the interferometer/processor combination.

Minimum Detectable Temperature Change (MDTC)

In this section we return to the concept of MDTC and apply it to the frequency shifted interferometer. To begin with, we will assume an ideal interferometer in order to be able to compare the results thus obtained with those of Chapter 3. We will then extend the calculation to include imperfections associated with the real interferometer in order to estimate the MDTC expected for actual experimental conditions.

As in previous cases we will assume that the total amount of scattered light I_1 remains constant and that aerosol scattering is negligible. We also assume, as before, that signal shot noise is the dominant source of noise and that the interferometer is "perfect." If only one component of the output beam is used then the power on the

detector is,

$$P(t) = A \frac{1}{4} I_1 [1 + V(\tau) \cos(\theta + 4\omega_s t)] \quad (4.34)$$

where $\theta = 2\pi v_o \tau - \pi$ (cf. eqn. 4.13) and A is the collected area of the output beam.

The signal processing system measures the RMS AC signal amplitude and responds to the RMS noise within a narrow bandpass Δf . Referring the MDTC calculation to the output of the detector we have,

$$\xi(t) = R P(t)$$

$$\xi_{\text{RMS}} = R \frac{A I_1}{4\sqrt{2}} [2 + V(\tau)^2]^{1/2} \quad (4.35)$$

$$\xi_{\text{AC, RMS}} = R \frac{A I_1}{4\sqrt{2}} V(\tau)$$

$$\xi_N = [2 e \xi_{\text{RMS}} \Delta f]^{1/2}$$

where R is the detector responsivity in amps/watt.

In this case MDTC is defined in terms of $\xi_{\text{AC, RMS}}$ since the signal processor's output is proportional to this quantity. That is,

$$\text{MDTC} \equiv \frac{\xi_N}{\partial \xi_{\text{AC, RMS}} / \partial T} \quad (4.36)$$

Using this definition, the preceding expressions, and eqn. 3.41 the following expression is obtained:

$$\text{MDTC} = \frac{1}{\pi b^2} \left[\frac{4e\Delta f}{R I_1} \right]^{1/2} \frac{2\sqrt{2}}{\tau^2} \frac{[2 + \exp^2(-\pi b^2 \tau^2 T)]^{1/4}}{\exp(-\pi b^2 \tau^2 T)} , \quad (4.37)$$

where as before $b^2 \equiv |\vec{K}|^2 K_B/2\pi M$. This expression may be compared with that for the classical fixed delay Michelson interferometer, eqn. 3.42. This comparison is shown graphically in fig. 4.4. In studying this comparison recall that we have made use of only half of the output of the frequency shifted interferometer. A lower MDTC would result if the signal processor made use of both output components.

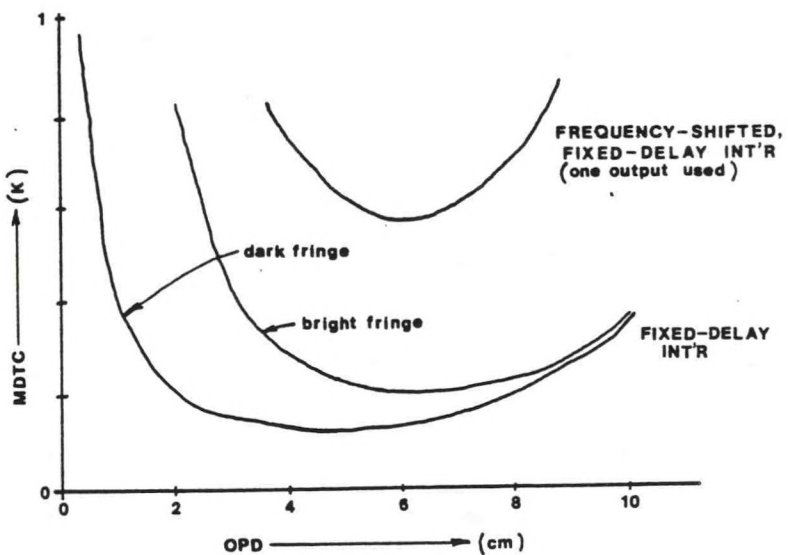


Fig. 4.4 MDTC vs. τ for the Frequency Shifted Michelson Interferometer and Classical Michelson Interferometer.

Parameters are: $\Delta f = 1$ Hz, $R = 0.027$ amp/watt, $I_1 = 5.7 \times 10^{-10}$ watt, $T = 300$ K, $\lambda = 514.5$ nm, backscatter.

Finally, we should extend eqn. 4.37 to include the imperfections of a non-ideal interferometer. In Chapter 3 it was shown that all of the imperfections simply reduce the interferometric efficiency η_I

and/or overall system efficiency η_0 . In terms of these quantities, the power on the detector becomes,

$$P(t) = A \frac{1}{4} I_1 \eta_0 [1 + \eta_I V(\tau) \cos(\theta + 4\omega_s t)] \quad (4.38)$$

in analogy to eqn. 4.34. It is not difficult to proceed with the analysis as before to obtain,

$$MDTC = \frac{1}{\pi b^2} \left[\frac{4e\Delta f}{RI_1 \eta_0} \right]^{1/2} \frac{2\sqrt{2} [2 + \eta_I \exp^2(-\pi b^2 \tau^2 T)]^{1/4}}{\tau^2 \eta_I \exp(-\pi b^2 \tau^2 T)}. \quad (4.39)$$

Using a hard target I have measured η_I experimentally to be about 0.68. The quantity η_0 could also be measured experimentally, although for the purposes here a guess will suffice. Figure 4.5 is a plot of eqn. 4.39 using values of 0.68 and 0.65 for η_I and η_0 respectively.

The graph of fig. 4.5 constitutes a calculation of the expected experimental noise performance of the interferometer described in this chapter and the next. Note that the predicted MDTC is below the original design goal of 1 K at the optimum value of τ . Throughout this development a value of $I_1 = 5.67 \times 10^{-10}$ watts has been used without explanation. In the next section this value is justified.

Expected Signal Level

In this section we estimate the irradiance level due to Rayleigh scattered light at the entrance to the interferometer. Here we will assume that all collected light is transferred to the interferometer

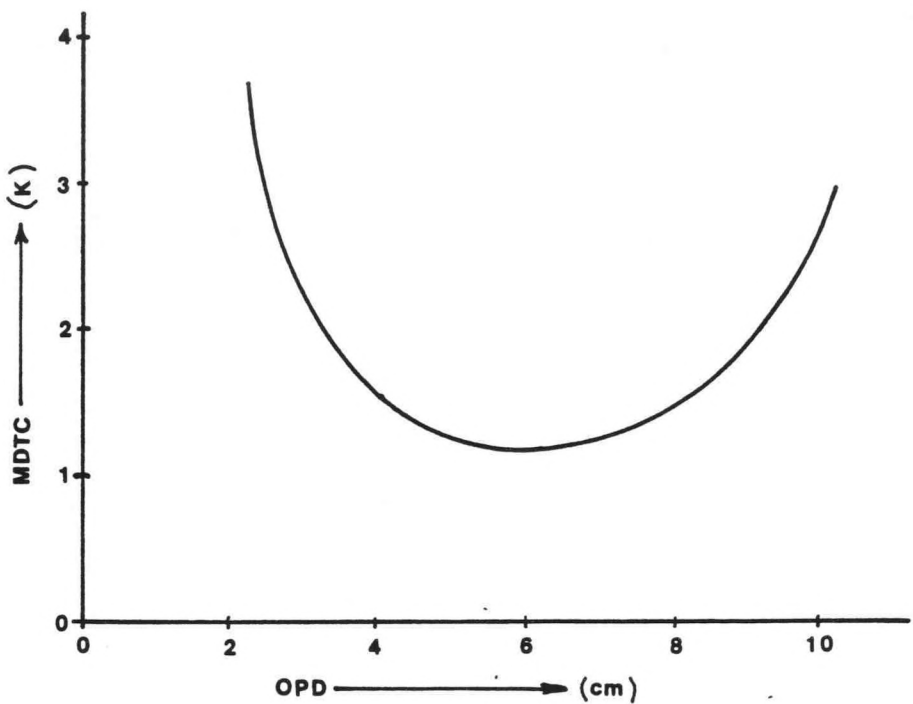


Fig. 4.5 MDTC vs. τ for the Frequency Shifted Michelson Interferometer Including the Effects of a Non-Ideal Interferometer.

Parameters are the same as for fig. 4.4 with $\eta_o = 0.6$ and $\eta_I = 0.68$.

without loss since actual losses have been accounted for by the overall optical efficiency factor η_o of eqn. 4.39. Aerosol scattering is neglected as before.

The geometry of the source and collecting lens are shown schematically in fig. 4.6. The source is effectively a line source lying along the optical axis of the lens. However, only the rays from a length ℓ pass through the field stop and on to the interferometer. With $f = 7.5''$, $D = 2.78''$, and the field stop diameter $a = 0.063''$, ℓ may be calculated using a simple paraxial analysis to yield $\ell \approx 1''$.

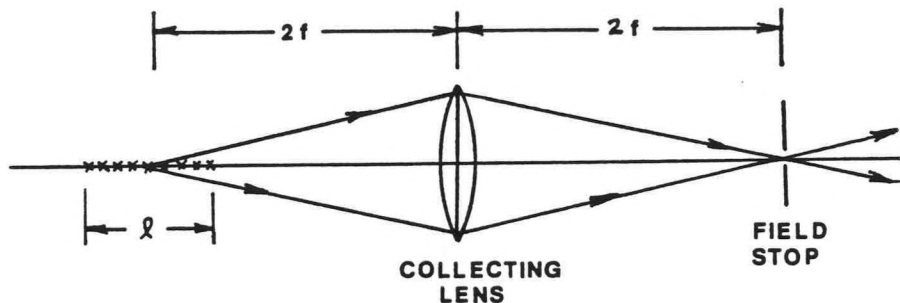


Fig. 4.6 Schematic Representation of Source and Collecting Lens Geometry.

Now using eqn. 2.2, the total collected power may be evaluated. Since the entire spectrum is collected, and assuming that the scattered irradiance is nearly constant over the collecting lens aperture, eqn. 2.2 becomes

$$P = I_o V \frac{d\Sigma}{d\Omega} \Omega \quad (4.40)$$

where I_o is the incident irradiance from the laser, V is the interaction volume, $d\Sigma/d\Omega$ is the differential Rayleigh volume scattering cross section, and Ω is the solid angle of collection. The product $I_o V$ may also be expressed as $P_o l$ where P_o is the power in the incident beam; in this case $P_o = 400$ mW. Equation 2.3 may be used to evaluate $d\Sigma/d\Omega$. With $\psi = 90^\circ$ (backscatter), $n = 1.000279$ (see for example Pendorf¹⁶), and $\rho_o = 2.092 \times 10^{25} \text{ m}^{-3}$ (evaluated using the ideal gas law for $P = 650$ mm Hg and $T = 300$ K) the result is $d\Sigma/d\Omega = 2.096 \times 10^{-6} \text{ m}^{-1} \text{ sr}^{-1}$. From the geometry of fig. 4.6, Ω may be estimated yielding $\Omega = 2.698 \times 10^{-2} \text{ sr}$. Using these values and eqn. 4.40 one obtains $P = 5.67 \times 10^{-10} \text{ watt}$. The irradiance in any plane may be estimated by simply dividing by the

beam area. However, in all cases power is the quantity of ultimate significance.

CHAPTER 5

EXPERIMENTAL OBJECTIVES, APARATUS, AND PROCEDURE

The basic objective of the experimental work reported here was to test the operation of a frequency shifted Michelson interferometer as a remote sensor of air temperature. The interferometer's noise performance was evaluated by experimentally measuring temperature changes in air and by experimentally determining the minimum detectable temperature change (MDTC). Theoretically, temperature changes are related to output signal changes through eqn. 3.28. Experimentally, this relationship was tested by simply inducing a known temperature change in the scattering air and observing the resulting signal change. Experimental determination of the MDTC was made by direct application of the definition (eqn. 3.35) to the same data. In the case of MDTC, only general agreement with the theoretical estimate of fig. 4.5 was expected since many of the parameters used in that estimate were approximations.

The experimental setup used in this investigation can be broadly divided into two parts: (1) the scattering chamber and its related systems, providing the source of scattered radiation under known conditions and (2) the interferometer and its related parts, providing the tool for analyzing the scattered light. The basic experimental layout is shown schematically in fig. 5.1. The remainder of this chapter is devoted to describing the experimental setup and procedures used in obtaining data.

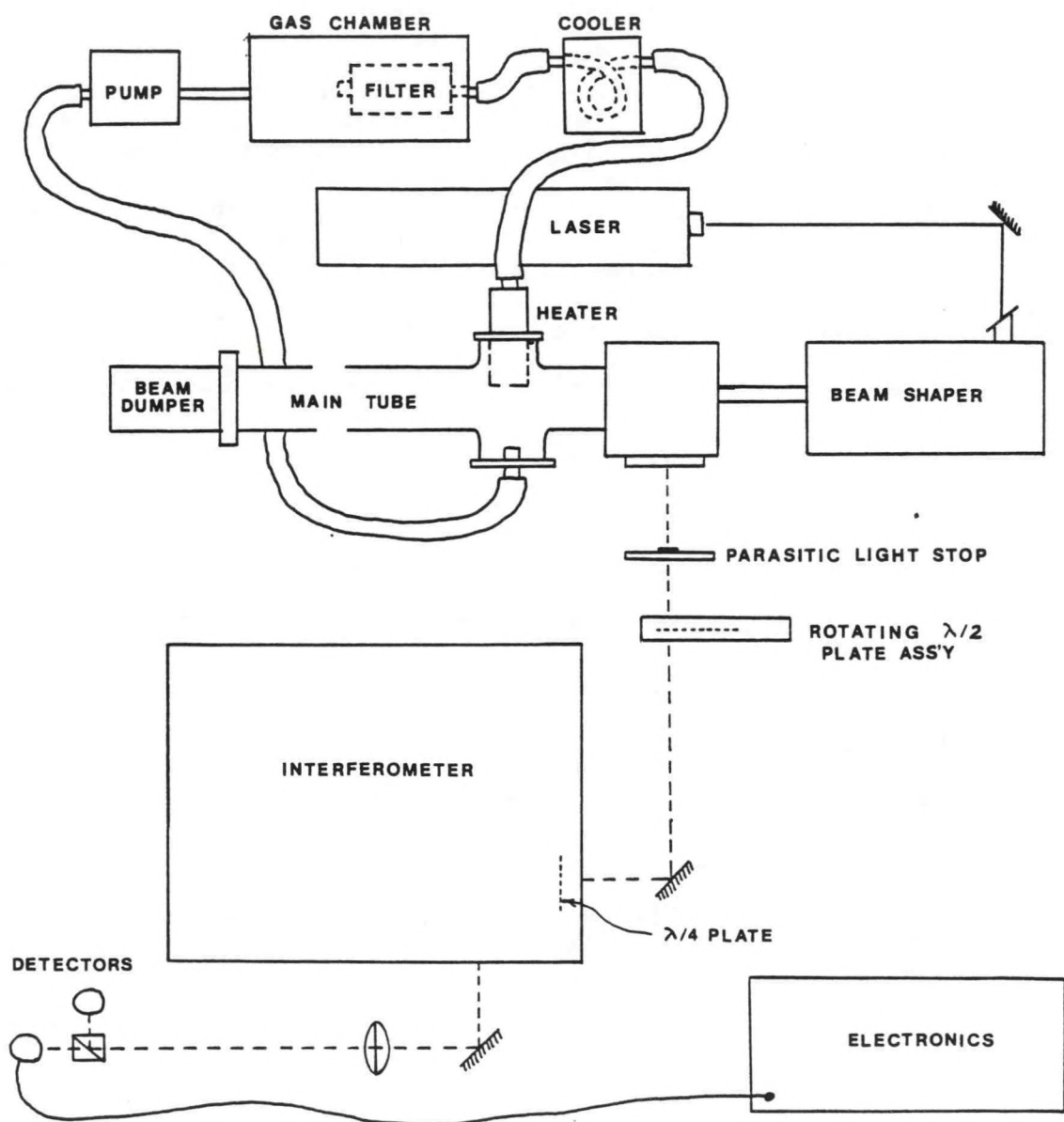


Fig. 5.1 Schematic Layout of the Experimental Apparatus.

Scattering Chamber and Related Systems

The scattering chamber and its related systems include the laser, a beam shaper, the scattering chamber itself, parasitic light suppressors, and the gas circulation and temperature control system. These components were designed to produce a stable source of Rayleigh scattered light under controlled conditions. The design differs from that of many other scattering chambers in that the temperature of the gas in the scattering volume had to be rapidly variable ($\sim 3^\circ\text{C}/\text{min}$).

The Laser

The light source chosen for this experiment was a Lexel model 95-4 argon ion laser with internal etalon and compensated Invar resonator structure. Throughout the experiment the laser was operated on the 514.5 nm line at power levels of about 400 mW TEM_{00} . The internal etalon assured operation on a single axial mode. The output power of the laser was stabilized by a built-in light regulator. Integrated noise fluctuations over the frequency range 10 Hz - 200 kHz were measured to be $< 0.2\%$ of the DC component. Long term stability was also excellent, amounting to a less than 0.5% variation over 1 h periods.

The apparent output linewidth of an argon laser is extremely narrow and is limited mainly by frequency jitter caused by mechanical vibrations of the resonator structure. This frequency jitter was measured for the laser used in this investigation and found to be limited to excursions of less than about ± 1 MHz.

Despite the compensated resonator structure of the laser, the absolute frequency of the output drifted within the passband of the

internal etalon. Even after considerable warmup periods a drift of 5 MHz/min was not uncommon. This frequency instability was the major reason for developing the frequency shifted interferometer which provided immunity to frequency drift in the scattered spectrum (see Chapter 4).

Beam Shaping

As shown in fig. 5.2, after leaving the laser the beam entered the beam shaping chamber via a Brewster window. The three main components there were the usual focusing lens, pinhole spatial filter, and refocusing lens. The refocusing lens focused the beam to a waist within the main scattering chamber tube. An iris following the refocusing lens was used to remove some of the forward scattered halo due to dust and imperfections on the refocusing lens.

After leaving the beam shaping chamber the beam traveled through a hole in the turning mirror and then on into the scattering chamber's main tube. Approximately 36 cm beyond the turning mirror the beam was focused to a waist. It was light scattered from this waist that formed the signal supplied to the interferometer. Most of the beam continued on from the waist down the main tube about 1.5 m to the beam dumper where it was extinguished.

Light backscattered from the waist within a 10.9° cone angle ($f/5.2$) was reflected from the turning mirror and gathered by the main objective lens. This light then passed out of the scattering chamber to be focused at the field stop on the rotating wave plate frequency shifter.

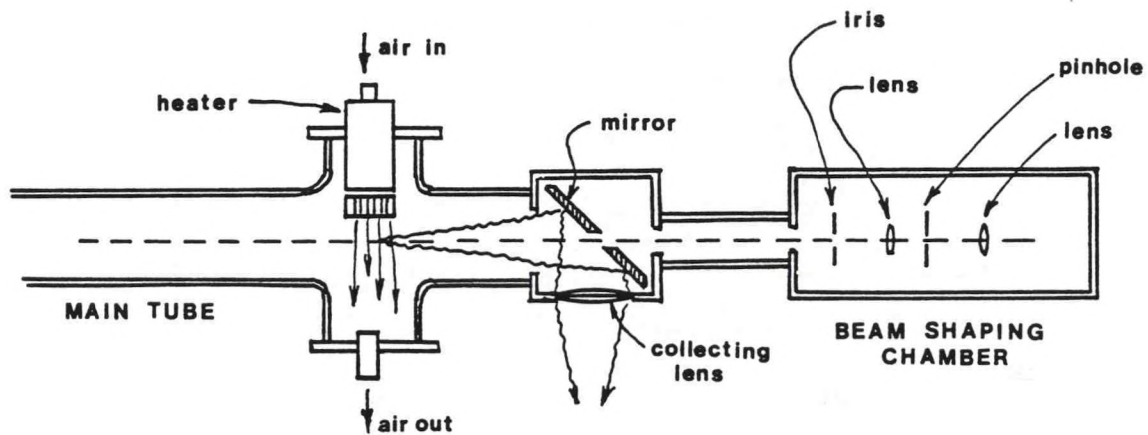


Fig. 5.2 Side Drawing of the Scattering Chamber.

The beam shaper, turning mirror, and main tube are shown.

Parasitic Light Suppressors

The main problem in designing a scattering chamber such as the one described here, is getting rid of unwanted (parasitic) scattered light. The amount of light gathered by the collecting lens was about nine orders of magnitude less than the light contained in the main beam. Clearly, any surface struck by the main beam would produce a source of scattered light much brighter than the Rayleigh scatter to be observed. The scattering chamber employed four methods of preventing the unwanted scattered light from reaching the detector.

The first was simply the use of black walls within the chamber. All surfaces were black, anodized aluminum except the main tube and the tube around the beam dumper. These tubes were glass painted black on the outside. Most of the light striking the walls of the glass tube was either absorbed or specularly reflected. Specular reflection was

preferable to diffuse reflection because the light was then confined to a small cone angle that could be effectively baffled.

The beam dumper assembly (fig. 5.3) formed the primary defense against unwanted scattered light. Any forward scattered light (from the refocusing lens) surrounding the main beam in a halo was stripped off by a cone at the entrance to the beam dumper chamber. This light then underwent multiple reflections between the surface of the cone and the wall of the tube surrounding it, thereby becoming extinguished. In effect, the cone and the tube surrounding it formed a type of Wood's horn attenuator.⁴⁶

The main beam proceeded through the hole bored along the axis of the cone and on into the beam dumper chamber. There it encountered a polished silicon flat at Brewster's angle. At the laser wavelength (514.5 nm) silicon has a high extinction coefficient and a Brewster's angle of about 76.5°. Since the beam was almost entirely vertically polarized, most of it was coupled into the first silicon flat and absorbed. The second silicon flat further attenuated any remaining vertically polarized light. Using this technique very low scatter may be achieved, limited

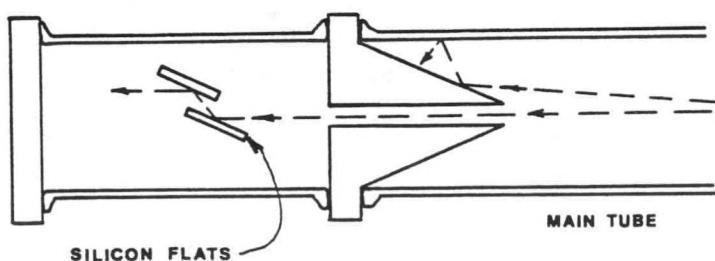


Fig. 5.3 Beam Dumper Assembly.

only by dust and microirregularities, primarily on the surface of the first silicon flat. Total scatter from such an arrangement can be as low as 1-10 ppm compared with about 1% for typical carbon black surfaces.⁴⁷

Inevitably, some light was scattered back into the scattering chamber. There were several possible light paths from the silicon surface back to the collecting lens. First there was the direct path which could not be baffled within the chamber. However, light undergoing one or more reflections from the inner wall of the main tube was effectively blocked by a single baffle located near the center of the main tube.

In order to baffle the direct scattered light, use was made of the different object distances of the observed Rayleigh scatter volume and the silicon flat from the collecting lens. The distance from the collecting lens to the Rayleigh scatter volume was about 44 cm; the distance to the silicon flat was about 2 m. The focal length of the collecting lens was 19 cm and consequently, the scattered light from the silicon flat was brought to a focus 21 cm beyond the lens whereas light from the Rayleigh scatter volume was focused 33 cm from it. A glass plate, with an opaque spot at its center, placed at the 21 cm focus effectively blocked the unwanted light. At the same time almost all of the signal light passed around the opaque spot and on to the 33 cm focus where it entered the rotating waveplate frequency shifter.

The final line of defense against parasitic scattered light was a set of apertures in the interferometer's optical train. The main collecting lens formed the aperture stop of the system and an iris at the 33 cm focus formed the field stop. These defined the $A\Omega$ product

of the optical system. For scattered light purposes however, the detector also had an aperture providing another field stop. This redundancy of field stops helped prevent unwanted light from reaching the detector.

Gas Circulation and Temperature Control

An accurate knowledge of the characteristics of the gas occupying the scattering volume within the scattering chamber was essential to the experiment. Important parameters were temperature, pressure, and aerosol content. To simplify the experiment the aerosol content of the gas was reduced to a negligible level. Pressure had to be known and constant whereas temperature had to be rapidly variable in order to test the response of the interferometer.

Temperature control was provided by continuously circulating air through the interaction volume within the scattering chamber, as shown in fig. 5.4. After leaving the scattering chamber the air was drawn through a diaphragm pump at a rate of 30 l/min (1.1 cfm). From there it entered a large chamber where pressure fluctuations due to the recipro-

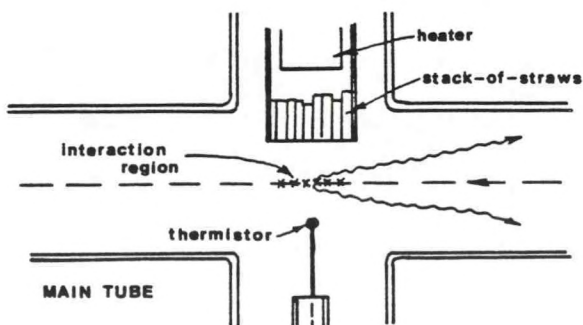


Fig. 5.4 Interaction Region.

cating diaphram pump were smoothed out. In order to leave the chamber, the air had to exit through a series of two filters after which it passed through cooling coils in an ice water bath. From there it returned to the scattering chamber. Just before reaching the scattering volume the air passed through a 400 watt electrical heating element followed by a stack-of-straws intended to produce laminar flow through the interaction volume.

The temperature of the air was measured with a thermistor suspended in the center of the flow just downstream from the scattering volume. The thermistor, used in conjunction with a Hewlett-Packard model 3467A logging multimeter, was intended to provide an accurate indication of the air temperature within the scattering volume. However, this turned out to be more complicated than was origionally anticipated. More will be said about this later.

The power level supplied to the heating element was manually adjusted. By watching the indicated temperature and adjusting the power level accordingly, I found that I could rapidly adjust the air temperature and maintain it to within $\pm 0.2^{\circ}\text{C}$ of a desired level.

The pressure within the scattering chamber was always set to the atmospheric pressure at the time the chamber was filled. The absolute pressure was measured in the next room with a Wallace and Tiernan model FA145 gauge which yielded measurements with an uncertainty of $\pm 0.5 \text{ mm Hg}$. Typically the pressures were about 605 mm Hg.

In this experiment I was able to reduce aerosol scattering to a negligible level by using the two series filters mentioned above. The

filters were designed to remove particles 0.3 μm or larger in diameter with a 99.99% efficiency. Residual aerosol scattering was experimentally confirmed to be negligible.

Other ports into the scattering chamber were provided for connection to a vacuum pump and to a helium tank. The vacuum pump was capable of rapidly pumping the entire system down to an ultimate pressure of about 1.2 mm Hg. Lower pressures were unattainable due to numerous small leaks. The system could then be flushed and backfilled with helium periodically to check the signal level due to parasitic scattered light.

The Interferometer and its Related Systems

The interferometer and its related systems included the rotating waveplate frequency shifter, the interferometer, detector, and signal processing electronics.

Rotating Waveplate Frequency Shifter

As discussed in Chapter 4 the polarization frequency shifter consisted optically of a rotating half-wave plate followed by a stationary quarter-wave plate. Physically the rotating half-wave plate was made of a 2" diameter wave plate glued on the end of a shaft, mounted in a housing with a small synchronous AC motor. The wave plate shaft and motor were connected by a small rubber belt which drove the wave plate at about 3000 RPM. A reference signal was derived from the rotating wave plate by way of an infrared emitter and detector viewing alternately black and white segments painted on the edge of the wave plate.

After leaving the rotating half-wave plate assembly, the beam was reflected from a 45° dielectric mirror and then entered the interferometer

enclosure via a thin glass window. The stationary quarter-wave plate was located just inside the enclosure. This wave plate was mounted so as to permit tilt tuning to obtain exactly quarter-wave retardation. Both wave plates were nominal 2" diameter, zero order mica elements, cemented between glass plates for rigidity.

The Interferometer

The interferometer was basically a classical Michelson interferometer with 2" diameter nominal aperture. A major factor in the design was the need for flexibility. Since the interferometer itself was the primary research tool of this investigation, the ability to easily make changes was important. Consequently, no effort was made to make it compact.

All components in the interferometer were mounted on a granite slab for mechanical and thermal stability. Two important sources of noise were mechanical room vibrations and air currents within the interferometer. Vibration isolation was provided by supporting the entire experimental layout (except electronics) on a table with each leg "floating" on an inner tube. Air currents within the interferometer were eliminated by enclosing it within a styrofoam box with windows providing access for the signal.

Optical components included the beam splitter, a compensating plate, a high quality quarter-wave plate, and the mirrors as shown in fig. 5.6. The beam splitter was a dielectric coated, quartz plate with 30' of wedge. The compensation plate was identical except that an

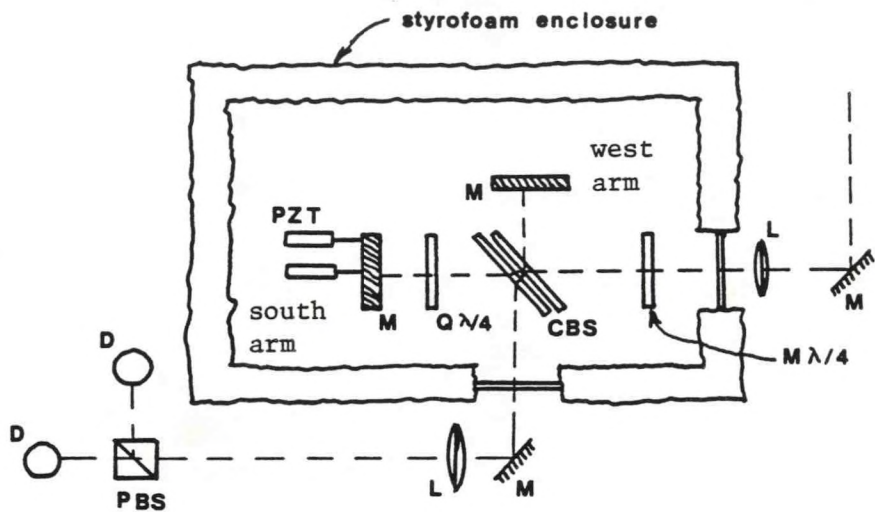


Fig. 5.5 The Interferometer and Detector Layout.

(M = mirror, L = lens, $M \lambda/4$ = mica $\lambda/4$ plate, CBS = compensated beamsplitter, $Q \lambda/4$ = quartz $\lambda/4$ plate, PZT = piezo electric mirror tilters, PBS = polarization beamsplitter, D = detector).

AR coating was applied to both sides. The quarter-wave plate was a multiple-order, crystalline-quartz plate 2" in diameter. The mirrors were flat, aluminized surfaces on quartz substrates.

In any interferometer the quality of the optics is of primary importance. Efficiency is determined in a large part by the relative wavefront distortion between interfering beams. However, in a cost versus performance comparison there is a point of diminishing returns. For this interferometer I chose $\lambda/20$ mirrors and all other components were specified at $\lambda/10$ maximum peak-to-valley wavefront error in transmission. The experimentally observed fringe pattern indicated an over-

all system wavefront error of about $\lambda/4$ resulting and a measured interferometric efficiency of about 0.68.

As in any Michelson interferometer, mirror alignment is also critical. For example, approximately 6.3 microradians of mirror tilt (1 wave) would cause a 10% loss of signal modulation. Even using high quality mirror holders, manual adjustment of critical mirror alignment is impossible. Consequently, I equipped one of the mirror holders with a PZT transducer to provide fine adjustment of mirror tilt for each axis. Typically, coarse adjustment of the interferometer was done manually after which the interferometer was sealed. Fine adjustment was then done electronically by varying the voltage supplied to the PZTs.

Although the PZTs solved the problem of fine adjustment, they created another problem. Slow drift in the output voltage of the PZT controller and drift in the mechanical response of the PZT transducers caused an overall drift in the alignment of the interferometer which resulted in signal drift. This signal drift was one of the limiting factors of the experiment.

The OPD of the interferometer could be varied by sliding one of the mirror mounts along parallel rails which supported it. Although the mirror support and rails were carefully constructed, fine adjustment of the interferometer was lost when changing from one OPD to another requiring realignment at each new setting. The position of the mirror was determined by a simple pointer and scale arrangement with an uncertainty of about ± 0.4 mm (1/64 inch).

Detector

As discussed in the last chapter, the output of the interferometer consisted of two superimposed signal channels: One vertically polarized, the other horizontally polarized. Since the information contained in these channels was identical, I used only one channel for simplicity.

At the output of the interferometer a lens intercepted the output beam and focused it onto the detector. Just before the detector a polarization beamsplitter was used to separate the signal channels. Actually, a detector was placed at the focus of both signal channels although only one of them was used except for occasional checks.

The detector used was an RCA 1P28A photomultiplier. This detector was well suited to the wavelength of interest and provided excellent responsivity and very low noise. Furthermore, its inherent low noise and high gain simplified subsequent signal processing.

Signal Processing Electronics

The signal processing electronics consisted of simply two operational amplifiers and a vector sum lock in amplifier as shown in fig. 5.6. The signal current leaving the photomultiplier was first converted into a voltage by an op-amp connected in the current-to-voltage configuration. The output of this op amp went directly to the lock in amplifier and also to the other op-amp which was connected as an integrator. For each data point, the output of the lock-in amplifier $S(\tau, T)$ and the output of the integrator $S_o(T)$ were recorded by the H-P model 3467A logging multimeter along with the time and air temperature.

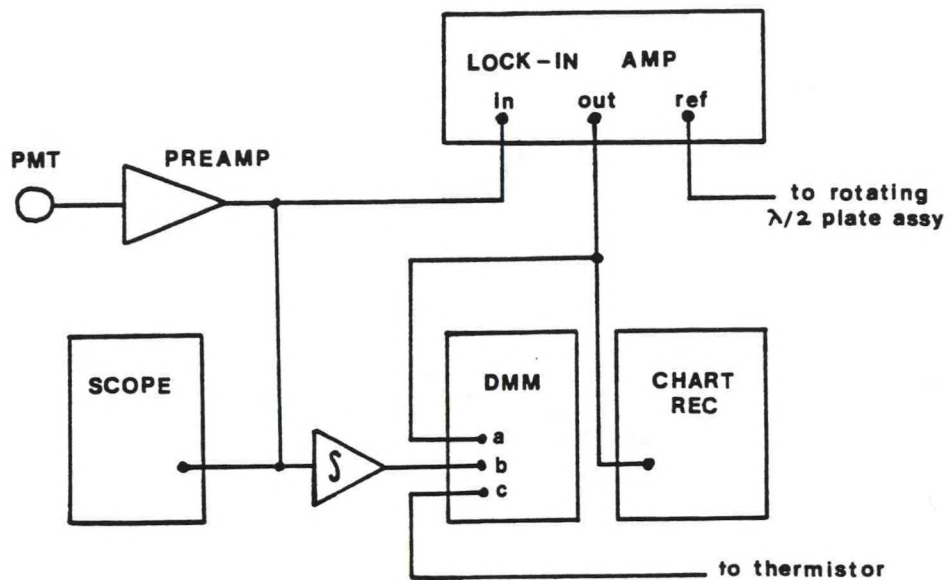


Fig. 5.6 Detector and Signal Processing Electronics.

The dominant source of noise in the experiment was signal shot noise. This was easily checked from time to time by blocking the signal beam and observing the output of the current-to-voltage converter. In each case the observed noise level dropped by about an order of magnitude when the signal beam was blocked.

Procedures

The basic goal of the experimental work reported here was to verify the operation of the fixed delay Michelson interferometer as a remote sensor of air temperature. Conceptually, this could have been accomplished by simply heating the air in the scattering volume to several known temperatures, recording the interferometer output signals $S(\tau, T)$ and $S_0(T)$, and then comparing the results with eqn. 3.27. While this describes the basic procedure used, various experimental details

complicated the situation. Important factors were optical alignment, signal drift, and parasitic scattered light. All of the procedures described in this section, except the thermistor calibration, were repeated for several different interferometer OPDs.

Warm up

Before each data taking session all of the equipment to be used was warmed up for a period of at least one hour. The exception to this was the PZT voltage driver which was left on continuously to minimize drift during the experiment. Also during this period the scattering chamber was vented to atmospheric pressure and then resealed after which the gas circulating pump was run to clean aerosols out of the system. The absolute air pressure in the system was then inferred by measuring the absolute atmospheric pressure in the next room.

Alignment

The alignment of the interferometer and waveplates were critical. Misalignment of the interferometer lead to a reduced AC signal output; misalignment of the waveplates lead to an AC signal component that was independent of the effective fringe visibility function $\eta_I V(\tau)$. In order to minimize these effects the following alignment procedure was performed at the beginning of each data taking session.

First, the interferometer's mirrors were adjusted to obtain the desired OPD. Then, with the laser running at low power, a hard target was lowered in the scattering chamber at the focus of the collecting lens. The interferometer's mirror alignment was then optimized using light scattered from this target.

Next, the waveplates were aligned, also using the light scattered from the hard target. The mica $\lambda/4$ plate (see fig. 5.5) was adjusted by blocking the south arm of the interferometer and tuning the waveplate to obtain a minimum AC signal at the lock-in amplifier (ideally no AC signal should be present since interference was prevented by blocking one arm of the interferometer). The quartz $\lambda/4$ plate was then likewise adjusted by tuning it to obtain minimum AC signal with the west arm blocked. The alignment was then checked by inserting an aberrator plate into one arm of the interferometer and again observing the residual AC signal. In all cases it was possible to obtain a residual AC signal which was <2% of the unblocked AC signal.

Finally, the hard target was removed from the beam, the laser power was turned up, and the signal due to Rayleigh scattering was observed. Again the mirror alignment was checked and reoptimized using this signal. Also the aberrator plate was again inserted into one arm of the interferometer to check the level of the residual AC signal and, if necessary, the tilt of the quartz $\lambda/4$ plate was reoptimized.

Temperature Data

Before taking data at different temperature levels, the interferometer was allowed to run for a period of about 10 minutes to insure that the system was stabilized. Temperature data was then obtained by simply recording several data points at each of various temperature levels within the range 290 K to 310 K. For each data group at least one of the temperatures was repeated during the test in order to provide a baseline for removing drift from the data. The time interval

which these measurements could be made was restricted to about five minutes due to this signal drift.

Each data point consisted of recording the time, temperature of the thermistor sensor, the AC signal $S(\tau, T)$, and the average signal $S_o(T)$. The values of each of these were printed on a paper tape by the HP3467A logging multimeter (see fig. 5.6). Additionally, a chart recorder provided a continuous record of the AC signal $S(\tau, T)$ versus time with tic marks to indicate when each data point was taken.

System Checks

Three system checks were performed periodically to monitor the operation of the interferometer, waveplates, signal processing system and the level of parasitic scattered light. The first system check, which has already been mentioned, was intended to check the alignment of the waveplates. It consisted of inserting an aberrating plate into one arm of the interferometer and measuring the residual AC signal level. The aberrating plate effectively destroyed the interference between the beams from the two arms of the interferometer and consequently, any residual AC signal was due to misalignment of the waveplates.

The second system check consisted of running the scattering chamber at constant temperature but alternately installing and then removing a thin, uncoated glass plate from the scattered light beam path (see fig. 5.1). The glass plate simply reduced the amount of light entering the interferometer. Data was recorded both with the plate installed and removed over a couple of cycles. The data obtained from this test was then processed identically to data obtained by

varying the temperature of the scattering air. Ideally, the processed data should indicate that there was no temperature change. Temperature changes actually indicated gave a measure of the overall performance of the system including the data processing.

At the end of each data taking session the level of parasitic scattered light was checked. To perform this test all equipment was left running while the scattering chamber was flushed with helium and pumped down to about 1.4 mm Hg. Lower pressures were unobtainable due to various small leaks. Then the chamber was backfilled with helium at atmospheric pressure. Rayleigh scattering from helium amounts to only about 1.4% of that from air⁶⁴ and consequently almost all of the signal observed with helium was due to parasitic scattered light and DC amplifier offsets. This data was then used to calculate corrections to the signals recorded due to Rayleigh scattering in air as described in the next chapter.

Calibration of the Thermistor Sensor

The temperature of the gas in the scattering volume was inferred by measuring its temperature slightly downstream with a small thermistor sensor as shown in fig. 5.4. Unfortunately this arrangement in itself was not adequate to determine the average temperature throughout the interaction region. By probing the interaction region with another thermistor it was discovered that the temperature along the laser beam path varied, being warmest at the center of the gas flow. In order to obtain an average temperature, a thermistor was placed inside a small

diameter, thin wall aluminum tube. The length of the tube was cut to correspond to the length of the laser beam observed by the interferometer ($\sim 1''$). This tube and thermistor assembly was then placed in the interaction region of the gas flow. The fixed, downstream thermistor was then calibrated against the temperature indicated by the tube assembly over the temperature range of interest.

Although this calibration procedure provided some indication of the average temperature in the interaction volume, the accuracy of the calibration was difficult to judge. The presence of the aluminum tube perturbed the flow of gas in its vicinity possibly causing some mixing with cooler gas at the outer edge of the flow. Since no other independent measurement was available, a relatively large uncertainty ($\pm 2^\circ\text{C}$ at 40°C) was assumed and is reflected in the results shown in the next chapter.

CHAPTER 6

EXPERIMENTAL RESULTS

In this chapter the results of the experimental work are presented. It is shown that the data generally verifies the theoretical developments of previous chapters in that: (1) the minimum detectable temperature change (MDTC) reaches a minimum value at an optical delay of about 6 cm and (2) eqn. 3.28 correctly relates the output signals of the interferometer to the temperature of the air in the scattering volume. The uncertainties in the measurements however are somewhat larger than originally anticipated, owing principally to signal drift, non-interferometric AC signal components, and the gas flow characteristics near the scattering volume in the scattering chamber. This chapter begins with a discussion of these sources of uncertainty. The question of the presence of aerosol scattering is then addressed, followed by an explanation of the data processing techniques. Finally, the MDTC and temperature measurement results are presented and discussed.

Factors Contributing to Experimental Uncertainty

Ideally, the only factor contributing to the measurement uncertainty in the experiment described here would be signal shot noise. Although generally the experiment was signal shot noise limited, several other factors also contributed to error. They were: (1) signal drift, (2) non-interferometric AC signal components, (3) gas flow characteristics near the scattering volume, and (4) uncertainty in the thermistor

temperature sensor calibration. None of these factors represents a fundamental limitation; indeed, a more careful design of the interferometer and scattering chamber could reduce all of these factors to a negligible level.

Signal Drift

Both the AC output signal $S(\tau, T)$ and the average signal $S_o(T)$ drifted as functions of time, even when the scattering gas was held at a constant temperature. In the case of the AC signal $S(\tau, T)$, the drift was often as much as 1%/minute which would be equal to an apparent change in gas temperature of about 1.7 K/minute (OPD = 5 cm, $T = 300$ K). The drift in the average signal $S_o(T)$ was generally less.

These drifts were caused by two effects. Most serious was a slow change in the mirror alignment of the interferometer caused by variations in the mechanical response of the PZT devices on one of the mirrors. The other source of signal drift was apparently a slight mechanical movement of the scattering chamber or laser beam relative to the system field stop. This lead to small variations in the light passing through the field stop which was reflected as variations in the output signals.

Generally, the signal drift appeared to be linear over periods of ten minutes or less. This fact was exploited in order to remove the drift effects from the data by repeating one temperature at the beginning and end of each experiment to provide a baseline against which other temperatures were compared. In spite of this technique some residual

error due to nonlinearity in the drift was unavoidable and difficult to estimate. However, after examining the data from many experiments I have estimated this error contribution to be on the order of 0.5 K or less for OPDs around 6 cm.

Non-Interferometric AC Signal Contributions

As described in the last chapter, slight imperfections or misalignment of the waveplates in the interferometer lead to an AC signal component that was independent of the interference between the two beams of the interferometer. By careful alignment this contribution could be reduced to a few percent of the main AC signal $S(\tau, T)$ at OPDS of about 6 cm or less. However, experimentally it was observed that the phase of the non-interferometric AC signal drifted relative to the main AC signal and therefore could not be simply subtracted from the data as an offset. In order to make an estimate of this contribution to the AC signal, half of its magnitude was subtracted as an offset and this amount was also taken as the uncertainty in the offset.

Possible Presence of Aerosol Scattering

In the experimental work reported here the attempt was made to reduce aerosol scattering to a negligible level by filtering the air that was passed through the scattering volume. The success of this effort was tested experimentally by looking for an interferometric signal contribution at a long optical delay (OPD ~ 20 cm). From eqns. 3.19 and 3.20 it can be seen that at long optical delays modulation in the interferogram could be due only to the presence of aerosol scattering.

Experimentally, it was found that to within the noise uncertainty, no interferometric AC signal existed at an OPD of 20 cm. From this observation it was concluded that aerosol scattering accounts for <1% of the AC signal $S(\tau, T)$ at OPDs of primary interest. This possible contribution was so small that it was generally ignored in the data processing.

Gas Flow Characteristics and Temperature Probe Calibration

The need to be able to rapidly change the temperature of the air in the interaction volume lead to the design of the scattering chamber cross flow arrangement shown in fig. 5.4. While this arrangement generally worked well, some problems were present. For example, the nearness of the heater assembly to the interaction volume resulted in temperature non-uniformity across the flow as described in the last chapter. Also, it seems reasonable to assume at flow temperatures far removed from ambient, some of the cooler air outside the flow probably mixed with the warmer air within the flow. This effect was impossible to measure accurately by the calibration technique described in the last chapter since the presence of the calibration sensor within the flow perturbed the system. The net result was that the temperature within the interaction volume was not as well known as originally hoped and the uncertainty increased as the temperature within the flow became much warmer than the ambient temperature outside the flow. In the data presented later in this chapter the uncertainty in the measured temperature is taken to be $\pm 2^\circ\text{K}$ at 310 K and decreases to ± 0.5 K near ambient (298 K).

Data Processing

As mentioned in the last chapter the data obtained for the experiment described here consisted of several data points collected at each of several different air temperatures. At least one temperature was repeated at the end of each data collection period to provide a baseline for removing drift effects. Each data point consisted of recording the time, thermistor temperature, average signal $S_o(T)$, and AC signal $S(\tau, T)$. Additionally, the non-interferometric AC signal contribution and signals due to parasitic scattered light and amplifier offsets were periodically measured. All of this data was later processed to remove the signal offsets and drift as described in the following paragraphs.

Calculating and Removing Offsets

Signal offsets were determined from the two system checks described in the last chapter. In one test an aberrating plate was placed in one arm of the interferometer thereby destroying the interference between the two arms. The residual AC signal provided an estimate of the non-interferometric AC signal component present. Half of this residual AC signal was subtracted as an offset from the AC signals $S(\tau, T)$ recorded during the experiment. Typically, this offset amounted to a few percent.

In another test, the level of parasitic scattered light was determined by filling the scattering chamber with helium and recording the signal outputs. The AC signal obtained in this way was subtracted directly from the AC signals $S(\tau, T)$ recorded during the experiment. The

average signal obtained with the helium fill was similarly subtracted from the average signal data $S_o(T)$ although it was first corrected by reducing it by the expected signal level (helium scatters about 1.4% as much as air³⁰). This correction was not necessary for the AC signal offset since the fringe visibility function for helium is essentially zero for all OPDs of interest. The AC signal offsets obtained in this way were typically about 3%. The average signal offsets were larger, owing to DC amplifier offsets, and were typically about 16%.

Removing Drift from the Data

Since data was obtained for one temperature level both at the beginning and end of each data collection period this data provided a baseline for removing drift. This baseline temperature was also taken to be the calibration temperature of eqn. 3.28. Signals obtained at other temperatures were then referenced to interpolated signals derived from the baseline signals. In this way linear drift was removed from the data. These concepts are illustrated graphically in fig. 6.1.

Calculating MDTC

The minimum detectable temperature change (MDTC) was calculated for several optical delays by simply applying the definition (eqn. 3.35) of MDTC to the corrected signals obtained at each delay. In this case, the output of the interferometer, denoted ξ in eqn. 3.35, was taken as the ratio of the corrected signals, $\xi = S(\tau, T)/S_o(T)$. The noise in the output ξ_N was taken to be the standard deviation of the output about its mean and the derivative $\partial\xi/\partial T$ was approximated as $\Delta\xi/\Delta T$

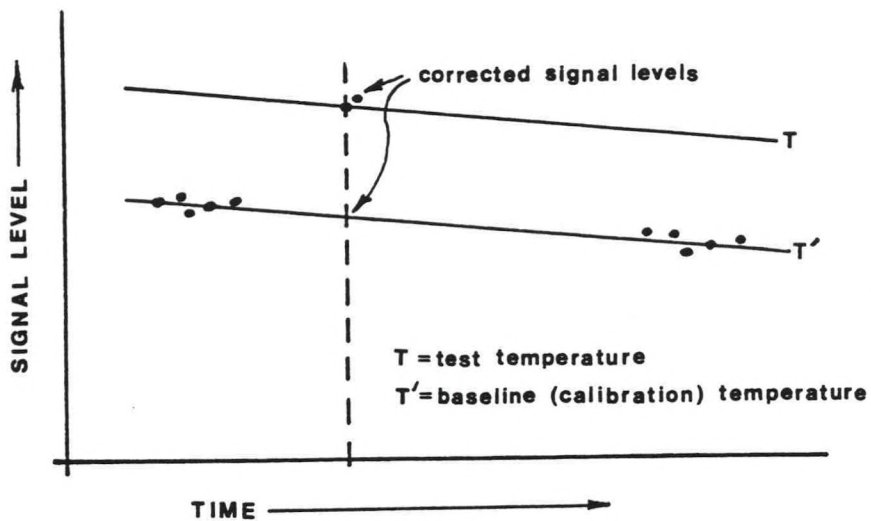


Fig. 6.1 Graphical Illustration of the Technique Used for Removing Signal Drift from the Temperature Data.

where ΔT was the temperature change measured by the thermistor probe.

Calculating Temperature and its Uncertainty

The calculated temperature T_c based on the corrected interferometer output signals $S(\tau, T)$, $S(\tau, T')$, $S_o(T)$, $S_o(T')$, and the calibration temperature T' was calculated by straightforward application of eqn. 3.28. The value of the constant b^2 in eqn. 3.28 was taken to be $2.72544 \times 10^{-16} \text{ s}^{-2} \text{ K}^{-1}$ which corresponds to a backscatter geometry with $\lambda_o = 514.5 \text{ nm}$ and an average molecular weight of the scattering gas of 28.964. The interferometer optical delay time τ was calculated from the simple relationship: $\tau = 2x/c$ where c is the speed of light and x is the relative mirror displacement from the $\text{OPD} = 0$ condition.

The uncertainty in the calculated temperature T_c was obtained from eqn. 3.30 where again S_a and S_{oa} were set equal to the total signal offsets and ΔS_a and ΔS_{oa} were set equal to the uncertainties in those offsets. As suggested by the example of table 3.1, the uncertainty in the corrected signals $S(\tau, T)$ and $S_o(T)$ accounted for most of the uncertainty in T_c .

Results and Discussion

Calculated MDTC versus optical delay is shown in fig. 6.2. The data points indicated with solid dots were obtained with $T' = 298$ K (25°C) and $T = 303$ K (30°C). The data indicated with circles were obtained in a separate experiment by averaging the MDTCs obtained with various T' and T . The theoretical curve shown is a repetition of that shown in fig. 4.5.

Since many of the factors affecting the value of the MDTC at a given OPD were known only approximately (e.g., total collected power and overall efficiency η_o) only rough agreement between the experimental results and theoretical predictions shown in fig. 6.2 was expected. The most important features are the general shape of the curve and the fact that the MDTC reaches a minimum at an OPD of about 6 cm in agreement with the theory presented in Chapters 3 and 4. The fact that the MDTCs indicated by the circles are somewhat larger than those indicated by solid dots results from the different number of data points taken in each case. In the former case fewer data points were taken at each temperature resulting in greater uncertainty in the output signal levels

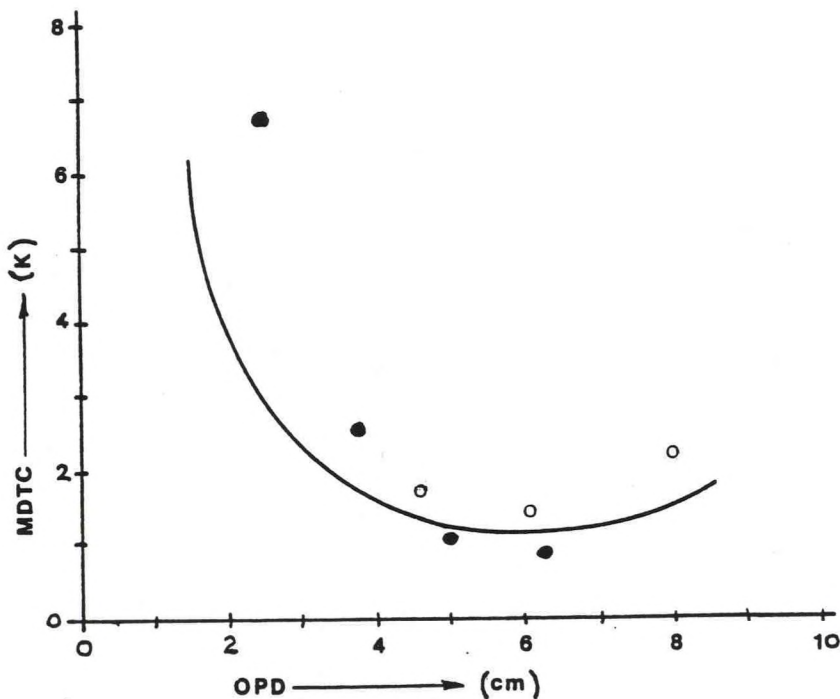


Fig. 6.2 Measured MDTC vs. OPD.

The data indicated with solid dots and circles were obtained in separate experiments as explained in the text. The solid curve indicates the theoretical MDTC as shown previously in fig. 4.5.

causing a greater MDTC. These results clearly indicate that optimum performance of the interferometer is obtained at an optical delay of about 6 cm.

The most important results of this experiment are shown in figs. 6.3, 6.4, and 6.5 where calculated temperatures T_c are graphed versus measured air temperatures for three different optical delays. Ideally, the calculated and measured temperatures should be equal, as indicated by the solid lines. As can be seen from the figures, the actual calculated temperatures generally agree with the measured temperatures to within the indicated experimental uncertainty except at the higher

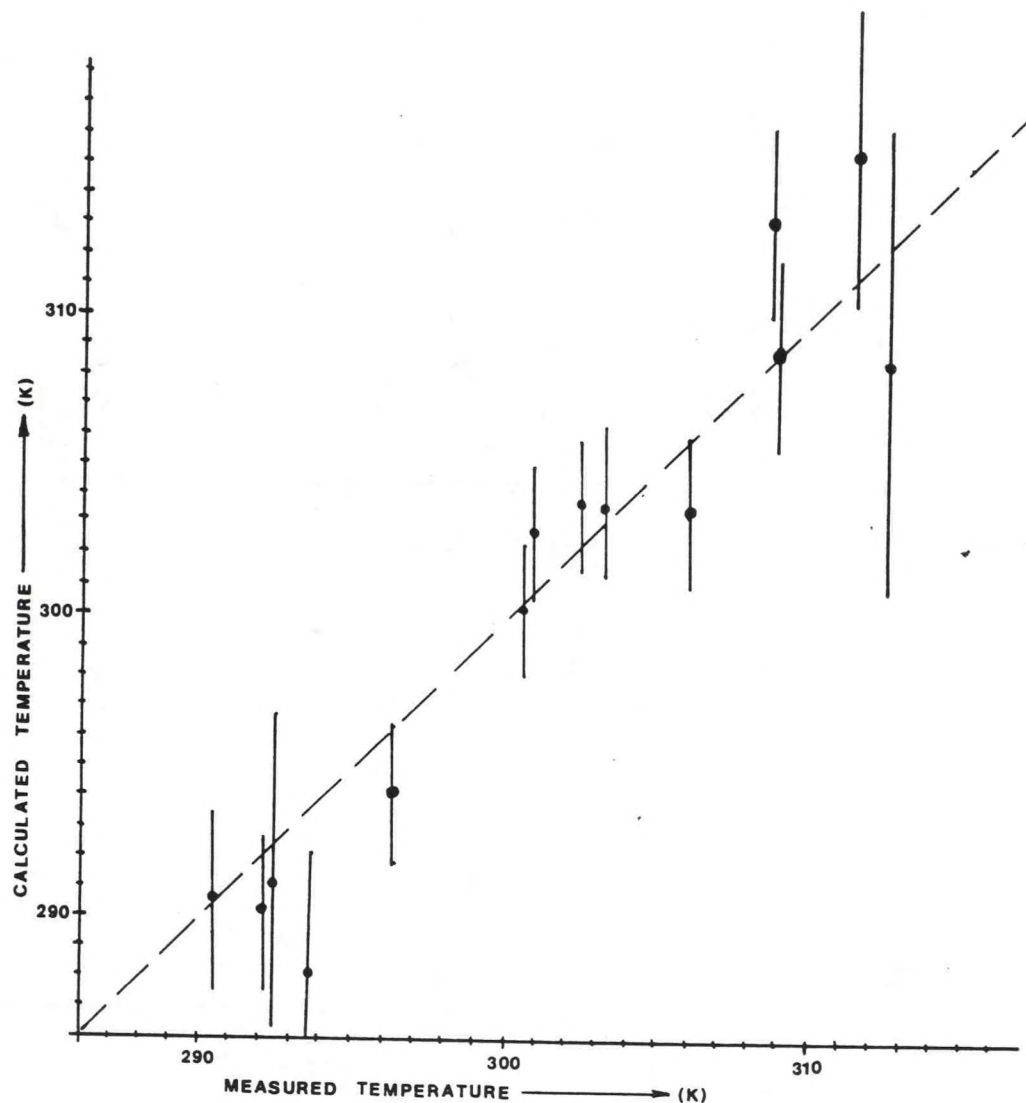


Fig. 6.3 Measured and Calculated Air Temperatures Based on Interferometer Output Signals with an Optical Delay of 4.6 cm.

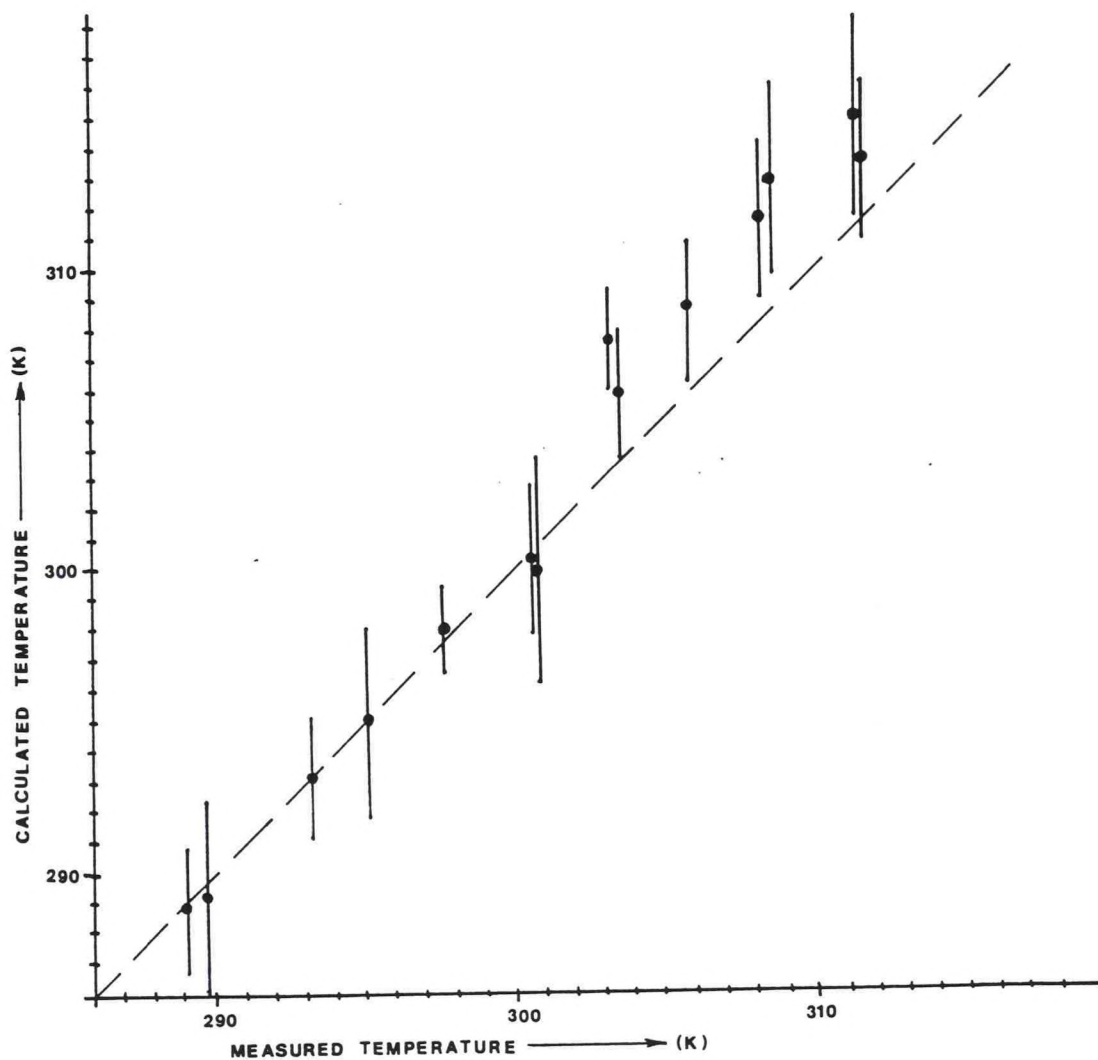


Fig. 6.4 Measured and Calculated Air Temperatures Based on Interferometer Output Signals with an Optical Delay of 6.0 cm.

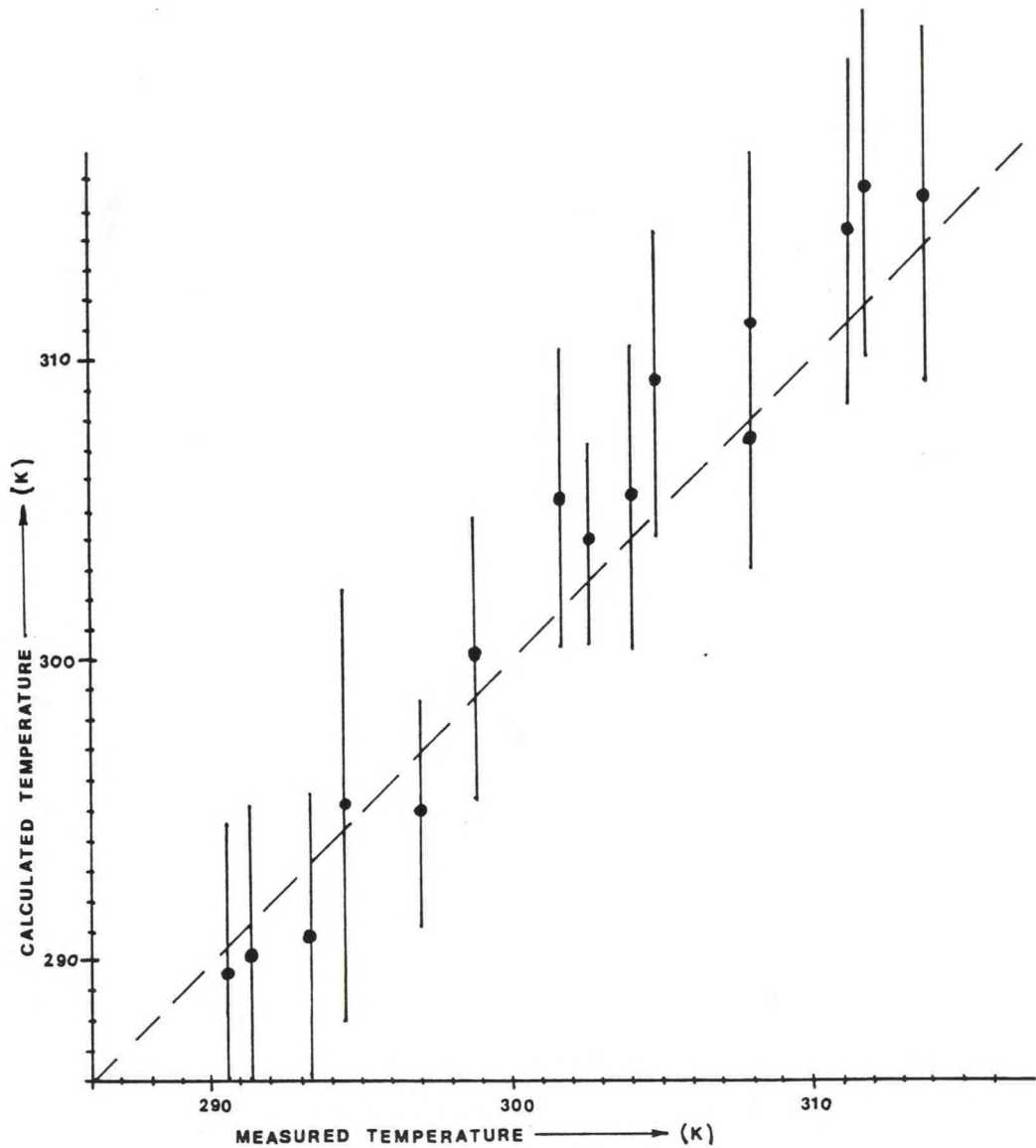


Fig. 6.5 Measured and Calculated Air Temperatures Based on Interferometer Output Signals with an Optical Delay of 8.0 cm.

temperatures. Before pursuing this result further several other features should be noted.

Although the general agreement between the calculated and measured temperatures is apparent in all three graphs, the scatter and uncertainty in the data is obviously least in fig. 6.4 which corresponds to an OPD of 6.05 cm. This result supports the MDTC results previously described. Again, this verifies the existence of an optimum OPD for this measurement at about 6 cm.

An important aspect of this study is the calculation of the Brillouin correction factors, F_c . The necessity of this correction is clearly shown by fig. 6.5 where the calculated temperatures at the upper end of the graph would be about 5 K higher if the correction factor were not applied. Without the correction factor the agreement between the experimental results and the theory would be poor. Therefore, it may be concluded that the data verifies the importance of this correction factor. The Brillouin correction factor becomes less important at smaller OPDs (see fig. 3.6) accounting for a temperature difference of only 2 K at the upper end of the graph of fig. 6.4. Unfortunately, in this case the experimental data does not agree well with the measured temperatures.

Figure 6.4 presents the results obtained at the optimum OPD of about 6 cm. Excellent agreement exists between the measured and calculated air temperatures in the 12 K range from about 290 K to 302 K. In this region the temperature uncertainty is about ± 2 K. However for temperatures above 302 K the calculated temperatures exceed the measured

temperatures by 3 to 5 K, a discrepancy which exceeds the indicated experimental uncertainty. The most likely causes of this discrepancy are: (1) failure of the thermistor sensor to accurately predict the average air temperature within the scattering volume and/or (2) an incorrect Brillouin correction factor.

The unusual feature of the data is sudden transition between good agreement below 302 K and poor agreement above. In regards to this feature it is important to note that the ambient temperature outside the heated gas flow was about 298 K. Above this temperature relatively large heater currents were required, which resulted in greater temperature gradients across the flow and possibly greater turbulence. As noted previously (see Chapter 5) these effects lead to an uncertainty in the thermistor probe calibration which was difficult to estimate. This uncertainty probably accounts for part of the discrepancy seen in fig. 6.4.

Another possibility is uncertainty in the Brillouin correction factor, F_c . A smaller value of F_c than that applied to the data of fig. 6.4 would tend to bring the data points down at the upper end of the graph and raise them slightly at the lower end. However, this would also mean that an even greater correction would occur for the data of fig. 4.6. From this observation it seems unlikely that the Brillouin correction factors are off by much. However, a small adjustment in the correction factors coupled with the uncertainty in the thermistor probe calibration could explain the discrepancy between the experimental results and theory seen in fig. 6.4.

In summary, it seems apparent that the theoretical results obtained generally verify the theoretical predictions regarding the performance of the fixed-delay, frequency shifted Michelson interferometer as a remote air temperature sensor. Specifically, it was found that a minimum MDTC occurred at an optical delay of about 6 cm where an average value of 1.2 K was obtained. Calculated temperatures based on the output signals from the interferometer agreed well with those measured by the thermistor probe in the range 290 K to 302 K. Between 302 K and 314 K the calculated temperatures were somewhat higher than those measured. The discrepancy is probably due to uncertainty in the thermistor probe calibration although incorrect values for the Brillouin correction factors may also contribute. At the optimum OPD of 6 cm the temperature uncertainty due to signal shot noise was about ± 2 K which is not far from the original goal of an uncertainty of ± 1 K. With the exception of signal shot noise, none of the factors contributing to uncertainty in this experiment were fundamental in nature. A more careful design of the interferometer and scattering chamber would have reduced them to a negligible level.

Signal Levels and Averaging Times

It was stated above that temperature measurements with an uncertainty of ± 2 K were achieved with the interferometer operating at an optical delay of 6 cm. In order to put these results into perspective the optical signal power level and averaging times must also be stated. Although the total collected power was never measured it was

estimated to be about 5.7×10^{-10} watts in Chapter 5. The effective averaging times for the data shown in figs. 6.3 through 6.5 may be determined from the averaging time of the electronics and number of data points taken at each temperature. Generally, the procedure followed was to take four or five data points at the calibration temperature both at the beginning and end of the experiment and three data points at all other temperature levels. The averaging time of the electronics was 1.25 seconds. If the time required to acquire the calibration signals is disregarded then the effective averaging time for temperature measurements was about 4 seconds, corresponding to an effective bandwidth of 0.25 Hz.

CHAPTER 7

CONCLUSIONS

In this dissertation it has been shown that a fixed-delay Michelson interferometer provides a simple and efficient means of remotely measuring air temperatures by monitoring the spectral width of Rayleigh-Brillouin scattered light. This device was compared theoretically with a Fabry-Perot interferometer in this application and found to make better use of the available signal in the signal shot noise limited case. The effects of Brillouin scattering on temperature measurements were studied and it was shown that although the shape of the scattered spectrum varies with air pressure, the output of the Michelson interferometer is effectively insensitive to pressure changes on the order of 10 mbar even at pressures near 1 atm. It was also shown that a convenient way of making the interferometer insensitive to small changes in the center frequency of the scattered spectrum was to frequency shift one arm of the interferometer relative to the other and then detect the amplitude of the resulting AC output. To verify the operation of this type of interferometer as a remote sensor of air temperature a frequency shifted, fixed-delay Michelson interferometer and laboratory scattering chamber were built and tested. The experimental results obtained were generally in good agreement with the theory.

In the theoretical developments of Chapter 3 it was shown that the fixed delay Michelson interferometer was superior to the Fabry-Perot

interferometer for measuring air temperature changes. Although this result is not new,⁵ the analysis presented here has the advantage of being intuitively appealing by providing a comparison based on minimum detectable temperature change (MDTC). This figure of merit is readily measurable experimentally and was verified for the case of the frequency shifted, fixed-delay Michelson interferometer. With this instrument the MDTC was found to reach a minimum value when the interferometer was operated at an optical delay of about 6 cm in agreement with the theoretical predictions.

Two of the most significant contributions of this work are the theoretical and experimental results obtained regarding the effect of Brillouin scattering on temperature measurements made with a Michelson interferometer. It was found that a Michelson interferometer operated at the optimum OPD is nearly insensitive to Brillouin pressure induced changes in the scattered spectrum for pressure changes on the order of 10 mbar. This result should lay to rest fears that an accurate knowledge of atmospheric pressure would be necessary in order to determine atmospheric temperature profiles using a fixed-delay Michelson interferometer. However, it is also clear from the experimental results that the Brillouin effects must not be ignored. The Brillouin correction factor calculated theoretically amounted to a correction of 2 K for some measurements. Although some discrepancy exists in the data, it is clear that a correction of at least this magnitude is necessary.

The concept of frequency shifting one arm of the interferometer relative to the other proved to be a simple and effective method of

modulating the output of the interferometer and making it insensitive to small changes in the center frequency of the scattered spectrum. It was found that the rotating waveplate technique used in optical testing⁴¹ was an effective method of producing the required frequency shift although it was also found that slight misalignments and imperfections in the waveplates caused undesirable spurious signals. These problems however are not fundamental in nature and could be eliminated by using high quality zero-order waveplates.

Generally speaking, the frequency shifted, fixed-delay Michelson interferometer used in the experimental investigations reported here worked well and demonstrated a capability of remotely measuring air temperatures in the absence of aerosol scattering. Although difficulties arose from drift in the interferometer alignment, this problem was also not of a fundamental nature and could be easily eliminated in a more careful design. Temperature measurements in the range of 290 K to 302 K were demonstrated with an uncertainty of ± 2 K fulfilling the original goals of the experiment. Since the uncertainty in these measurements depends almost entirely on signal shot noise, it is clear that a more signal efficient interferometer and optical system design could have significantly reduced the measurement uncertainty (the interferometer used in this experiment utilized less than 25% of the available signal). Although temperature measurements in the range of 302 K to 315 K were several degrees higher than predicted, it seems likely that this discrepancy was due mainly to uncertainty in the thermistor probe calibra-

tion caused by turbulence and uneven heating of the air flowed through the scattering volume.

The results obtained from this work suggest several recommendations for future efforts. Since the Brillouin effects are important for precise temperature measurements, an accurate spectral model is needed for Rayleigh-Brillouin scattering in air. To produce such a model, more theoretical and experimental work will both be required. In terms of hardware, a more stable interferometer would be required for routine temperature measurements. A solid interferometer formed by a beamsplitter cube and optically contacted glass spacers for the arms would be one possibility offering simplicity and ruggedness. If the frequency shifting technique is to be used, higher quality, zero-order waveplates should be specified in order to eliminate spurious signals. If the center frequency of the scattered spectrum is invariant then the interferometer could be operated in a stabilized fringe mode locked to a dark fringe as suggested by Schwiesow and Lading⁶ to obtain optimum noise performance.

In conclusion it seems fair to say that the fixed-delay Michelson interferometer provides an efficient tool for remotely measuring air temperatures by the Rayleigh linewidth technique. Temperature measurements with an uncertainty of ± 1 K should be possible with scattered light levels on the order of 10^{-9} watts and averaging times on the order of 5 s or less. Although atmospheric remote temperature sensing poses additional problems, such as the presence of aerosol scattering, this technique should still be applicable with appropriate modifications.

APPENDIX

CALCULATING THE y PARAMETER

The y parameter introduced in Chapter 2 is an important parameter in the calculation of the spectral shape of Rayleigh-Brillouin scattered light. Unfortunately, there is some confusion in the literature concerning the magnitude of this parameter under normal, sea level atmospheric conditions. For example, the value quoted by Fiocco and DeWolf³ for air is a factor of about 2.4 lower than that quoted by Sandoval and Armstrong²⁰ for nitrogen. Although it is true that the exact value of the y parameter depends on the molecular physics of the scattering gas,¹⁵ the discrepancy mentioned above cannot be accounted for.

A survey of the papers in this field reveals that most authors^{18,19,20,48} define y in terms of the shear viscosity of the gas,

$$y = \frac{p}{k \eta [2 k_B T/M]^{1/2}} \quad (A.1)$$

where p is pressure, η is the shear viscosity of the gas, k_B is Boltzman's constant, T is the temperature, M is molecular mass, and k is given by $k = (4\pi/\lambda_o) \sin(\theta/2)$. As in Chapter 2, λ_o is the wavelength of the incident light and θ is the scattering angle. The viscosity depends almost entirely on temperature and may be approximated as follows:²⁵

$$\eta = 14.58 \frac{[T(K)]^{1/2}}{T(K) + 110.4} \quad (A.2)$$

where the units of temperature are Kelvin and the resulting units of η are μ poise. Using the approximation of eqn. A.2 and a value 28.964 for the molecular weight of air,²⁵ equation A.1 may be rewritten to obtain

$$y = 0.2308 \frac{T(K) + 110.4}{[T(K)]^2} \frac{P(atm) \lambda(nm)}{\sin(\theta/2)} \quad (A.3)$$

where the required units are indicated. Equation A.3 has been used throughout this dissertation to calculate values of y where required. Results obtained from this expression also agree with y values quoted by Sandoval and Armstrong²⁰ in their experimental work with nitrogen.

REFERENCES

1. M.T. Decker, E.R. Westwater, and F.O. Guiraud, "Experimental Evaluation of Ground-Based Microwave Radiometric Sensing of Atmospheric Temperature and Water Vapor Profiles," *J. Appl. Meteorology*, 17, 1788 (Dec. 1978).
2. David C. Hogg, "Ground-Based Remote Sensing and Profiling of the Lower Atmosphere Using Radio Wavelengths," *IEEE Trans. on Antennas and Propagation*, AP-28, 281 (March 1980).
3. G. Fiocco and J.B. DeWolf, "Frequency Spectrum of Laser Echoes from Atmospheric Constituents and Determination of the Aerosol Content of Air," *J. Atmos. Sci.*, 25, 488 (May 1968).
4. G. Fiocco, G. Benedetti-Michelangeli, K. Maischberger, and E. Madonna, "Measurement of Temperature and Aerosol to Molecule Ratio in the Troposphere by Optical Radar," *Nature Physical Science*, 229, 78 (Jan. 8, 1971).
5. L. Lading and A. Skov Jensen, "Estimating the Spectral Width of a Narrowband Optical Signal," *Appl. Opt.*, 19, 2750 (Aug. 1980).
6. R.L. Schwiesow and L. Lading, "Temperature Profiling by Rayleigh-Scatter Lidar," *Appl. Opt.*, 20, 1972 (1 June 1981).
7. Albert A. Michelson, "On the Application of Interferometric Methods to Spectroscopic Measurements — I," *Phil. Mag.*, 31, 338 (1891).
8. Albert A. Michelson, "On the Application of Interferometric Methods to Spectroscopic Measurements — II," *Phil. Mag.*, 34, 280 (1892).
9. J. Terrien, "The Visibility of Two Beam Interference, its Measurement and its Spectroscopic Interpretation," *Interferometry*, Symposium No. 11 of the National Physical Laboratory, 1959 (Her Majesty's Stationery Office, London, 1960).
10. Earl J. McCartney, Optics of the Atmosphere, (John Wiley & Sons, New York, 1976).
11. Immanuil L. Fabelinskii, Molecular Scattering of Light, (Plenum Press, New York, 1968).
12. H.F.P. Knaap and P. Lallemand, "Light Scattering by Gases," in Annual Review of Physical Chemistry, H. Eyring, ed. (Annual Reviews, Inc., Palo Alto, 1975).

13. Andrew T. Young, "Rayleigh Scattering," *Appl. Opt.*, 20, 533 (15 Feb. 1981).
14. S.M. Rytov, "Correlation Theory for Rayleigh Scattering of Light I," *Soviet Physics JETP*, 6(33), 401 (Feb. 1958).
S.M. Rytov, "Correlation Theory for Rayleigh Scattering of Light II," *Soviet Physics JETP*, 6(33), 513 (March 1958).
S.M. Rytov, "Correlation Theory of Thermal Fluctuations in an Isotropic Medium," *Soviet Physics JETP*, 6, 130 (Jan. 1958).
15. Sidney Yip, "Rayleigh Scattering in Dilute Gases," *J. Acoustical Soc. Amer.*, 49, 941 (1971).
16. Rudolf Pendorf, "Tables of Refractive Index of Standard Air and the Rayleigh Scattering Coefficient for the Spectral Region between 0.2 and 20.0 μm and their Application to Atmospheric Optics," *J. Opt. Soc. Amer.*, 47, 176 (Feb. 1957).
17. R.L. Rowell, G.M. Aval, and J.J. Barrett, "Rayleigh-Raman Depolarization of Laser Light Scattered by Gases," *J. Chem. Phys.*, 54, 1960 (1 March 1971).
18. G. Tenti, C.D. Boley, and Rashmi C. Desai, "On the Kinetic Model Description of Rayleigh-Brillouin Scattering from Molecular Gases," *Can. J. Phys.*, 52, 285 (15 Feb. 1974).
19. Q.H. Lao, P.E. Schoen, and B. Chu, "Rayleigh-Brillouin Scattering of Gases with Internal Relaxation," *J. Chem. Phys.*, 64, 3547 (1 May 1976).
20. R.P. Sandoval and R.L. Armstrong, "Rayleigh-Brillouin Spectra in Molecular Nitrogen," *Phys. Rev. A*, 13, 752 (Feb. 1976).
21. Sidney Yip and Mark Nelkin, "Application of a Kinetic Model to Time-Dependent Density Correlations in Fluids," *Phys. Rev.*, 135, A1241 (31 Aug. 1964).
22. C.F. Campden, Jr., ed., Handbook of Geophysics, (MacMillan Co., New York, 1961).
23. S.T. Shipley, J.H. Joseph, J.T. Trauger, T.J. Guetter, E.W. Eloranta, J.E. Lawler, W.J. Wiscombe, A.T. Odell, F.L. Roesler, and J.A. Weinman, "The Evaluation of a Shuttle Borne Lidar Experiment to Measure the Global Distribution of Aerosols and Their Effect on the Atmospheric Heat Budget," Final Report on NASA Grant NSG 1057, April 1975 (University of Wisconsin).

24. Glauco Benedetti-Michelangeli and Georgio Fiocco, "Active and Passive Optical Doppler Techniques for the Determination of Atmospheric Temperature, 2: A Highly Coherent Laser Radar," in Structure and Dynamics of the Upper Atmosphere, F. Verniani, ed. (Elsevier Scientific Publishing Co., Amsterdam, 1974).
25. Maurice Dubin, Norman Sissenwine, and Harry Wexler, cochairmen, U.S. Standard Atmosphere, 1962, (U.S. Government Printing Office, Washington, D.C., 1962).
26. R.G. Strauch, V.E. Derr, and R.E. Cupp, "Atmospheric Temperature Measurement Using Raman Backscatter," Appl. Opt., 10, 2665 (Dec. 1971).
27. S. Bhagavantam, Scattering of Light and the Raman Effect, (Chemical Publishing Co., Brooklyn, N.Y., 1942).
28. Ariel Cohen, John A. Cooney, and Kenneth N. Geller, "Atmospheric Temperature Profiles from Lidar Measurements of Rotational Raman and Elastic Scatter," Appl. Opt., 15, 2896 (Nov. 1976).
29. C.M. Penney, R.L. St. Peters, and M. Lapp, "Absolute Rotational Raman Cross Sections for N₂, O₂, and CO₂," J. Opt. Soc. Amer., 64, 712 (May 1974).
30. Ralph R. Rudder and David R. Bach, "Rayleigh Scattering of Ruby-Laser Light by Neutral Gases," J. Opt. Soc. Amer., 59, 1260 (Sept. 1968).
31. John Chamberlain, The Principles of Interferometric Spectroscopy, (John Wiley & Sons, New York, 1979).
32. Robert John Bell, Introductory Fourier Transform Spectroscopy, (Academic Press, New York, 1972).
33. Max Born and Emil Wolf, Principles of Optics, Fifth Edition, (Pergamon Press, New York, 1975).
34. Daniel Malacara, ed., Optical Shop Testing, (John Wiley & Sons, New York, 1978).
35. Philip R. Bevington, Data Reduction and Error Analysis for the Physical Sciences, (McGraw-Hill, New York, 1969).
36. J. Chamberlain, "Phase Modulation in Far Infrared (Submillimetre-Wave) Interferometers. I — Mathematical Formulation," Infrared Physics, 11, 25 (1971).

37. C.F. Bahrer, V.J. Fowler, and L.R. Bloom, "Single Sideband Suppressed-Carrier Modulation of Coherent Light Beams," Proc. IRE, 50, 1827 (Aug. 1962).
38. C.F. Bahrer, D. Baird, and E.M. Conwell, "Optical Frequency Shifting by Electro-Optic Effect," Appl. Phys. Lett., 1, 46 (1 Oct. 1962).
39. V.J. Fowler, C.F. Bahrer, L.R. Bloom, D. Baird, and E.M. Conwell, "Theory and Applications of Single-Sideband Suppressed-Carrier Optical Modulation," Chapter 9 in Optical Processing of Information, D. Pollack, C. Koester, and J.T. Tippett, eds., (Spartan Books, Baltimore, 1963).
40. Robert Crane, "Interference Phase Measurement," Appl. Opt., 8, 538 (March 1969).
41. Gary E. Sommagren, "Up/Down Frequency Shifter for Optical Heterodyne Interferometry," J. Opt. Soc. Amer., 65, 960 (Aug. 1975).
42. R.N. Shagam and J.C. Wyant, "Optical Frequency Shifter for Heterodyne Interferometers Using Multiple Rotating Polarization Retarders," 17, 3034 (1 Oct. 1978).
43. R. Clark Jones, "A New Calculus for the Treatment of Optical Systems," J. Opt. Soc. Amer., 31, 488 (July 1941).
44. Maurice Francon and S. Mallick, Polarization Interferometers, (Wiley Interscience, New York, 1971).
45. "Noise Performance of Vector Sum Lock-in Amplifiers," Technical Bulletin IPB-0121, (Ithaco, Inc., Ithaca, N.Y., 1978).
46. John Strong, Concepts of Classical Optics, (W.H. Freeman and Co., San Francisco, 1958).
47. John P. Rahn, "How to Extinguish a Light Beam Without Scatter," Appl. Opt., 17, 2475 (15 Aug. 1978).
48. Akira Sugawara and Sidney Yip, "Kinetic Model Analysis of Light Scattering by Molecular Gases," Phys. of Fluids, 10, 1911 (Sept. 1967).